UNIVERSITY OF CALIFORNIA,
IRVINE

Thermodynamic Considerations for Achieving Selective and Reversible CO_2 to HCO_2^- Electrocatalysis

DISSERTATION

submitted in partial satisfaction of the requirements
for the degree of

DOCTOR OF PHILOSOPHY

in Chemistry

by

Drew Whittier Cunningham

Dissertation Committee:
Associate Professor Jenny Y. Yang, Chair
Distinguished Professor A. S. Borovik
Distinguished Professor William J. Evans

2020

DEDICATION

To my high school chemistry teacher,

Pete “Mr. L” Lewandowski.

Without your guidance, passion for chemistry, and willingness to push me

I question if any of this would have been possible.

TABLE OF CONTENTS

LIST OF FIGURES

LIST OF TABLES

LIST OF SCHEMES

ACKNOWLEDGMENTS

To my PI, Jenny Yang: You helped me out at a particularly difficult time in my life and I can never thank you enough for giving me that chance. You have taught me a tremendous amount and I will carry that with me for the rest of my career. We are incredibly lucky to have you as a leader and mentor.

To my parents: What a journey it has been. Your endless support and willingness to put up with me have allowed me to be where I am today. Thank you for everything.

VITA

Drew W. Cunningham

Education

Ph.D. Chemistry	University of California, Irvine	Expected March 2020
B.S. Chemistry	University of Wisconsin, Stevens Point	2014

Research Experience

Visiting Researcher, DOE SCGSR, Pacific Northwest National Laboratory Winter 2019
Advisor: Drs. Aaron Appel and John Linehan

- Investigated water-soluble, homogeneous catalysts for aqueous CO_2 hydrogenation utilizing high-pressure NMR spectroscopy

Ph.D. Candidate, University of California, Irvine 2016 – 2020
Advisor: Prof. Jenny Y. Yang

- Synthesized and characterized molecular catalysts for the reduction of CO_2
- Performed mechanistic studies utilizing NMR spectroscopy and electrochemical techniques
- Utilized thermodynamic principles for the rational design of CO_2-reduction electrocatalysts

Ph.D. Student, University of California, Irvine 2014 – 2016
Advisor: Prof. Suzanne A. Blum

- Utilized single-molecule fluorescence microscopy for studying the kinetics of organometallic reactions
- Synthesized and characterized organic substrates for method development
- Investigated the kinetics of organometallic catalysts using NMR spectroscopy for method optimizations

Undergraduate Researcher, University of Wisconsin, Stevens Point 2011 – 2014
Advisor: Prof. Jason S. D'Acchioli

- Synthesized and characterized organometallic compounds for applications to the water-gas shift reaction
- Performed DFT calculations to provide insight into the electronic structure of transition metal complexes

Publications

1. Cunningham, D. W.; Yang, J.Y. Investigating the Kinetics for the Electrocatalytic Reduction of CO_2 to HCO_2^- by a Homogeneous Platinum Hydride. *Manuscript in preparation for submissions to Inorganic Chemistry*.
2. Cunningham, D. W.; Yang, J. Y. Selective Electrocatalytic Reduction of CO_2 to HCO_2^-. *Trends in Chemistry*. Invited Perspective; Submitted February 20, 2020.

3. Cunningham, D. W.; Barlow, J. M.; Velasquez, R. S.; Yang, J. Y. Reversible and Selective CO_2 to HCO_2^- Electrocatalysis near the Thermodynamic Potential. *Angew. Chem. Int. Ed.* Published online December 17, 2019. DOI: 10.1002/anie.201913198.
    - Highlighted as a Very Important Paper (VIP).
4. Thammavongsy, Z.; Cunningham, D. W.; Sutthirat, N.; Eisenhart, R. J.; Ziller, J. W.; Yang, J. Y. Adaptable ligand donor strength: Tracking Transannular Bond Interactions in *tris*(2-pyridylmethyl)-azaphosphatrane (TPAP). *Dalton Trans.* **2018**, *47*, 14101–14110.
5. Feng, C.; Cunningham, D. W.; Easter, Q. T.; Blum, S. A. Role of LiCl in Generating Soluble Organozinc Reagents. *J. Am. Chem. Soc.* **2016**, *138*, 11156–11159.
    - Highlighted in *Org. Process. Res. Dev.* **2016**, *20*, 1961.
6. Webster, A. J.; Mueller, C. M.; Foegen, N. P.; Sit, P. H. L.; Speetzen, E. D.; Cunningham, D. W.; D'Acchioli, J. S. Oxidation states "naturally": A Natural Bond Orbital method for determining transition metal oxidation states. *Polyhedron* **2016**, *114*, 128–132.

Presentations

1. Cunningham, D. W.; Ceballos, B. M.; Yang, J. Y. Selective Electrocatalytic Reduction of H^+ or CO_2. American Chemical Society National Meeting, San Diego, CA, 2019.
2. Cunningham, D. W.; Yang, J. Y. Reversible CO_2/formate Interconversion by a Homogeneous Platinum Electrocatalyst. American Chemical Society National Meeting, San Diego, CA, 2019.
3. Cunningham, D. W.; Yang, J. Y. Selective Reduction of CO_2: A Rational Thermodynamic Approach to Disfavor Proton Reduction Pathways. American Chemical Society National Meeting, New Orleans, LA, 2018.
4. Cunningham, D. W.; Ceballos, B. M.; Yang, J. Y. Tailoring Hydrogen Evolution Reaction Catalysts for Operation at Specific pH Values. Southern California Bioinorganic Meeting, Irvine, CA, 2017.
5. Cunningham, D. W.; Blum, S. A. The Influence of LiCl on the Formation of Organozinc Compounds. Organic Chemistry Graduate Student Symposium, Irvine, CA, 2015.
6. Cunningham, D. W.; Zach, M. T. Characterization of Atmospheric Particulate Matter by Scanning Electron Microscopy/Energy Dispersive X-ray Spectrometry. Chemistry Undergraduate Senior Independent Research Symposium, Stevens Point, WI, 2014.
7. Cunningham, D. W.; D'Acchioli, J. S. Water-Gas Shift Catalysts: A New Use For Classic Compounds. Undergraduate Research Symposium, Stevens Point, WI, 2013.
8. Cunningham, D. W.; D'Acchioli, J. S. A 'Novel' Molybdenum Complex: Possible Photovoltaic Material. Undergraduate Research Symposium, Stevens Point, WI, 2013.

Awards

DOE Office of Science Graduate Student Research (SCGSR) Fellowship	2019
NSF Research Traineeship (NRT) Award	2017
ACS Undergraduate Award in Inorganic Chemistry	2013
Trytten Sophomore Chemistry Award	2012
Trytten Freshman Chemistry Award	2011

Professional Affiliations

UWSP American Chemical Society Student Chapter Vice President	2012 – 2013
American Chemical Society Member	2011 – Present
UWSP American Chemical Society Student Chapter Member	2010 – 2014

ABSTRACT OF THE DISSERTATION

Thermodynamic Considerations for Achieving Selective and Reversible CO_2 to HCO_2^- Electrocatalysis

By

Drew Whittier Cunningham

Doctor of Philosophy in Chemistry

University of California, Irvine, 2020

Professor Jenny Y. Yang, Chair

Reversible catalysis is a hallmark of energy-efficient chemical transformations, but can only be achieved if the changes in free energy of intermediate steps are minimized and the catalytic cycle is devoid of high transition-state barriers. In Chapter 1, using these criteria, we demonstrate reversible CO_2 to HCO_2^- conversion catalyzed by $[HPt(depe)_2]^+$ (where depe=1,2-*bis*(diethylphosphino) ethane). Direct measurement of the free energies associated with each catalytic step correctly predicts a slight bias towards CO_2 reduction. We demonstrate how the experimentally measured free energy of each step directly contributes to the <50 mV overpotential. We also find that for CO_2 reduction, H_2 evolution is negligible and the Faradaic efficiency for HCO_2^- production is nearly quantitative. A free-energy analysis reveals H_2 evolution is endergonic, providing a thermodynamic basis for highly selective CO_2 reduction.

In Chapter 2, the kinetics of each step of the catalytic cycle for CO_2 reduction is assessed as a means to elucidate the nature of the sluggish catalytic rate. By measuring the rates of electron transfer, protonation, and CO_2 insertion, it was shown that the catalytic rate is limited by CO_2 insertion into $[HPt(depe)_2]^+$.

Chapter 3 diverges from the common themes discussed in this dissertation and describes the role of lithium chloride for enabling the insertion of metallic zinc into organic halides. The sensitivity provided by fluorescence microscopy enabled the observation of surface intermediates in the synthesis of soluble organozinc reagents by direct insertion of commercial zinc powder into alkyl iodides. Five hypotheses were examined for the mechanistic role of lithium chloride in enabling this direct insertion. The data are consistent with lithium chloride solubilizing organozinc reagents from the surface of the zinc after oxidative addition.

INTRODUCTION

The concentration of atmospheric CO_2 has increased to over 400 ppm from ca. 280 ppm at the beginning of the Industrial Revolution.[1] In order to supplement our current energy demands and to address environmental concerns, there is a need to develop carbon-neutral energy production schemes.[2-3] One way this can be achieved is by taking inspiration from nature: in photosynthesis, solar-converted energy is stored in chemical bonds. A schematic diagram for an artificial photosynthetic cell can be seen in Scheme 0.1. In this highly schematic representation, an oxidation catalyst, "O" in Scheme 0.1, oxidizes water to make oxygen, protons, and electrons, with concomitant migration of protons and electrons to the reduction side of the cell, or fuel-forming step, where a reduction catalyst, "R" in Scheme 0.1, then reduces CO_2 to yield more energy-dense products (e.g. sugars, CH_4, CH_3OH, and HCO_2^-) that are stored for later use. Development of an artificial photosynthetic process requires selective and efficient electrocatalysts for the reduction of substrates in the fuel-forming step (dotted rectangle in Scheme 0.1).

Scheme 0.1. Schematic Diagram for an Artificial Photosynthetic Cell[a]

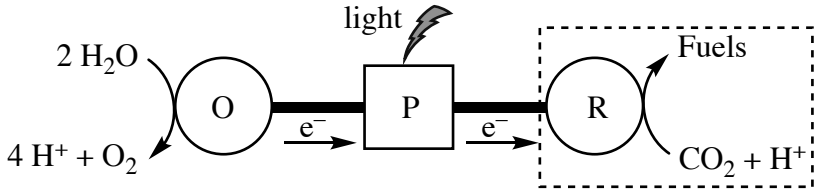

[a] "O," "P," and "R" represent oxidation, photosensitizer, and reduction catalysts, respectively.

In nature, photosynthetic pathways have been optimized over the course of billions of years to allow for efficient processes. Protons and electrons produced from the oxidation of water are stored as hydride equivalents by reduction of $NADP^+$ to NADPH;[4] there over 400 enzymatic reduction or oxidations reactions that involve the net transfer of a hydride to $NADP^+$.[5]

Although intimate mechanistic details for the fuel-forming steps in many biological systems are often not well understood, several enzymatic processes have been proposed to go through a transition-metal hydride intermediate: a Fe–H–Ni in [NiFe]-hydrogenase,[6] dehydrogenase, and a Fe–H–Fe in the [FeMo]-cofactor of nitrogenase.[7-8] Transition-metal hydrides are ubiquitous intermediates for energy-conversion schemes in biological systems.[9] In addition to their biological significance, metal hydrides have widespread uses in relevant catalytic processes such processes such as alkene[10-11] and carbonyl[12-14] hydrogenation, olefin isomerization,[15-16] and C–H bond activation.[17-19]

Due to the widespread use of metal hydrides throughout the mid to late 19th century, fundamentally understanding the nature of the M–H bond was of significant interest. In the 1980s, pioneering work by Norton[20-23] and others[24] systematically quantified the thermochemistry associated with the M–H bond, specifically the homolytic bond dissociation free energy (BDFE, eq 0.1) and the acidity (pK_a, eq 0.2). Early work describing the reactivity of metal hydrides and their relative hydride donor strength, or hydricity, focused on kinetic hydricity.[25-27] However, measuring the kinetics of hydride transfer had its limitations. Notably, the rate of the hydride transfer reaction is strongly influenced by the details of the mechanistic steps; for example, a hydride donor that undergoes a concerted reaction mechanism may react slower than a hydride donor undergoing a radical mechanism despite having comparable absolute hydricities.[27] In addition, the rate of the reaction is strongly influenced by the identity of the hydride acceptor.[26]

$$\text{M–H} \rightleftharpoons \text{M}\cdot + \text{H}\cdot \qquad (0.1)$$

$$\text{M–H} \rightleftharpoons \ddot{\text{M}}^{-} + \text{H}^{+} \qquad (0.2)$$

$$\text{M–H} \rightleftharpoons \text{M}^{+} + \ddot{\text{H}}^{-} \qquad (0.3)$$

In order to circumvent these limitations, DuBois and colleagues provided experimentally determined thermodynamic values for the heterolytic cleavage of M–H to donate a hydride moiety, called hydricity or ΔG^{o}_{H-} (eq 0.3).[28-30] Hydricity describes the magnitude of the energy required for M–H bond cleavage and is endergonic, thus a lower value for ΔG^{o}_{H-} corresponds to a stronger hydride-donating ability. As a thermodynamic property, hydricity is a state function and is independent of the path, thus the identity of the hydride acceptor does not influence the hydricity. Hydricity defines the free energy for hydride transfer reactions and a fundamental understanding of the factors that influence the hydricity of a metal hydride would prove to be indispensable for developing catalysts for these transformations.

Prior to DuBois establishing a hydricity scale in the early 2000s, the reactivity of metal hydrides with small molecules, such as CO_2, was largely undeveloped. Darensbourg noted in a 1981 article, on the topic of metal hydrides and CO_2 reactivity, "such a deficiency in chemical knowledge is particularly surprising in view of the abundance of work directed toward an understanding of the water-gas shift reaction."[31] More recently, thermodynamic hydricity has aided in the design of efficient catalysts that proceed through metal hydride intermediates and have demonstrated potential significance for energy-conversion schemes.

The hydricity of HCO_2^- has been experimentally determined to be 44 kcal/mol; thus if a metal hydride is to reduce CO_2 it must have a hydricity ≤44 kcal/mol.[32] Currently there are nearly 100 different compounds that have reported values for ΔG^{o}_{H-} in acetonitrile,. The trends that exist in this data set guides tuning hydricity values for investigation metal hydrides capable of CO_2 reduction to HCO_2^-. The electrocatalytic reduction of CO_2 to HCO_2^- (eq 0.4) is of particular interest for several reasons: 1) HCO_2^- is the most rudimentary reduction product of CO_2 involving protons, being that it results from the net transfer of one hydride unit, 2) as the

simplest reduction product, it is often an intermediate for further reductions to other small molecules of interest (e.g. H_2CO, CH_3OH, and CH_4),[33-36] and 3) the microscopic reverse reaction (HCO_2^- oxidation) is important for energy utilization in fuel cell applications.[37-38] For these reasons, HCO_2^- is chosen as a model to study the fundamental thermochemistry of hydride-transfer reactions.

$$CO_2 + H^+ + 2e^- \rightleftharpoons HCO_2^- \qquad (0.4)$$

Using hydricity as a guide, Linehan and Appel were able to develop a cobalt hydride catalyst, [HCo(dmpe)$_2$] (where dmpe = 1,2-*bis*(dimethylphosphinoethane)), that hydrogenates CO_2 to HCO_2^- under ambient conditions (1 atm CO_2/H_2 and 25 ºC; eq 0.5):[39-41]

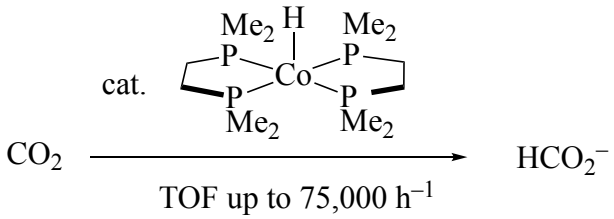

(0.5)

To date, this is the fastest catalyst for the conversion of CO_2 to HCO_2^- with turnover frequencies (TOFs) reaching up to 75,000 h^{-1}. The authors attribute this catalyst to be so active because it was judiciously chosen such that oxidative-addition of H_2 would be exergonic (which is often the rate-determining step in hydrogenation catalysts), leaving CO_2 insertion to be rate limiting which provides for a –8 kcal/mol driving force for this step.[42] Without having a prior, thermodynamic basis for the free energy of each step (i.e. H_2 addition and hydride transfer), discovery of this catalyst would have been limited to "chemical intuition" or brute-force "guess and check" methods for catalyst development.

Although CO_2 reduction to HCO_2^- has recently made promising advances, most of the research efforts have been focused on developing *hydrogenation* catalysts and more important to solar energy conversion schemes are *electrocatalysts*, which have undergone little development.

One notable difference between the two methods, is that in electrocatalysis an acid is needed to protonate a reduced metal species in order to generate M–H, while in hydrogenation catalysis a hydride is delivered to the reduced metal species by the net hydride transfer from H_2 and a base (Scheme 0.2).

Scheme 0.2. Comparison of M–H Generation for Electrocatalytic and Hydrogenation Catalysis

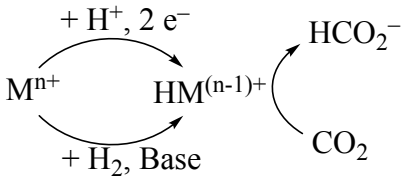

The challenge in electrocatalytic CO_2 reduction is that, in addition to the various carbon-based products that can be formed, protonation of the metal hydride intermediate from protons in solution to form H_2 poses difficulties in obtaining a single product. Due to these challenges, there are currently less than six examples of electrocatalysts that selectively reduce CO_2 to HCO_2^- with Faradaic efficiencies >90%.[43-48]

Unproductive protonation of M–H to form H_2 has recently been addressed within the Yang lab.[49] Ceballos and Yang have developed a first-principles method for systematically determining the conditions such that the hydrogen-evolution reaction (HER) is endergonic and thus will not be thermodynamically favorable. The free energy for protonation of M–H by an acid, or HA, to generate H_2 (eq 0.9 in Table 0.1) can be calculated by utilizing a thermochemical scheme seen in Table 0.1. This is calculated from the hydricity of M–H (eq 0.6), the free energy pertaining to the activity of HA (eq 0.7), and the heterolysis of H_2, a solvent-dependent experimentally determined constant (eq 0.8). The summation of eqs 0.6–0.8 results in the free energy for HER and by setting this sum to be >0, the minimum pK_a of HA can be calculated

such that HER is endergonic. With this "recipe," they were able to rationally choose a catalyst and acid that lead to high-selectivity for the reduction of CO_2 to HCO_2^-.

Table 0.1. Free-Energy Values for Calculating the pK_a Required for Unfavorable HER.

Reaction	ΔG^o (kcal/mol)	eq
$MH \rightleftharpoons M^+ + H^-$	44	0.6
$HA \rightleftharpoons H^+ + A^-$	1.364•pK_a	0.7
$H^+ + H^- \rightleftharpoons H_2$	–76.0[a]	0.8
$MH + HA \rightleftharpoons M^+ + A^- + H_2$	ΔG^o_{HER}	0.9

[a]From ref. [32]

With a method established that aids in selective CO_2 reduction to HCO_2^- and with over 100 values for ΔG^o_{H-} reported in the literature for metal hydrides in acetonitrile, the next logical step was to design a reversible electrocatalyst capable of reversibly interconverting CO_2 and HCO_2^-. Reversible catalysis will be discussed in more depth in Chapter 1 Introduction, but is introduced here. In order to be reversible, the net free energy for every elementary step must not deviate significantly from the thermodynamic potential for the process. If a step does deviates more than a few kcal/mol from the thermodynamic potential, then high or low energy intermediates are formed that create low energy syncs of high energy barriers and do not allow for traversing the reaction coordinate diagram back and forth.

Thesis Overview

This dissertation describes the advancement for the thermodynamic requirements for achieving selective and reversible CO_2 to HCO_2^- electrocatalysis. To this end, fundamental thermochemical principles were experimentally reproduced and quantified by considering the free energy of *every* step in the series of reactions pertaining to CO_2 reduction to HCO_2^-. Several of the consequences are discussed that result from these rigid, thermochemical implementations,

including what is required for efficient catalysis and how they influence rational catalyst design. Methods to minimize the overpotential associated with an electrocatalyst are discussed. In addition to a thermochemical analysis, the kinetics of electrochemical CO_2 reduction was studied as a means to accelerate the CO_2 insertion step into M–H. These studies highlight the importance of considering the thermodynamics associated with every step, while also considering the importance of kinetic limitations for achieving fast catalysis. It is anticipated that this thermochemical insight is generally applicable to achieving selective and reversible M–H reactivity with substrates other than CO_2.

References

1. NOAA Mauna Loa Carbon Dioxide Emssions; https://www.esrl.noaa.gov/gmd/ccgg/trends/weekly.html.

2. Lewis, N. S.; Nocera, D. G. *Proc. Natl. Acad. Sci.* **2006**, *103*, 15729-15735.

3. Lewis, N. S. *Science* **2007**, *315*, 798-801.

4. Archipowa, N.; Kutta, R. J.; Heyes, D. J.; Scrutton, N. S. *Angew. Chem. Int. Ed.* **2018**, *57*, 2682-2686.

5. Gębicki, J.; Marcinek, A.; Zielonka, J. *Acc. Chem. Res.* **2004**, *37*, 379-386.

6. Barton, B. E.; Rauchfuss, T. B. *J. Am. Chem. Soc.* **2010**, *132*, 14877-14885.

7. Khadka, N.; Milton, R. D.; Shaw, S.; Lukoyanov, D.; Dean, D. R.; Minteer, S. D.; Raugei, S.; Hoffman, B. M.; Seefeldt, L. C. *J. Am. Chem. Soc.* **2017**, *139*, 13518-13524.

8. Lukoyanov, D. A.; Khadka, N.; Yang, Z.-Y.; Dean, D. R.; Seefeldt, L. C.; Hoffman, B. M. *Inorg. Chem.* **2018**, *57*, 6847-6852.

9. Appel, A. M.; Bercaw, J. E.; Bocarsly, A. B.; Dobbek, H.; DuBois, D. L.; Dupuis, M.; Ferry, J. G.; Fujita, E.; Hille, R.; Kenis, P. J. A.; Kerfeld, C. A.; Morris, R. H.; Peden, C. H. F.; Portis, A. R.; Ragsdale, S. W.; Rauchfuss, T. B.; Reek, J. N. H.; Seefeldt, L. C.; Thauer, R. K.; Waldrop, G. L. *Chem. Rev.* **2013**, *113*, 6621-6658.

10. Young, J. F.; Osborn, J. A.; Jardine, F. H.; Wilkinson, G. *Chem. Commun.* **1965**, *7*, 131-132.

11. Crabtree, R. *Acc. Chem. Res.* **1979**, *12*, 331-337.

12. Ohkuma, T.; Ooka, H.; Yamakawa, M.; Ikariya, T.; Noyori, R. *J. Org. Chem.* **1996**, *61*, 4872-4873.

13. Pàmies, O.; Bäckvall, J.-E. *Chem. Rev.* **2003**, *103*, 3247-3262.

14. Shvo, Y.; Goldberg, I.; Czerkie, D.; Reshef, D.; Stein, Z. *Organometallics* **1997**, *16*, 133-138.

15. Hart, D. W.; Schwartz, J. *J. Am. Chem. Soc.* **1974**, *96*, 8115-8116.

16. Cramer, R.; Lindsey, R. V. *J. Am. Chem. Soc.* **1966**, *88*, 3534-3544.

17. Chatt, J.; Davidson, J. M. *J. Chem. Soc.* **1965**, 843-855.

18. Wax, M. J.; Stryker, J. M.; Buchanan, J. M.; Kovac, C. A.; Bergman, R. G. *J. Am. Chem. Soc.* **1984**, *106*, 1121-1122.

19. Crabtree, R. H. *J. Chem. Soc., Dalton Trans.* **2001**, 2437-2450.

20. Edidin, R. T.; Sullivan, J. M.; Norton, J. R. *J. Am. Chem. Soc.* **1987**, *109*, 3945-3953.

21. Jordan, R. F.; Norton, J. R. *J. Am. Chem. Soc.* **1982**, *104*, 1255-1263.

22. Kristjansdottir, S. S.; Moody, A. E.; Weberg, R. T.; Norton, J. R. *Organometallics* **1988**, *7*, 1983-1987.

23. Moore, E. J.; Sullivan, J. M.; Norton, J. R. *J. Am. Chem. Soc.* **1986**, *108*, 2257-2263.

24. Tilset, M.; Parker, V. D. *J. Am. Chem. Soc.* **1989**, *111*, 6711-6717.

25. Labinger, J. A.; Komadina, K. H. *J. Organomet. Chem.* **1978**, *155*, C25-C28.

26. Kao, S. C.; Spillett, C. T.; Ash, C.; Lusk, R.; Park, Y. K.; Darensbourg, M. Y. *Organometallics* **1985**, *4*, 83-91.

27. Cheng, T.-Y.; Brunschwig, B. S.; Bullock, R. M. *J. Am. Chem. Soc.* **1998**, *120*, 13121-13137.

28. Berning, D. E.; Noll, B. C.; DuBois, D. L. *J. Am. Chem. Soc.* **1999**, *121*, 11432-11447.

29. Curtis, C. J.; Miedaner, A.; Ellis, W. W.; DuBois, D. L. *J. Am. Chem. Soc.* **2002**, *124*, 1918-1925.

30. Ciancanelli, R.; Noll, B. C.; DuBois, D. L.; DuBois, M. R. *J. Am. Chem. Soc.* **2002**, *124*, 2984-2992.

31. Darensbourg, D. J.; Rokicki, A.; Darensbourg, M. Y. *J. Am. Chem. Soc.* **1981**, *103*, 3223-3224.

32. Wiedner, E. S.; Chambers, M. B.; Pitman, C. L.; Bullock, R. M.; Miller, A. J. M.; Appel, A. M. *Chem. Rev.* **2016**, *116*, 8655-8692.

33. Yan, X.; Ge, H.; Yang, X. *Inorg. Chem.* **2019**, *58*, 5494-5502.

34. Kar, S.; Sen, R.; Kothandaraman, J.; Goeppert, A.; Chowdhury, R.; Munoz, S. B.; Haiges, R.; Prakash, G. K. S. *J. Am. Chem. Soc.* **2019**, *141*, 3160-3170.

35. Wesselbaum, S.; vom Stein, T.; Klankermayer, J.; Leitner, W. *Angew. Chem. Int. Ed.* **2012**, *51*, 7499-7502.

36. Huff, C. A.; Sanford, M. S. *J. Am. Chem. Soc.* **2011**, *133*, 18122-18125.

37. An, L.; Chen, R. *J. Power Sources* **2016**, *320*, 127-139.

38. Vo, T.; Purohit, K.; Nguyen, C.; Biggs, B.; Mayoral, S.; Haan, J. L. *ChemSusChem* **2015**, *8*, 3853-3858.

39. Jeletic, M. S.; Mock, M. T.; Appel, A. M.; Linehan, J. C. *J. Am. Chem. Soc.* **2013**, *135*, 11533-11536.

40. Jeletic, M. S.; Helm, M. L.; Hulley, E. B.; Mock, M. T.; Appel, A. M.; Linehan, J. C. *ACS Catal.* **2014**, *4*, 3755-3762.

41. Kumar, N.; Camaioni, D. M.; Dupuis, M.; Raugei, S.; Appel, A. M. *Dalton Trans.* **2014**, *43*, 11803-11806.

42. Jeletic, M. S.; Hulley, E. B.; Helm, M. L.; Mock, M. T.; Appel, A. M.; Wiedner, E. S.; Linehan, J. C. *ACS Catal.* **2017**, *7*, 6008-6017.

43. Rail, M. D.; Berben, L. A. *J. Am. Chem. Soc.* **2011**, *133*, 18577-18579.

44. Taheri, A.; Thompson, E. J.; Fettinger, J. C.; Berben, L. A. *ACS Catal.* **2015**, *5*, 7140-7151.

45. Kang, P.; Zhang, S.; Meyer, T. J.; Brookhart, M. *Angew. Chem. Int. Ed.* **2014**, *53*, 8709-8713.

46. Kang, P.; Cheng, C.; Chen, Z.; Schauer, C. K.; Meyer, T. J.; Brookhart, M. *J. Am. Chem. Soc.* **2012**, *134*, 5500-5503.

47. Kang, P.; Meyer, T. J.; Brookhart, M. *Chem. Sci.* **2013**, *4*, 3497-3502.

48. Roy, S.; Sharma, B.; Pécaut, J.; Simon, P.; Fontecave, M.; Tran, P. D.; Derat, E.; Artero, V. *J. Am. Chem. Soc.* **2017**, *139*, 3685-3696.

49. Ceballos, B. M.; Yang, J. Y. *Proc. Natl. Acad. Sci.* **2018**, *115*, 12686-12691.

CHAPTER 1:

Reversible CO_2/HCO_2^- Electrocatalysis near the Thermodynamic Potential

Introduction*

Reversible catalysis between energy storage and utilization reactions has been called a 'holy grail' in catalysis,[1] and can only be achieved by levelling the energy landscape of the catalytic cycle. The definitions of bi-directional versus reversible catalysis were recently described.[2] Electrocatalysts that function for both reduction and oxidation reactions are considered bi-directional; however, they are only reversible if they operate at a minimal overpotential in both directions. Reversible reactivity indicates minimal changes in free energy between intermediates, coupled with low transition-state barriers.

The prototypical example of a reversible electrocatalyst is platinum, which facilitates H_2 production and oxidation at negligible overpotentials.[3] In nature, hydrogenase enzymes also display reversible electrocatalytic activity and operate near the thermodynamic potential, although different variants display bias towards either H^+ reduction or H_2 oxidation.[4-5] More recently, a few synthetic catalysts have achieved reversible $2H^+/H_2$ electrocatalysis. [6-8]

Research in H_2 electrocatalysis is motivated by the prospect of storing renewable electricity in a chemical bond. However, challenges associated with using a gaseous fuel has stimulated interest in applying renewable electricity to recycle CO_2 to liquid fuels.[9] One solution is the reduction of CO_2 to HCO_2^- (formate; eq 1.1), a soluble fuel more convenient for storage

---

* Portions of this chapter have been published: Cunningham, D. W.; Barlow, J. M.; Velasquez, R. S.; Yang, J. Y. *Angew. Chem. Int. Ed.* Published online December 17, 2019, DOI: 10.1002/anie.201913198.

and transportation.[10-11] The reverse reaction, electrocatalytic oxidation of HCO_2^-, is valuable in fuel cell applications.[10-11]

$$CO_2 + H^+ + 2e^- \rightleftharpoons HCO_2^- \quad (1.1)$$

Kang and co-workers recently described the electrocatalytic activity of bi-directional CO_2/HCO_2^- electrocatalysis with an iridium pincer compound.[12] Although the compound catalyzed both the reduction and oxidation reactions, the onset potentials are separated by ca. 1 V. Koper and coworkers described the electrocatalytic activity of Pd–Pt nanoparticles towards CO_2 reduction to formic acid at low overpotentials with a maximum Faradaic efficiency of 88%, with the balance of electrons contributing to H_2 evolution.[13] Electrocatalysis of the reverse reaction, formic acid oxidation, was also observed. However, the Pd–Pt nanoparticle catalyst suffered from deactivation by CO intermediates in both directions. Prior to this work, stable, highly selective, reversible catalysis at minimal overpotentials for CO_2 to HCO_2^- interconversion had only ever been observed in two formate dehydrogenase (FDH) enzymes that were attached to an electrode surface: Mo-dependent FDH from *Escherichia coli* (*Ec*FDH-H)[14] and W-dependent FDH from *Syntrophobacter fumaroxidans*.[15]

Guided by thermodynamic considerations, we describe a selective and reversible synthetic electrocatalyst for CO_2/HCO_2^- conversion. Transition-metal catalyzed CO_2 reduction to HCO_2^- most commonly proceeds through the following steps: 1) reduction of the metal pre-catalyst 2) protonation to generate a metal-hydride complex, and 3) hydride transfer to form a C–H bond.[16-22] For a reversible catalyst, HCO_2^- oxidation follows the microscopic reverse and each step must be close to equilibrium. A prospective catalyst and acid source were selected to minimize the free energy of the third and second step, respectively. Stoichiometric and electrochemical experiments verified chemical and electrocatalytic reversibility. The free-energy

change for each chemical step was determined through equilibrium measurements to be ≤1 kcal/mol for a net energy change of 1.1 kcal/mol, equivalent to a 48 mV overpotential. The experimentally derived energy landscape delineates how the free energies of each step contribute to the catalyst overpotential, illustrating how both catalyst and acid selection are key to minimizing the catalytic overpotential.

The catalyst not only reduces CO_2 to HCO_2^- near the thermodynamic potential, but does so with high selectivity (no direct H^+ reduction to H_2 is observed). We found that under conditions optimized for reversible catalysis, H_2 evolution is endergonic, leading to high Faradaic efficiency for HCO_2^-. We found that when the acid source is selected to minimize the free energy of protonation (and thus operate at the lowest possible overpotential for the catalyst), H_2 evolution is nearly always endergonic, leading to high selectivity. These results demonstrate how flattening the energy landscape leads to more efficient and more selective catalysis.

Results and Discussion

The free energy of hydride transfer from a transition-metal hydride to generate HCO_2^- (from CO_2) is described by their hydricities, or ΔG^o_{H-}, as shown in eqs 1.2 and 1.3. Thus, to minimize the free energy for hydride transfer to CO_2, the hydricity of the transition-metal hydride should closely match the hydricity of formate.

$$[MH]^{n+} + CO_2 \rightleftharpoons [M]^{n+1} + HCO_2^- \quad (1.2)$$

$$\Delta G^o_{rxn} = \Delta G^o_{H-}([MH]^{n+}) - \Delta G^o_{H-}(HCO_2^-) \quad (1.3)$$

DuBois and co-workers measured the hydricity of $[HPt(depe)_2]^+$ (depe = 1,2-*bis*(diethylphosphino)ethane), or **[HPt]**$^+$ (Scheme 1.1), to be 44 kcal/mol[23] and later noted that

although **[HPt]**$^+$ reacts with CO_2 to form sub-stoichiometric amounts of HCO_2^-, **[HPt]**$^+$ could also be generated by addition of HCO_2^- to $[Pt(depe)_2]^{2+}$, or **[Pt]**$^{2+}$ (Scheme 1.1).[24] Based on these observations, it was evident that the hydricity of **[HPt]**$^+$ is comparable to that of HCO_2^-, although its catalytic activity was not explored. The similar thermodynamic hydricities of **[HPt]**$^+$ and HCO_2^- makes the former an ideal candidate for reversible reactivity.

Scheme 1.1 Proposed catalytic cycle and abbreviations

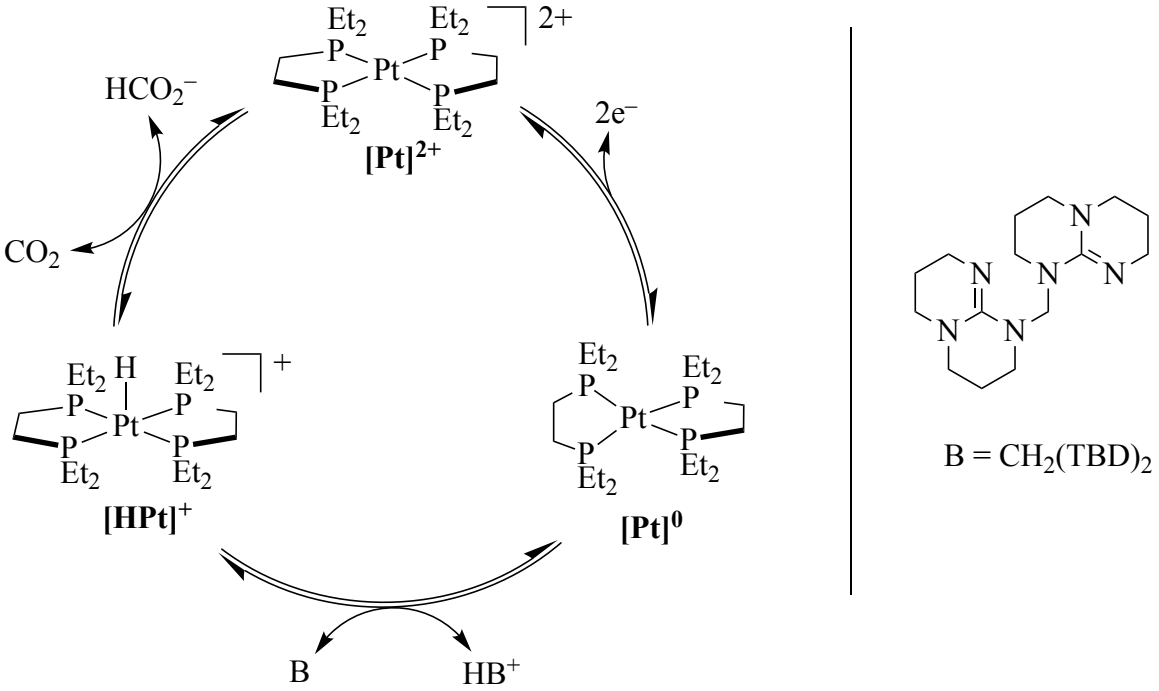

Hydride transfer equilibria. In order to confirm the free energy for hydride transfer from **[HPt]**$^+$ to CO_2, the equilibria for each hydride donor/acceptor pair in the forward and reverse direction (**[HPt]**$^+$/CO_2 and **[Pt]**$^{2+}$/HCO_2^-, respectively) were studied. Addition of CO_2 (1 atm) to an acetonitrile solution of **[HPt]**$^+$, resulted in the formation of **[Pt]**$^{2+}$ in a 16/1 ratio of **[Pt]**$^{2+}$/**[HPt]**$^+$ (Figure 1.1), as indicated by $^{31}P\{^1H\}$ NMR spectroscopy; this corresponds to a K_{eq} of 1.1. Note that the resonances appear as a triplet due to coupling with the 33% abundant NMR-active ^{195}Pt nucleus. This discrepancy for the reaction to favor the formation of **[Pt]**$^{2+}$ is

attributed to the high solubility of CO_2 in acetonitrile (280 mM).[25] This reaction was done in triplicate and the tabulated data for each experiment can be seen in entries 1–3 of Table 1.1.

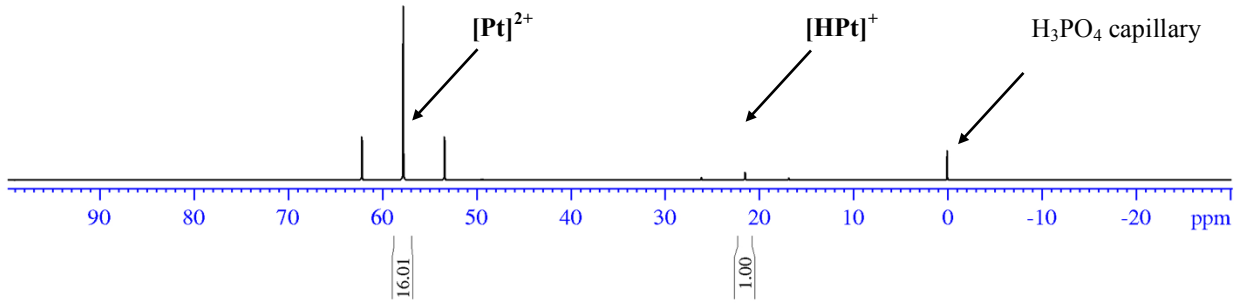

Figure 1.1. $^{31}P\{^{1}H\}$ NMR spectrum for the reaction of **[HPt]**$^{+}$ (20 mM) with CO_2 (1 atm) in CH_3CN.

If the reaction **[HPt]**$^{+}$ and CO_2 is indeed at thermodynamic equilibrium, then the reverse reaction of hydride transfer from HCO_2^- to **[Pt]**$^{2+}$ should yield the same K_{eq} values. Equilibration of an acetonitrile solution of HCO_2^- with an equimolar amount of **[Pt]**$^{2+}$ under a CO_2 atmosphere yielded identical ratios for **[Pt]**$^{2+}$/**[HPt]**$^{+}$ as before, 16.1; Figure 1.2) and a K_{eq} of 1.1. It is important to note that in order to achieve standard state conditions, this experiment was done under an atmosphere of CO_2. This experiment was done in duplicate and the tabulated data can be seen in entries 4 and 5 of Table 1.1. Due to the fact that identical K_{eq} values were yielded independent of the direction the reaction is approached from, this demonstrates that the hydride transfer step is at thermodynamic equilibrium.

The free energy for hydride transfer from **[HPt]**$^{+}$ to CO_2 was determined to be –0.028 kcal/mol from the previously discussed hydride transfer experiments. This free energy is consistent with what is expect from the identical hydricity values of 44 kcal/mol for both **[HPt]**$^{+}$

and HCO_2^- and verifies that there is minimal change in the free energy landscape for this particular step.

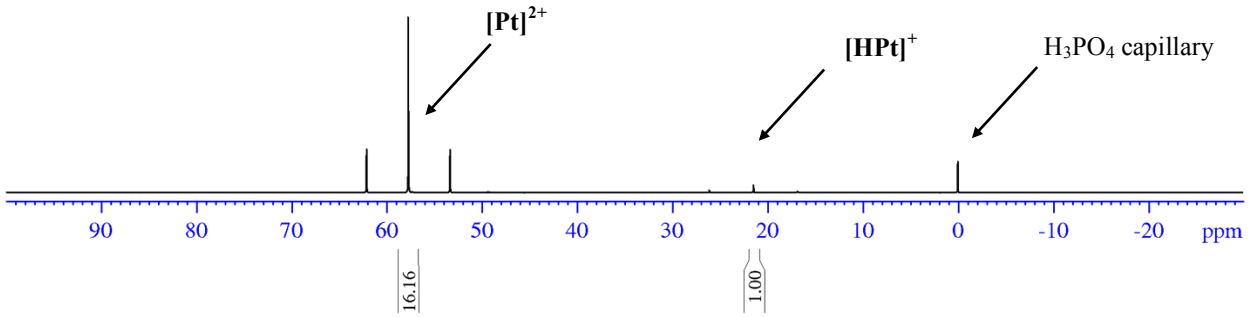

Figure 1.2. $^{31}P\{^1H\}$ NMR spectrum for the reaction of **[Pt]$^{2+}$** (20 mM) with [*n*-Bu$_4$][HCO_2^-] (20 mM) in CH_3CN under CO_2 (1 atm).

Table 1.1. Tabulated Data for Determination of K_{eq} and ΔG^o_{rxn} for the Reaction of [HPt]$^+$/CO_2 and the Microscope Reverse, [Pt]$^{2+}$/HCO_2^-

entry	[**HPt$^+$**]$_i$[a]/mM	[**Pt^{2+}**]$_i$[a]/mM	[HCO_2^-]$_i$[a]/mM	$\frac{[\mathbf{Pt^{2+}}]_{eq}}{[\mathbf{HPt^+}]_{eq}}$[b]	x[c]	K_{eq}	ΔG^o_{rxn}/ kcal/mol
1	20.0	0	0	16.0	18.8	1.08	–0.044
2	20.0	0	0	17.2	18.9	1.16	–0.087
3	20.0	0	0	14.5	18.7	0.965	0.021
4	0	20.0	20.0	16.0	18.8	1.07	–0.042
5	0	20.0	20.0	14.7	18.7	0.981	0.011
					Average =	1.05	–0.028

[a]Subscripts "i" and "eq" represent initial amounts and equilibrium amounts, respectively. [b]Experimental ratio determined by the relative integrations of the two resonances in the $^{31}P\{^1H\}$ spectrum. [c]*x*, or change in equilibrium concentration, calculated from the equilibrium expression and the $^{31}P\{^1H\}$ integrations; see Experimental section for derivation and sample calculation.

Selection of Acid/Base Conjugate Pair. In order to generate **[HPt]$^+$** for CO_2 reduction, an acid with a suitable pK_a is required. Similarly, the microscopic reverse, HCO_2^- oxidation, requires a base for deprotonation of **[HPt]$^+$** to form **[Pt]^0**. DuBois and colleagues have previously measured the pK_a of **[HPt]$^+$** in acetonitrile and determined it to be 29.7.[23] An acid/base conjugate pair with a pK_a within 1 unit of **[HPt]$^+$** would be the ideal candidate for achieving reversible reactivity which could be achieved by varying the amount of acid or base.

To avoid the formation of H_2, resulting from protonation of **[HPt]**$^+$, we utilize a thermochemical scheme to calculate the pK_a required such that protonation of **[Pt]**^{0} is favorable while the free energy for the hydrogen-evolution reaction, or ΔG^o_{HER}, is unfavorable. As discussed in the Chapter 0: Introduction, summation of eqs 0.6–0.8 in Table 0.1 yields the equation for ΔG^o_{HER} (eq 0.9); by setting this sum to be >0 kcal/mol, the pK_a required was calculated to be >23.5. This means that as long as the choice of acid has a pK_a in the range of 23.5–29.7, adventitious H_2 production will be unfavorable, while still allowing for protonation of **[Pt]**^{0}.

To meet all of the criteria of having comparable pK_a to **[HPt]**$^+$, for reversibility, as well as avoid H_2 formation, this restricts us to an acid/base conjugate pair that has a pK_a in the range of 28.7–30.7. To this end, $CH_2(TBD)_2$ (eq 1.8; TBD = 1,5,7-triazabicyclo[4.4.0]dec-5-ene) which has a reported pK_a of 29.0 was chosen.[26] In addition to having a suitable pK_a, $CH_2(TBD)_2$ was chosen due its relative ease of synthesis from the S_N2 reaction of the readily available precursor, TBD, and CH_2Cl_2 (eq 1.8).[27] The conjugate acid, or $CH_2(TBD)_2{\bullet}H^+$, can also readily be prepared as the $[PF_6]^-$ salt by addition of $[NH_4][PF_6]$ to $CH_2(TBD)_2$.

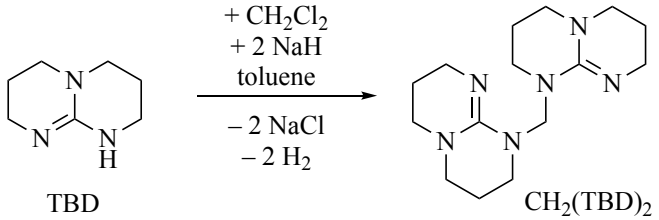

(1.4)

The stoichiometric reaction of $CH_2(TBD)_2$ and **[HPt]**$^+$ was studied by $^{31}P\{^1H\}$ NMR spectroscopy in order to show that the process is at equilibrium and to confirm the pK_a, and the corresponding free energy to what is reported in the literature. Addition of $CH_2(TBD)_2$ to an equimolar amount of **[HPt]**$^+$ resulted in a ratio of **[Pt]**^{0}/**[HPt]**$^+$ of 0.40 (Figure 1.3, top), which

corresponds to a K_{eq} of 0.16 and a ΔpK_a of 0.80. This is in good agreement with the theoretical K_{eq} expected for a difference of pK_a values of 0.7, which was calculated to be 0.20. To confirm that this process is indeed at thermodynamic equilibrium, an identical experiment was performed that only varied the amount $CH_2(TBD)_2$ added (ca 0.3 equiv) and yielded comparable K_{eq} values. The free energy for this step was calculated to be 1.07 kcal/mol. Table 1.2 contains a summary of the K_{eq} and ΔG^o values, in addition to any associated parameters used for calculations.

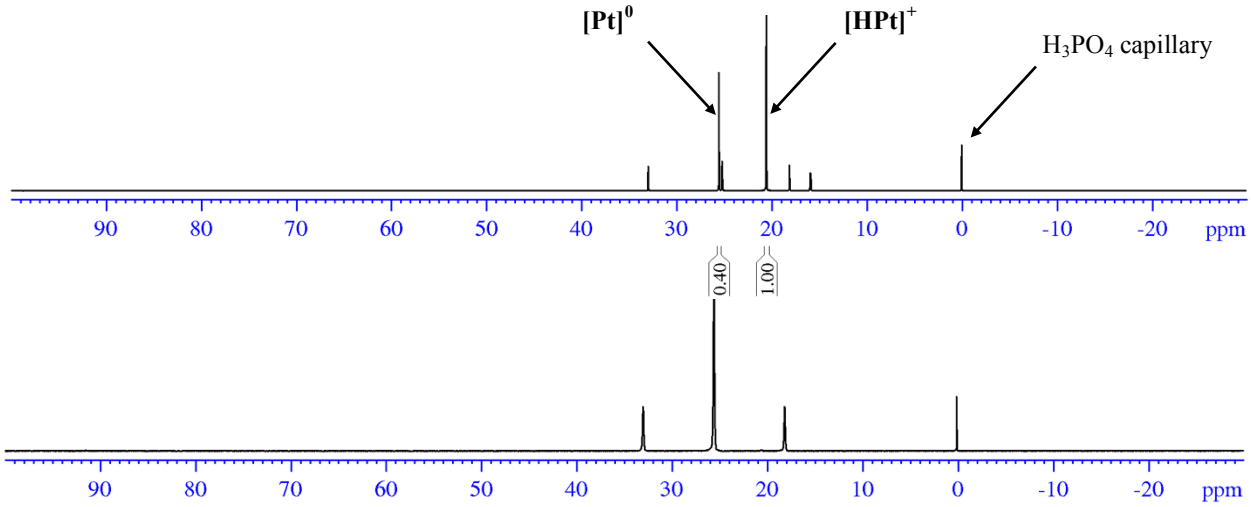

Figure 1.3. $^{31}P\{^1H\}$ NMR spectra of reaction with **[HPt]**$^+$ (30 mM) and $CH_2(TBD)_2$ (30 mM) (top) and independently-isolated **[Pt]**^{0} (bottom).

Table 1.2. K_{eq} Values for the Deprotonation of [HPt]$^+$ by $CH_2(TBD)_2$.

$[\mathbf{HPt}^+]_i$[a]/mM	$[CH_2(TBD)_2]_i$[a]/mM	$\frac{[\mathbf{Pt}^0]_{eq}}{[\mathbf{HPt}^+]_{eq}}$[b]	x[c]	K_{eq}	ΔG^o_{rxn}/ kcal/mol
29.9	30.0	0.398	0.00851	0.158	1.09
29.3	10.0	0.251	0.00587	0.168	1.06
			Average=	0.163	1.07

[a]Subscripts "i" and "eq" represent initial amounts and equilibrium amounts, respectively. [b]Experimental ratio determined by the relative integrations of the two resonances in the $^{31}P\{^1H\}$ spectrum. [c]*x,* or change in equilibrium concentration, was calculated from the equilibrium expression and the $^{31}P\{^1H\}$ integrations; see Experimental section for derivation and K_{eq} calculation.

CO_2 Reduction. The first step in the proposed catalytic cycle for CO_2 reduction is the 2-electron reduction of **[Pt]**$^{2+}$ to generate **[Pt]**^{0}. The Pt(II/0) oxidation states are separated by a 2-electron couple at –1.64 V vs Fc^+/Fc in acetonitrile, as shown in the black trace of Figure 1.4a.[23] Upon addition of $CH_2(TBD)_2{\bullet}H^+$ (1.0–5.0 equiv; Figure 1.4a), the peak current of the anodic return wave, or i_{pa}, is attenuated; this is consistent with protonation of the reduced platinum species, **[Pt]**^{0}, to form **[HPt]**$^{+}$, or an electron transfer chemical step (EC) reaction. The extent of protonation is dependent on the concentration of $CH_2(TBD)_2{\bullet}H^+$; after the addition of 10 equiv no cathodic peak is observed on the return scan (Figure 1.4b, blue trace).

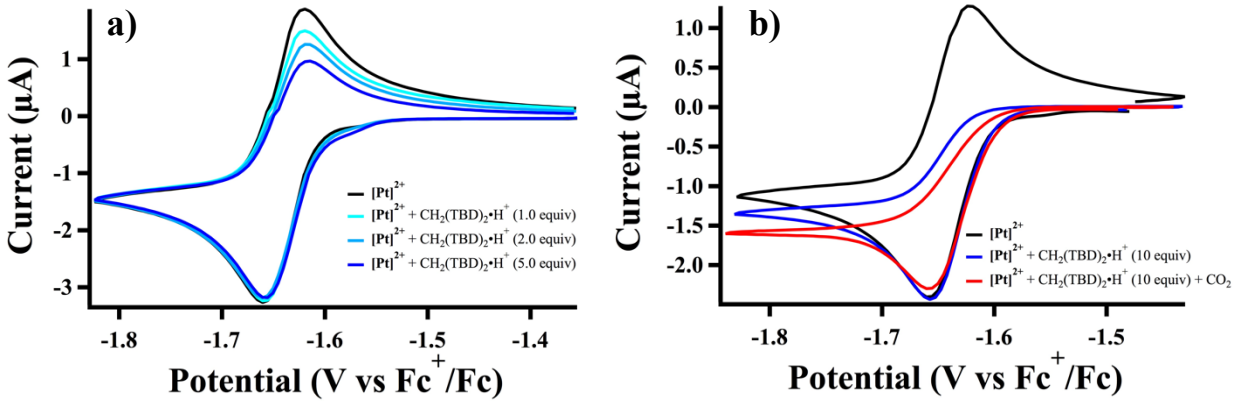

Figure 1.4. Cyclic voltammograms of (a) the titration of **[Pt]**$^{2+}$ (0.98 mM) with $CH_2(TBD)_2{\bullet}H^+$ (0–5 equiv) with scan rate of 0.025 V/s and (b) **[Pt]**$^{2+}$ (1.0 mM) with $CH_2(TBD)_2{\bullet}H^+$ (10 equiv) and under a CO_2 atmosphere at a scan rate of 0.01 V/s. All CVs shown are in $CH_3CN/TBAPF_6$ (0.2 M).

After addition of $CH_2(TBD)_2{\bullet}H^+$ and upon addition of CO_2, no current enhancement is observed (Figure 1.4b, red trace). The lack of current This suggests that there is either a) no catalysis occurring or b) catalysis is occurring at a rate much slower than the timescale of the CV measurements.

To test the electrocatalytic activity of **[Pt]**$^{2+}$ for the reduction of CO_2 to HCO_2^-, we moved to controlled-potential electrolysis (CPE) which can be done at much longer timescales

than CV measurements. A CO_2-saturated solution of $\mathbf{[Pt]^{2+}}$ (0.0101 mmol) and $CH_2(TBD)_2{\bullet}H^+$ (0.100 mmol) was electrolyzed at –2.0 V vs Fc^+/Fc for 5 h and resulted in a total charge passed of 11.3 C (Figure 1.5a); thus, the theoretical amount of formate that could have been produced was calculated to 0.058 mmol. An aliquot of CPE solution after electrolysis was analyzed by ^1H NMR spectroscopy and the amount of HCO_2^- produced was determined to be 0.056 mmol by integrating relative to a 1,3,5-tri-*tert*-butylbenzene standard (Figure 1.5b). An equivalent CPE in the absence of catalyst resulted in negligible charge being passed (Figure 1.5a, blue trace). The Faradaic efficiency for the process was 97% and the turnover number was 5.5.

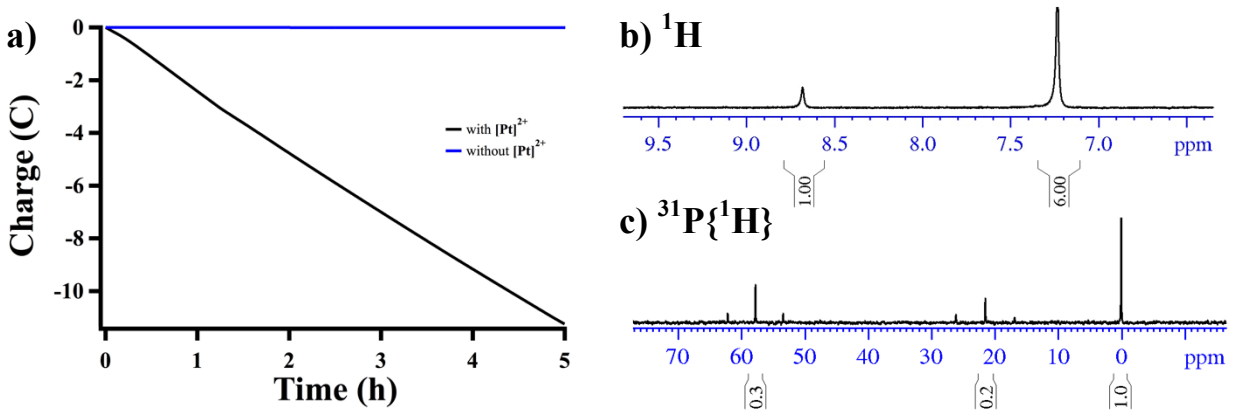

Figure 1.5. Charge passed during CPE of $\mathbf{[Pt]^{2+}}$ (0.0101 mmol) with $CH_2(TBD)_2{\bullet}H^+$ (0.100 mmol, 10 equiv) and CO_2 (1 atm). (b) ^1H NMR Spectrum of an aliquot of post-electrolysis solution (1.00 mL) containing 1,3,5-tri-*tert*-butylbenzene (6.7 mg, 0.027 mmol) and (c) $^{31}P\{^1H\}$ NMR spectra of same aliquot of post-electrolysis solution containing an H_3PO_4/D_2O external capillary as an integration standard.

The resonances pertaining to all platinum species (i.e. $\mathbf{[HPt]^+}$, $\mathbf{[Pt]^{2+}}$, and $\mathbf{[Pt]^0}$) in the $^{31}P\{^1H\}$ NMR spectrum were integrated relative to an external capillary containing H_3PO_4/D_2O in order to determine whether the total concentration of platinum species is conserved. The total concentration of platinum species relative to integration standard in the post-electrolysis solution

was 0.5:1.0 (Figure 1.5c); the amount of total platinum species to standard pre-electrolysis was 1.0:1.0. The total concentration appeared to go down by a factor of two, but this is attributed to a two-fold dilution of the working solution during electrolysis. This indicates that the catalyst is not degrading under CPE conditions or forming catalytically active nanoparticles. In addition, electrolysis was performed over a pool of mercury, suggesting catalysis is not proceeding via the formation of nanoparticles.[28]

These results show that $\mathbf{[Pt]^{2+}}$ is a selective, homogeneous electrocatalyst for the reduction of CO_2 to HCO_2^- with a turnover number (TON) of 5.5 and Faradaic efficiency of 97% under these conditions.

In an attempt to accelerate catalysis, the stronger acid, TBD•H^+ (pK_a = 26.0), was utilized as the acid source.[29] This choice of acid still allows for unfavorable HER and if the rate-determining step involves protonation of $\mathbf{[Pt]^0}$, then it should also provide additional driving force for CO_2 reduction. CVs of $\mathbf{[Pt]^{2+}}$ are shown in Figure 1.6; upon addition of acid and CO_2, no current increase is observed. This suggests that catalysis is not drastically accelerated by the addition of stronger acid and that protonation of $\mathbf{[Pt]^0}$ might not be rate limiting. As expected, no catalytic H_2 formation is occurring even with an acid nearly 3 orders of magnitude stronger than $CH_2(TBD)_2$•H^+.

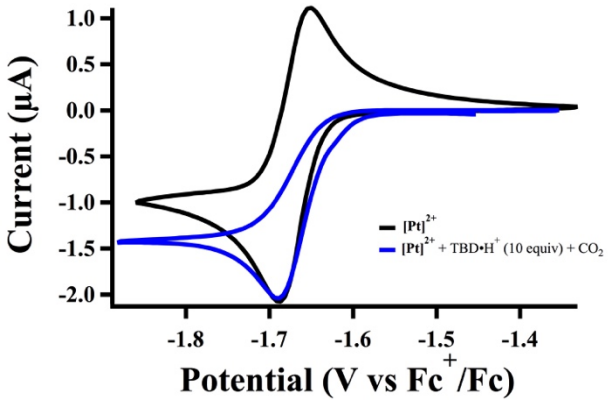

Figure 1.6. Cyclic voltammograms of **[Pt]**$^{2+}$ (1.0 mM) and in the presence of TBD•H^+ (10 equiv) with CO_2 (1 atm). All scans shown are at 0.010 V/s.

HCO_2^- oxidation. The reverse reaction of CO_2 reduction, electrocatalytic HCO_2^- oxidation, was investigated by cyclic voltammetry. A set of CV experiments containing **[HPt]**$^+$ in the presence of HCO_2^- (50 equiv) with the addition of base, $CH_2(TBD)_2$, can be seen in Figure 1.7a. It is important to note, that upon addition of $CH_2(TBD)_2$ to **[HPt]**$^+$, **[Pt]**^{0} is formed, thus the CVs start at more negative potentials than the $E_{1/2}$ and scans to more positive numbers (oxidatively) numbers before cycling back to more negative (reductively). As more $CH_2(TBD)_2$ is added, the peak current of the forward, anodic wave, gets larger. This is consistent with deprotonation of **[HPt]**$^+$ until ca. 50 equiv of $CH_2(TBD)_2$ is added and the current increase is negligible (Figure 1.6a, black trace) suggesting full deprotonation of **[HPt]**$^+$.

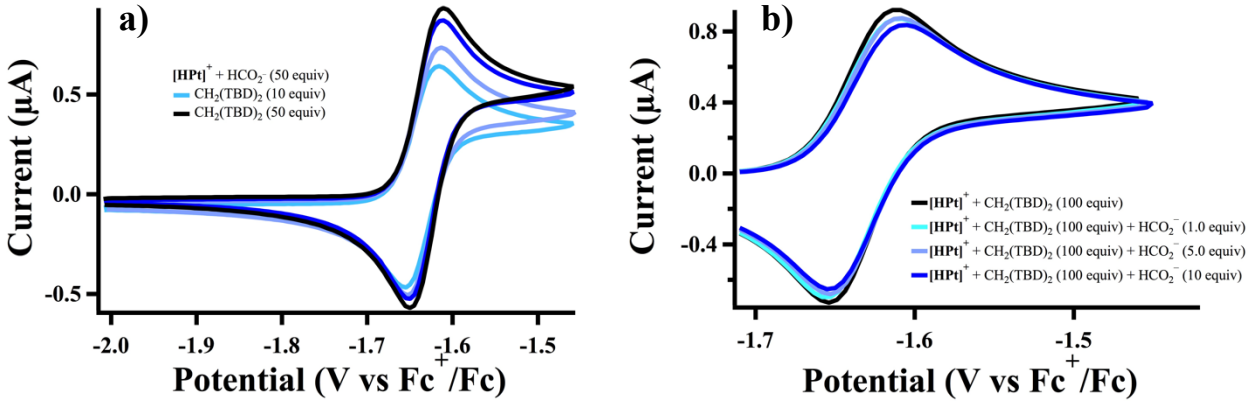

Figure 1.7. Cyclic voltammograms of (a) the titration of $\mathbf{[HPt]^+}$ (1.0 mM) and HCO_2^- (50 mM) with $CH_2(TBD)_2$ (10–50 mM) with scan rate of 0.005 V/s and (b) the titration of $\mathbf{[HPt]^+}$ (1.0 mM) and $CH_2(TBD)_2$ (100 mM) with HCO_2^- (1–10 mM) with scan rate of 0.005 V/. All CVs shown are in CH_3CN/$TBAPF_6$ (0.2 M).

A titration of $\mathbf{[HPt]^+}$ and $CH_2(TBD)_2$ with HCO_2^- was performed in an attempt to observe a catalytic current increase (Figure 1.6b). The large excess of $CH_2(TBD)_2$ (100 equiv) should fully deprotonate $\mathbf{[HPt]^+}$ to $\mathbf{[Pt]^0}$. Upon the addition of HCO_2^- (up to 10 equiv) no current increased was observed for the forward, anodic scan. As with the case for CO_2 reduction, this suggests that there is either no catalysis occurring, or that catalysis is much slower than the timescale of the CV measurements.

Controlled potential electrolysis at –1.4 V vs Fc^+/Fc of $\mathbf{[Pt]^{2+}}$ (0.0113 mmol), HCO_2^- (0.099 mmol), and $CH_2(TBD)_2$ (0.10 mmol) in acetonitrile resulted in a total charge of 5.71 C transferred throughout the electrolysis period (Figure 1.8a). The concentration of HCO_2^- in the post-electrolysis solution was determined to be 25.9 mM by spiking a 500 µL aliquot with C_6H_6 (2.30 µL, 0.0258 mmol). For the entire electrolysis solution of 2.80 mL, this corresponds to a total amount of HCO_2^- in the post-electrolysis solution of 0.0725 mmol; thus, the amount of

HCO_2^- consumed through the electrolysis was 0.027 mmol. Based on the charge passed of 5.71 C, the theoretical amount of HCO_2^- consumed was 0.030 mmol. The Faradaic efficiency for this electrocatalytic process was 90% and the turnover number was 2.4. An electrolysis experiment was performed under identical conditions, but lacking catalyst resulted in negligible charge being passed (Figures 1.8a, blue trace).

To rule out the formation of platinum nanoparticles, the total concentration of platinum species was measured before and after electrolysis by integrating the resonances in $^{31}P\{^1H\}$ NMR spectra relative to an external capillary standard containing H_3PO_4/D_2O. Figure 1.8c shows the $^{31}P\{^1H\}$ NMR spectrum recorded after electrolysis, the relative concentration of total platinum species to the external capillary standard was found to be 0.56:1.0. The total amount of platinum species before electrolysis relative to the exact same amount of external standard was 0.80:1.0. There does appear to be a discrepancy before and after electrolysis, however, the 1.4-fold decrease in total platinum concentration is attributed to dilution of the working solution from 2.0 mL to 2.8 mL. In addition, the CPE was performed over a pool of mercury, suggesting that catalysis is not a result of nanoparticle formation.[28]

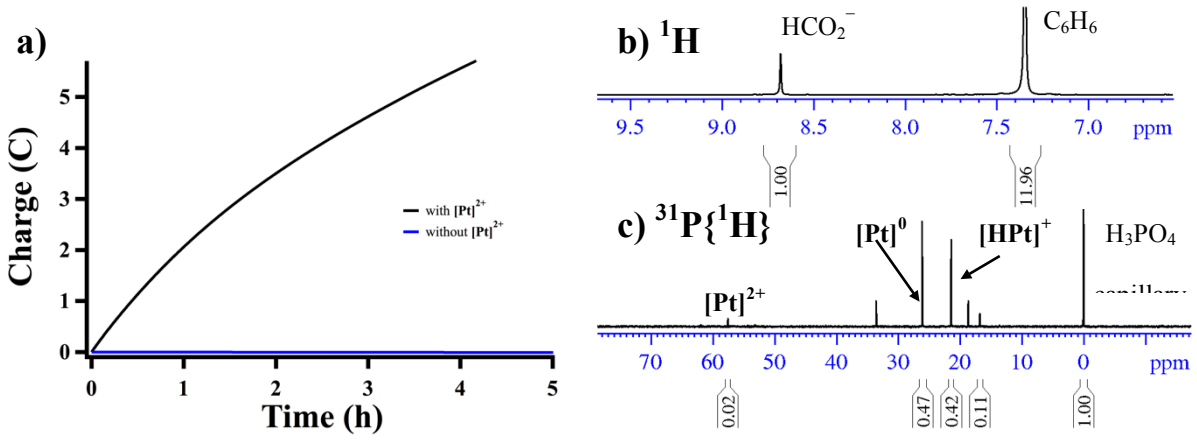

Figure 1.8. (a) Charge passed during CPE of $\mathbf{[Pt]^{2+}}$ (0.0113 mmol) with $CH_2(TBD)_2$ (0.10 mmol) and HCO_2^- (0.099 mmol). (b) ^1H NMR Spectrum of an aliquot of post-electrolysis

solution (500 μL) spiked with C_6H_6 (2.30 μL, 0.0258 mmol) and (c) $^{31}P\{^1H\}$ NMR spectra of same aliquot of post-electrolysis solution containing an H_3PO_4/D_2O external capillary as an integration standard.

The electrocatalytic data demonstrate **[HPt]**$^+$ is a selective electrocatalyst for the reversible conversion between CO_2 and HCO_2^-. According to the most recent estimate of the standard potential for CO_2/HCO_2^- in acetonitrile, the thermodynamic potential at a pK_a of 29.0 is −1.63 V vs Fc/Fc^+.[30] The overpotential calculated using the $E_{1/2}$ value for **[Pt]**$^{2+}$, as described by Appel et. al, is 10 mV.[31] We note that our controlled potential electrolysis experiments are performed at 300 mV past the potential of maximum current, or 'peak current', to generate sufficient product for accurate quantification and to avoid any drifts in potential that may occur throughout the electrolysis period.

The measured equilibrium constants of each intermediate step in our proposed catalytic cycle is represented as an energy landscape, shown in Figure 1.9. The energy for protonation of **[Pt]**^{0} to generate **[HPt]**$^+$ followed by CO_2 addition to form HCO_2^- and **[Pt]**$^{2+}$ is shown in kcal/mol. The free energy diagram is drawn at –1.64 V vs Fc^+/Fc, or the reversible two-electron couple for **[Pt]**$^{2+}$/**[Pt]**^{0}. At this potential, the two species are equal in energy. By our measured equilibrium constants, the difference between the initial species and final species varies by –1.1 kcal/mol, which is equivalent to an overpotential of 48 mV (1.0 kcal/mol is equivalent to 43 mV), slightly higher than expected from the calculation above (10 mv). A few sources of error are possible with the previously estimated thermodynamic potential. The latter relies on an estimate of the pK_a of formic acid in acetonitrile, which has not been experimentally measured. The calculation also relies on the accuracy of the pK_a of the $CH_2(TBD)_2{\bullet}H^+$ in acetonitrile, and the absence of any effects (such as homoconjugation) in which the pK_a would not precisely

represent the proton activity of the solution. We note that the overpotential for CO_2 reduction of 48 mV derived from our energy landscape is derived from internally consistent equilibrium values and is thus a more accurate representation of the overpotential. By both calculations, the overpotential is small, as would be expected for a reversible electrocatalyst.

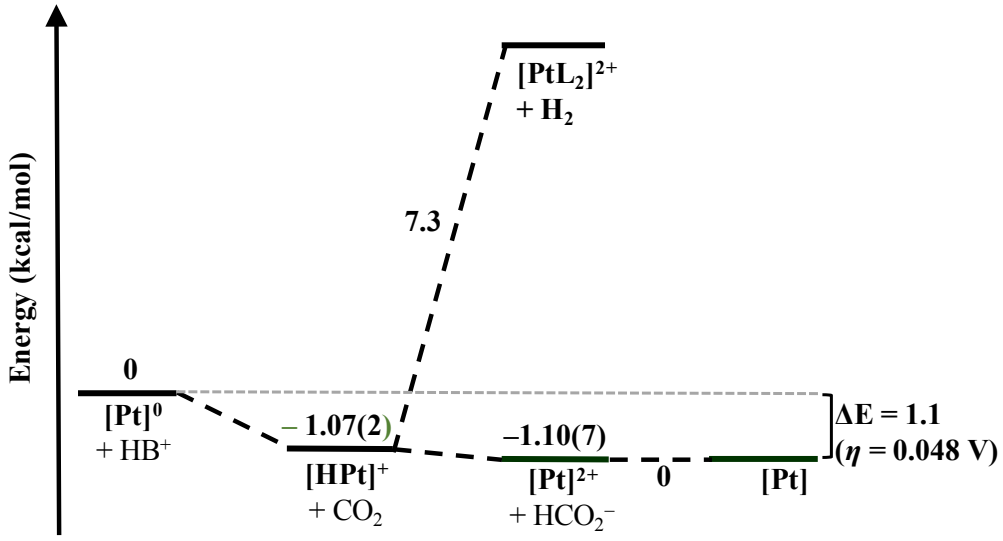

Figure 1.9. Energy landscape under catalytic conditions (pK_a of 29.0, 1 atm CO_2, and at –1.64 V vs Fc^+/Fc.

The derivation of the overpotential from the energy landscape depicts an essential tenant of efficient (and reversible) electrocatalysts – intermediate free energies must be minimized. For example, using a stronger acid than necessary for the protonation step would increase the overpotential by 59 mV, or 1.37 kcal/mol per excess pK_a unit. (This relationship is intuitive, as it is consistent with the change in thermodynamic potential by the Nernst equation for a single proton reaction). Perhaps less intuitively, using a stronger hydride donor than necessary for CO_2 reduction would also increase the overpotential by 43 mV per kcal/mol in excess free energy. The step-wise measurements in this system illustrate the energetic requirements for designing a

low-overpotential electrocatalyst. Additionally, our approach underscores the importance of quantifying thermodynamic parameters to minimize free energies.

Another noteworthy consequence of minimizing the free energies of intermediate steps is high selectivity for CO_2 reduction in the presence of protons. The free energy of H_2 evolution through protonation of the intermediate metal hydride can be quantified using the hydricity of the metal hydride, pK_a of the proton source, and the heterolytic bond formation of H_2 (a solvent-dependent constant). Although the acid/base pair in the system was selected to match that of the metal hydride to enable reversible catalysis, we find the free energy of H_2 evolution with this acid and the intermediate hydride to be endergonic by 7.3 kcal/mol.

Conclusion

By considering the thermodynamic driving force for each step and avoiding high- and low-energy intermediates we have shown that **[Pt]**$^{2+}$ is an electrocatalyst for both the reduction of CO_2 as well as the oxidation of HCO_2^-. This represents the first molecular electrocatalyst that exhibits reversible CO_2/ HCO_2^- reactivity.

Experimental

All manipulations were carried out under a dinitrogen atmosphere in dried glassware unless otherwise noted. All chemicals were used as received from commercial sources unless otherwise noted. All non-deuterated solvents were degassed by sparging with argon and then dried by passage through an alumina column under argon pressure on a Solvent Drying System (JC Meyer Solvent Systems) and stored over activated molecular sieves. Deuterated solvents were degassed by freeze-pump-thaw methods then dried over activated molecular sieves. **[Pt]$^{2+}$**,[32] **[HPt]$^{+}$**,[32] [*n*-Bu_4N][HCO_2],[33] TBD•HPF_6,[34] and $CH_2(TBD)_2$[27] were synthesized according to previously reported procedures.

NMR Spectroscopy. All NMR spectroscopy data were recorded on a Bruker AVANCE 600 MHz outfitted with a cryoprobe at 242.94 MHz for all $^{31}P\{^1H\}$ measurements and 600.13 MHz for all ^1H measurements. All ^1H NMR chemical shifts (δ) are reports in parts per million (ppm) downfield of tetramethylsilane and referenced to the residual protiated solvent peak (δ = 1.94 ppm for CD_3CN and 2.50 ppm for d_6-dmso). All $^{31}P\{^1H\}$ chemical shifts are reported in ppm downfield of H_3PO_4, which was inserted via an external capillary into the NMR tube. For NMR experiments in CH_3CN, an external capillary containing H_3PO_4/D_2O was inserted that served for locking and shimming as well as $^{31}P\{^1H\}$ NMR referencing. Quantitative ^1H NMR spectroscopy experiments were conducted with a delay time of 10 s and acquisition time of 5 s.

Hydride Transfer Equilibria. Stock solutions of **[Pt]$^{2+}$** (40 mM), **[HPt]$^{+}$** (40 mM), and [*n*-Bu_4N][HCO_2] (20 mM) were all prepared in a glovebox under a di-nitrogen atmosphere by weighing the corresponding solid directly into a 5.00 mL volumetric flask and dissolving in CH_3CN. For **[Pt]$^{2+}$** and HCO_2^- equilibration experiments, **[Pt]$^{2+}$** (250 μL) and HCO_2^- (250 μL) were each added to the same NMR tube and sealed with a rubber septum. For **[HPt]$^{+}$**, 500 μL of

the stock solution was put directly into an NMR tube and sealed with a rubber septum. The NMR tubes were then sparged with CO_2 (1 atm) for 60 sec each and NMRs were acquired. NMRs were acquired periodically until they came to equilibrium, which was generally <48 h.

$[HPt]^+$ Deprotonation Equilibrium. A solution of $CH_2(TBD)_2$ was prepared by recording the mass of $CH_2(TBD)_2$ (73.3 mg, 0.252 mmol) directly in a 5.00 mL volumetric flask followed by dissolution with CH_3CN (50.5 mM in $CH_2(TBD)_2$). **$[HPt]^+$** (22.5 mg, 0.0299 mmol) was then dissolved in the $CH_2(TBD)_2$ solution (592 μL) and then diluted with CH_3CN (108 μL) to make the total volume 700 μL. This was repeated by varying the volume of $CH_2(TBD)_2$ added to **$[HPt]^+$** and dilution with CH_3CN to make the finaly solution volume to be 700 μL.

Calculation of K_{eq}. The data for each experiment is explicitly shown and discussed in the Results and Discussion section above, however, a sample derivation for determining K_{eq} is shown here for the deprotonation of **$[HPt]^+$** and a base, B, in eq 1.8 below.

$$HPt^+ + B \rightleftharpoons Pt^0 + HB^+ \tag{1.5}$$

The directionality of the equilibrium is as shown in eq 1.2, thus K_{eq} is expressed as eq 1.10:

$$K_{eq} = \frac{[Pt^0]_{eq}}{[HPt^+]_{eq}} \bullet \frac{[HB^+]_{eq}}{[B]_{eq}} \tag{1.6}$$

Let x represent the concentration change at equilibrium, then K_{eq} can be expressed as eq 1.4:

$$K_{eq} = \frac{[Pt^0]_{eq}}{[HPt^+]_{eq}} \bullet \frac{x}{[B]_i - x} \tag{1.7}$$

The ratio $[Pt^0]_{eq}/[HPt^+]_{eq}$ is determined experimentally by $^{31}P\{^1H\}$ NMR integrations and the concentrations change at equilibrium, x, can be calculated:

$$\frac{[Pt^0]_{eq}}{[HPt^+]_{eq}} = \frac{x}{[HPt^+]_i - x} \rightarrow x = \frac{[HPt^+]_i \frac{[Pt^0]_{eq}}{[HPt^+]_{eq}}}{\left(1 + \frac{[Pt^0]_{eq}}{[HPt^+]_{eq}}\right)} \quad (1.8)$$

With x determined, K_{eq} is then calculated from eq 1.11.

Cyclic voltammetry. CVs were performed on a Pine Wavedriver 10 potentiostat with AfterMath software, using a 1 mm diameter glassy carbon disc working electrode and glassy carbon rod counter electrode. A Ag/Ag^+ pseudo-reference electrode containing a silver wire submerged in 0.2 M [*n*-Bu_4N][PF_6] separated from the bulk solution by a Vycor tip was used in addition to an internal ferrocene reference.

Controlled potential electrolysis. CPE experiments were performed in a small-volume H-cell. The working and counter compartments were separated by a fine glass frit. Each of the two compartments tops were threaded (GL18 and GL25) and were sealed with a cap containing a PTFE-faced silicone septum. The working compartment contained an acetonitrile solution of reagents, catalyst, and 0.2 M [*n*-Bu_4N][PF_6] (ca. 2 mL for a typical experiment) along with a vitreous carbon foam working electrode. The counter compartment contained an acetonitrile solution of 0.2 M [*n*-Bu_4N][PF_6] along with a coiled nichrome wire counter electrode and a Ag/Ag^+ pseudo-reference electrode with a silver wire submerged in 0.2 M [*n*-Bu_4N][PF_6] separated from the bulk solution by a Vycor tip. In a typical experiment, CVs were recorded and the potential was set ca. 0.3 V more negative (CO_2 reduction) or positive (HCO_2^- oxidation) of the $E_{1/2}$ of the Pt(II/0) couple. After the electrolysis period the volume in the working compartment was carefully measured with a graduated cylinder to account for any dilution that resulted from pressurization throughout the electrolysis. Analyzing the headspaces by GC show negligible formation of H_2 for all CPE experiments.

$CH_2(TBD)_2$•HPF_6. This synthesis was based on the modified literature report which synthesized the analogous compounds with Cl^- and BPh_4^- counter anions.[35] A solution of $CH_2(TBD)_2$ (123 mg, 0.425 mmol) in CH_3CN (5 mL) was added to $[NH_4][PF_6]$ and stirred for 2 h. The solution was then reduced in vacuo to yield a colorless, tacky solid. The tacky solid was dissolved in a minimal amount of toluene and placed in a freezer at –35 ºC; this yielded colorless crystals of $CH_2(TBD)_2$•HPF_6 (181 mg, 0.415 mmol, 98% yield) that were washed thrice with ether and dried in vacuo. The ^1H NMR spectrum obtained was in agreement with previously reported data with the different counter anions.[35] ^1H NMR (d_6-dmso, 600 MHz): δ (ppm) = 13.40 (s br, 1H, N*H*), 4.77 (s, 2H, CH_2-bridging), 3.40 (t, 4H), 3.24 (t, 4H), 3.18 (m, 8H), 1.90 (quartet, 4H), 1.78 (quartet, 4H); $^{31}P\{^1H\}$ NMR (d_6-dmso, 243 MHz): δ (ppm) = –144 (m, PF_6).

References

1. Savéant, J.-M. *ACS Catal.* **2018**, *8*, 7608-7611.

2. Fourmond, V.; Wiedner, E. S.; Shaw, W. J.; Léger, C. *J. Am. Chem. Soc.* **2019**, *141*, 11269-11285.

3. Eftekhari, A. *Int. J. Hydrogen Energy* **2017**, *42*, 11053-11077.

4. Hexter, S. V.; Grey, F.; Happe, T.; Climent, V.; Armstrong, F. A. *Proc. Natl. Acad. Sci.* **2012**, *109*, 11516-11521.

5. Abou Hamdan, A.; Dementin, S.; Liebgott, P.-P.; Gutierrez-Sanz, O.; Richaud, P.; De Lacey, A. L.; Rousset, M.; Bertrand, P.; Cournac, L.; Léger, C. *J. Am. Chem. Soc.* **2012**, *134*, 8368-8371.

6. Smith, S. E.; Yang, J. Y.; DuBois, D. L.; Bullock, R. M. *Angew. Chem. Int. Ed.* **2012**, *51*, 3152-3155.

7. Priyadarshani, N.; Dutta, A.; Ginovska, B.; Buchko, G. W.; O'Hagan, M.; Raugei, S.; Shaw, W. J. *ACS Catal.* **2016**, *6*, 6037-6049.

8. Dutta, A.; Appel, A. M.; Shaw, W. J. *Nat. Rev. Chem.* **2018**, *2*, 244-252.

9. Seh, Z. W.; Kibsgaard, J.; Dickens, C. F.; Chorkendorff, I.; Nørskov, J. K.; Jaramillo, T. F. *Science* **2017**, *355*, eaad4998.

10. An, L.; Chen, R. *J. Power Sources* **2016**, *320*, 127-139.

11. Vo, T.; Purohit, K.; Nguyen, C.; Biggs, B.; Mayoral, S.; Haan, J. L. *ChemSusChem* **2015**, *8*, 3853-3858.

12. Bi, J.; Hou, P.; Kang, P. *ChemCatChem* **2019**, *11*, 2069-2072.

13. Kortlever, R.; Peters, I.; Koper, S.; Koper, M. T. M. *ACS Catal.* **2015**, *5*, 3916-3923.

14. Reda, T.; Plugge, C. M.; Abram, N. J.; Hirst, J. *Proc. Natl. Acad. Sci.* **2008**, *105*, 10654-10658.

15. Bassegoda, A.; Madden, C.; Wakerley, D. W.; Reisner, E.; Hirst, J. *J. Am. Chem. Soc.* **2014**, *136*, 15473-15476.

16. Kang, P.; Cheng, C.; Chen, Z.; Schauer, C. K.; Meyer, T. J.; Brookhart, M. *J. Am. Chem. Soc.* **2012**, *134*, 5500-5503.

17. Kang, P.; Zhang, S.; Meyer, T. J.; Brookhart, M. *Angew. Chem. Int. Ed.* **2014**, *53*, 8709-8713.

18. Loewen, N. D.; Neelakantan, T. V.; Berben, L. A. *Acc. Chem. Res.* **2017**, *50*, 2362-2370.

19. Taheri, A.; Berben, L. A. *Inorg. Chem.* **2016**, *55*, 378-385.

20. Roy, S.; Sharma, B.; Pécaut, J.; Simon, P.; Fontecave, M.; Tran, P. D.; Derat, E.; Artero, V. *J. Am. Chem. Soc.* **2017**, *139*, 3685-3696.

21. Ceballos, B. M.; Yang, J. Y. *Proc. Natl. Acad. Sci.* **2018**, *115*, 12686-12691.

22. Barlow, J. M.; Yang, J. Y. *ACS Cent. Sci.* **2019**, *5*, 580-588.

23. Curtis, C. J.; Miedaner, A.; Ellis, W. W.; DuBois, D. L. *J. Am. Chem. Soc.* **2002**, *124*, 1918-1925.

24. DuBois, D. L.; Berning, D. E. *Appl. Organomet. Chem.* **2000**, *14*, 860-862.

25. Fujita, E.; Szalda, D. J.; Creutz, C.; Sutin, N. *J. Am. Chem. Soc.* **1988**, *110*, 4870-4871.

26. Kaljurand, I.; Saame, J.; Rodima, T.; Koppel, I.; Koppel, I. A.; Kögel, J. F.; Sundermeyer, J.; Köhn, U.; Coles, M. P.; Leito, I. *J. Phys. Chem. A* **2016**, *120*, 2591-2604.

27. Oakley, S. H.; Coles, M. P.; Hitchcock, P. B. *Inorg. Chem.* **2003**, *42*, 3154-3156.

28. Whitesides, G. M.; Hackett, M.; Brainard, R. L.; Lavalleye, J. P. P. M.; Sowinski, A. F.; Izumi, A. N.; Moore, S. S.; Brown, D. W.; Staudt, E. M. *Organometallics* **1985**, *4*, 1819-1830.

29. Kaljurand, I.; Kütt, A.; Sooväli, L.; Rodima, T.; Mäemets, V.; Leito, I.; Koppel, I. A. *J. Org. Chem.* **2005**, *70*, 1019-1028.

30. Waldie, K. M.; Ostericher, A. L.; Reineke, M. H.; Sasayama, A. F.; Kubiak, C. P. *ACS Catal.* **2018**, *8*, 1313-1324.

31. Appel, A. M.; Helm, M. L. *ACS Catal.* **2014**, *4*, 630-633.

32. Miedaner, A.; DuBois, D. L.; Curtis, C. J.; Haltiwanger, R. C. *Organometallics* **1993**, *12*, 299-303.

33. Grills, D. C.; Farrington, J. A.; Layne, B. H.; Lymar, S. V.; Mello, B. A.; Preses, J. M.; Wishart, J. F. *J. Am. Chem. Soc.* **2014**, *136*, 5563-5566.

34. Yang, Z.-Z.; He, L.-N.; Miao, C.-X.; Chanfreau, S. *Adv. Synth. Catal.* **2010**, *352*, 2233-2240.

35. Coles, M. P.; Aragón-Sáez, P. J.; Oakley, S. H.; Hitchcock, P. B.; Davidson, M. G.; Maksić, Z. B.; Vianello, R.; Leito, I.; Kaljurand, I.; Apperley, D. C. *J. Am. Chem. Soc.* **2009**, *131*, 16858-16868.

CHAPTER 2:

Investigating the Kinetics for Electrocatalytic Reduction of CO_2 to HCO_2^- by a Selective Platinum Catalyst

Introduction

Utilizing renewable electricity for the reduction of CO_2 by transition-metal hydrides is a primary goal for the generation of sustainable fuels.[1-3] These processes require electrocatalysts to facilitate the formation of fuels. A significant challenge for this route is product selectivity. In addition to the various carbon-based by-products that can be formed, the formation of parasitic H_2 often occurs.[4-6] In Chapter 1, we reported the first example of an electrocatalyst, **[HPt]**$^+$, that reversibly and selectively interconverts CO_2 and HCO_2^- at minimal overpotentials. This electrocatalyst, **[HPt]**$^+$, joins a group of select few electrocatalysts capable of reducing CO_2 to HCO_2^- with Faradaic efficiencies of >90%: an iron carbonyl cluster by Berben and colleagues,[5,7-8] an iridium-pincer complex studied by Brookhart, Meyer, and Palmore[9-11], and a cobalt-P_2N_2 catalyst from Artero and co-workers.[12]

A detailed mechanistic understanding of the reduction of CO_2 to HCO_2^- is vitally important for rational and efficient catalyst design. To date, there are only a select few examples of experimental studies that probe the mechanism of CO_2 reduction to HCO_2^-. Of these examples, they primarily focus of kinetics for the *hydrogenation* of CO_2 (i.e. generating metal hydrides by addition of H_2 and a base) and not *electrocatalytic* reductions, which often go through different rate-determining steps. Recently, Hazari and colleagues have studied methods for accelerating the rate of CO_2 insertion into transition-metal hydrides supported by pincer-type

ligand scaffolds that reduced CO_2 to HCO_2^- (in stoichiometric reactions). They probed the nature of the transition state for this step. Their results represent some of the first experimental and fundamental studies on probing the nature of the C–H bond forming step.[13-14] By applying insight they gained they, they were able to accelerate the rate of CO_2 insertion (up to $\times 10^3$) into the metal hydrides they studied. The number of mechanistic studies for CO_2 insertion into metal hydrides are sparse.

In this chapter, we utilize stoichiometric reactions and electrochemical methods to study the kinetics of each step of the proposed cycle for electrocatalytic CO_2 reduction to HCO_2^- by the selective and reversible catalyst, **[HPt]**$^+$ (Scheme 1.1). Alternative mechanistic pathways are considered. Due to the fact that catalysis is slow, we do not see any significant current enhances by CV. Each individual step was studied using stoichiometric reactions and non-steady-state conditions. We anticipate these studies will aid in future development of selective and more efficient catalysts for the reduction of CO_2 to HCO_2^-.

Results and Discussion

Electron transfer rate constant. The electron transfer rate constant, k_s, was determined using the Butler–Volmer approach,[15] where the peak potential of the anodic, E_{pa}, and cathodic, E_{pc}, waves shift with increasing scan rate given by the relationship given in eqs 2.1 and 2.2:

$$E_{pc} = E° - \frac{0.78RT}{n\alpha F} + \frac{2.303RT}{n\alpha F}\log\left(k_s\sqrt{\frac{RT}{n\alpha F v D}}\right) \tag{2.10}$$

$$E_{pa} = E° + \frac{0.78RT}{n(1-\alpha)F} + \frac{2.303RT}{n(1-\alpha)F}\log\left(k_s\sqrt{\frac{RT}{n(1-\alpha)F v D}}\right) \tag{2.11}$$

Where E^o is the formal reduction potential, R is the ideal gas constant, T is the absolute temperature, n is the number of electrons transferred, F is Faraday's constant, α is the so-called charge transfer coefficient, v is the scan rate, and D is the diffusion constant. Electron transfer parameters (α and k_s) are determined by plotting E_p against the log of the scan rate. α is first calculated from the slope of the linear fit and then k_s is calculated from the y-intercept of each plot and reported as an average of the two.

In order to calculate the electron transfer rate constant, the diffusion coefficient, D, must first be determined. This is calculated from the Randles-Sevchik equation,[16] which describes the linear relationship for peak current a function of the square root of the scan rate:

$$i_p = 0.4463nFAC\sqrt{\frac{nFvD}{RT}} \tag{2.12}$$

Where n, F, C, D, R, and T are the same as previously defined; A is the electrode surface area in units of cm^2 and C is the concentration in units of mol/cm^3.

The variable-scan-rate CVs for $\mathbf{[Pt]^{2+}}$ can be seen in Figure 2.1a. From this data, the peak currents for the cathodic and anodic waves were plotted as the square root of the scan rate (Figure 2.1b) and D was calculated from the slope of each line and found to be 6.28×10^{-6} and 4.71×10^{-6} cm^2/s for the reduction and oxidation events, respectively.

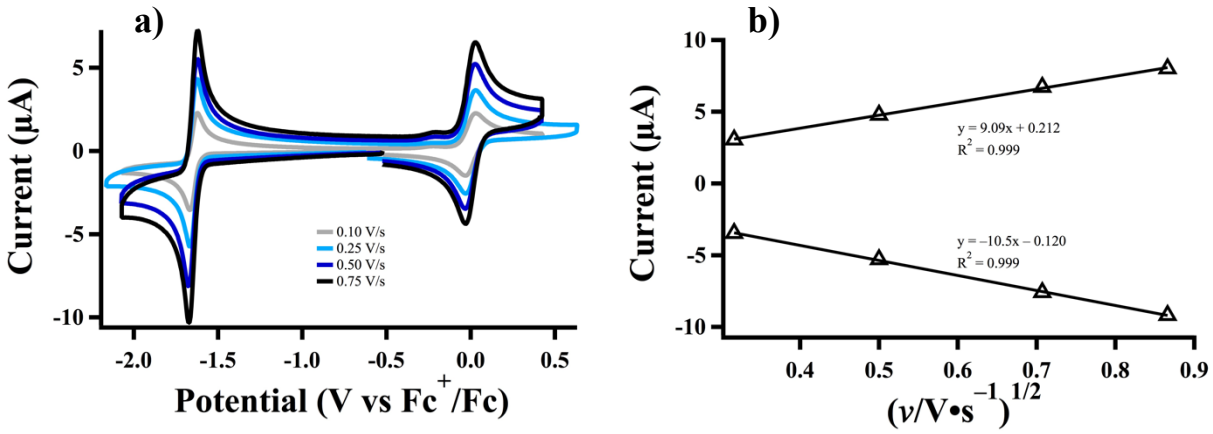

Figure 2.1. (a) Variable scan-rate CVs for **[Pt]**$^{2+}$ (0.501 mM) in CH_3CN and (b) peak currents plotted as a function of the square root of scan rate for calculation of diffusion coefficient.

As the scan rate, v, is increased and begins to exceed the diffusion of the species to and from the electrode, the change in peak potential, or ΔE_p, becomes larger and displays a linear relationship with the log(v). The scan-rate dependent CVs for **[Pt]**$^{2+}$ at higher scan rates can be seen in Figure 2.2a and their corresponding peak potentials are shown in Figure 2.2b. From the slope of the linear portion of the cathodic wave, the electron transfer symmetry coefficient, α, was determined to be 0.20.

The electron transfer rate constant, k_s, was then calculated from the y-intercepts of both the cathodic and anodic waves and determined to be 0.028 and 0.11 cm/s and is typically reported as an average, thus k_s = 0.069 cm/s. Using the same CVs, the electron transfer rate constant for ferrocene was determined to be 0.32 cm/s, which is in good agreement with the k_s often reported in the literature of 0.25 cm/s.[17] These experiments indicate that the rate of electron transfer to **[Pt]**$^{2+}$ is comparable to that of ferrocene, which is generally considered fast.

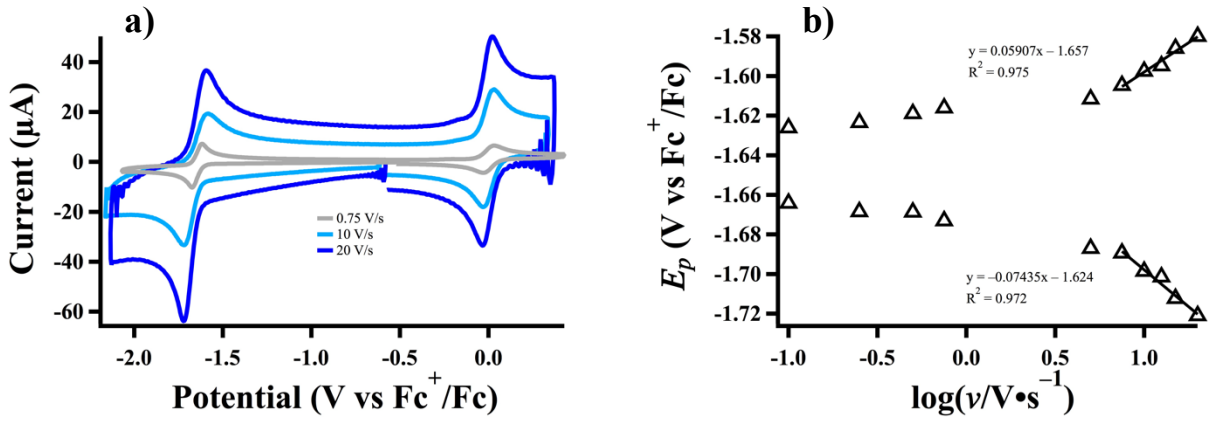

Figure 2.2. (a) Variable scan-rate CVs for $\mathbf{[Pt]^{2+}}$ (0.501 mM) in CH_3CN and (b) peak potentials plotted as a function of the logarithm of scan rate for calculation of electron transfer rate constant.

Analysis of the electron transfer rate constant with respect to the rate-determining step (RDS) in not inherently intuitive. Berben and co-workers have recently described selective, homogeneous electrocatalytic CO_2 reduction to HCO_2^- by an Fe cluster, $[Fe_4N(CO)_{12}]^-$, at a turnover frequency (TOF) of 210 1/s and a k_s of 0.005 cm/s.[7] Even at this slow of an electron transfer rate, the RDS for the relatively fast catalytic TOF was found to be hydride transfer to CO_2 and not electron transfer. In addition, Wiedner and Bullock have reported the kinetics for facile, H_2 production by a cobalt(II)-P_2N_2 electrocatalyst that has a k_s = 0.003 cm/s and they showed that even with a slow electron transfer rate, protonation of the reduced cobalt(I) species to generate the metal hydride was rate-limiting.[18] These comparisons allows us to conclude that the 2-electron reduction of $\mathbf{[Pt]^{2+}}$ to generate $\mathbf{[Pt]^0}$ is likely not rate-limiting.

Protonation of $\mathbf{[Pt]^0}$. As discussed in Chapter 1, it is believed that the electrochemically-generated $\mathbf{[Pt]^0}$ undergoes protonation to generate $\mathbf{[HPt]^+}$. CVs were shown that displayed attenuation of the return, anodic peak upon addition of acid to $\mathbf{[Pt]^{2+}}$ (Figure 1.4a). If the window for reduction is brought out to more negative values, a feature is observed at ca. –2.9 V vs

Fc^+/Fc, which is attributed to the reduction of **[HPt]**$^+$; this feature is only present with the addition of acid (Figure 2.3). To confirm this is due to generation of **[HPt]**$^+$, CVs of independently-isolated **[HPt]**$^+$ show the same irreversible feature (Figure 2.3, red trace). The irreversible nature is hypothesized to be due to the stronger hydride-donating ability of the reduced hydride that then transfer the hydride to a proton to make H_2. This further strengthens the claim that **[HPt]**$^+$ is being generated.

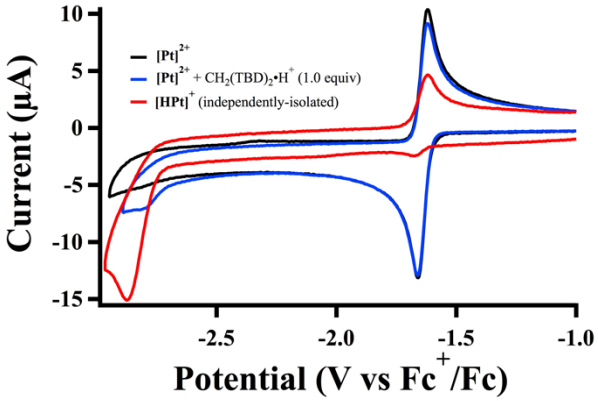

Figure 2.3. CVs of **[Pt]**$^{2+}$ and **[Pt]**$^{2+}$ in the presence of $CH_2(TBD)_2$•H^+ with CVs of independently-isolated **[HPt]**$^+$ for comparison. Scan rates are 0.250 V/s.

The rate constant for protonation of the reduced platinum species, **[Pt]**^{0}, was investigated using scan-rate dependent cyclic voltammetry. Specifically, for a chemical event that proceeds an electron-transfer event, or an EC mechanism, the peak potentials shift cathodically relative to the formal potential with increasing scan rate (eq 2.4).[19] All other constants are as previously defined. By plotting the change in peak potential as a function of the natural logarithm of the scan rate, the observed rate constant for protonation, $k_{obs,H+}$, was calculated from the y-intercept of the linear fit.

$$\frac{nF}{RT}\left(E_p - E^{\circ\prime}\right) = -0.780 + \frac{1}{2}\ln k_{obs,H+} + \frac{1}{2}\ln\frac{RT}{nF} - \frac{1}{2}\ln v \qquad (2.13)$$

The variable-scan-rate CVs for $\mathbf{[Pt]^{2+}}$ in the presence of 10 equiv of acid can be seen in Figure 2.4a. The cathodic peak potential shift to more negative values at higher scan rates, as expected (shown in Figure 2.4b). In addition, it is noted that at slower scan rates, the return oxidation wave is almost completely diminished due to consumption of $\mathbf{[Pt]^0}$. At faster scan rates, almost complete reversibility is observed due to the scan rate being much faster than the rate of protonation. From the y-intercept of linear plot in Figure 2.4b, the observed rate constant for protonation with 10 mM of $CH_2(TBD)_2{\bullet}H^+$, $k_{obs,10}$, was calculated to be 43 s^{-1}.

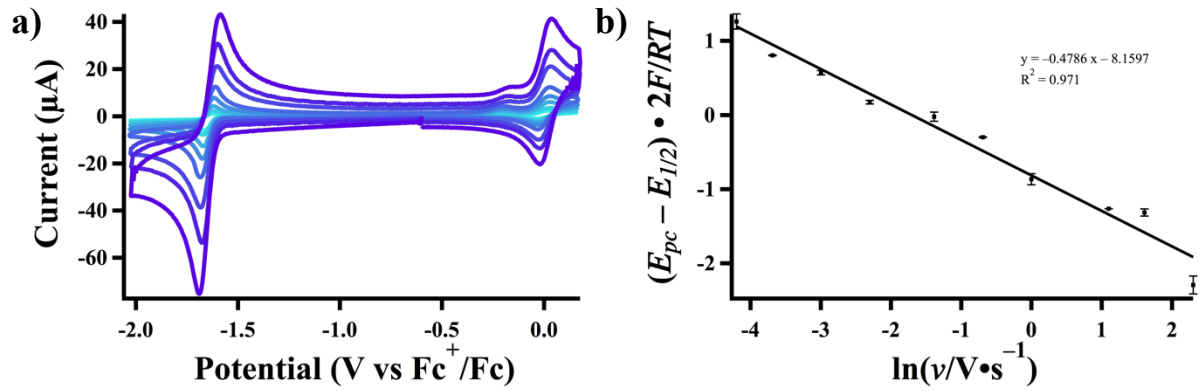

Figure 2.4. (a) Variable scan-rate CVs (0.05–10 V/s) of $\mathbf{[Pt]^{2+}}$ (1.06 mM) with $CH_2(TBD)_2{\bullet}H^+$ (9.62 mM) and (b) linear plot for the change in cathodic peak potential for calculating $k_{obs,H+}$.

The 2nd-order rate constant was determined by varying the concentration of acid. This confirmed that protonation is first order in acid, and gave an estimate of the rate constant under relevant, catalytic conditions. Figure 2.5 contains the scan-rate dependent CV data as well as the plots used to determine the observed rate constant for protonation of $\mathbf{[Pt]^0}$ with $CH_2(TBD)_2{\bullet}H^+$ (5.0 and 7.5 mM). The observed rate constants were calculated to be 53 and 75 s^{-1} for 7.5 and 10 mM $CH_2(TBD)_2{\bullet}H^+$, respectively, and from the slope of the line in Figure 2.6 the 2nd order rate constant is $8.1(7)\times10^3$ $M^{-1}s^{-1}$. These data indicate that protonation of $\mathbf{[Pt]^0}$ is facile and 1st order

in acid. Protonation is likely not the rate-determining step, otherwise we would expect a much large catalytic TOF observed under both CV and CPE conditions.

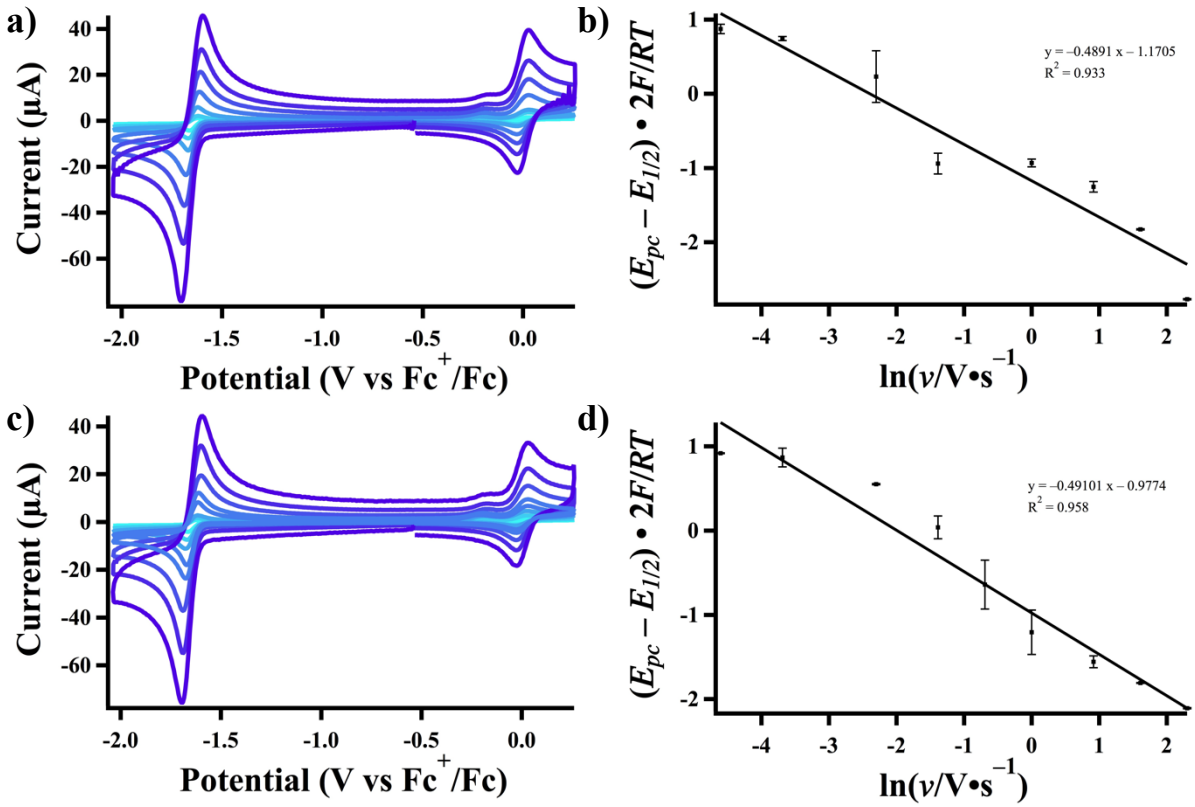

Figure 2.5. (a) Variable scan-rate CVs (0.025–10 V/s) of $[\mathbf{Pt}]^{2+}$ (1.06 mM) with $CH_2(TBD)_2{\bullet}H^+$ (5.00 mM) and (b) linear plot for the change in cathodic peak potential for calculating $k_{obs,H+}$. (c) and (d) are the same experiment, but with 7.47 mM $CH_2(TBD)_2{\bullet}H^+$.

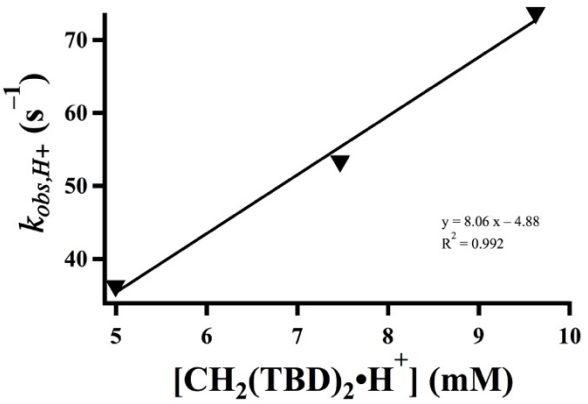

Figure 2.6. $k_{obs,H+}$ for protonation of **[Pt]^0** at various concentrations of $CH_2(TBD)_2$•H^+ to determine the 2nd order rate constant.

Hydride Transfer Step. The rate constant for hydride transfer from **[HPt]$^+$** to CO_2 was investigated by monitoring the amount of HCO_2^- produced by ^{1}H NMR spectroscopy over time. The amount of HCO_2^- at each time point was subtracted from the initial concentration of **[HPt]$^+$** to deduce the concentration **[HPt]$^+$** of at each time point. The rate constant, k_{obs}, was calculated by the method of initial rates by using the slope of the line containing the initial time points (t <15 min). The slope of the initial data points represents the rate equation:

$$-\frac{d[\mathbf{HPt^+}]}{dt} = -(slope) = k[\mathbf{HPt^+}][\mathbf{CO_2}] \tag{2.14}$$

Under the experimental conditions, it is assumed the concentration of CO_2 is 280 mM[20] and is therefore in 10-fold excess than **[HPt]$^+$** (21.9 mM) and the rate expression becomes:

$$-\frac{d[\mathbf{HPt^+}]}{dt} = -(slope) = k_{obs}[\mathbf{HPt^+}] \tag{2.15}$$

Thus, the observed rate constant, k_{obs}, is then calculated by dividing the negative of the slope by the concentration of **[HPt]$^+$**.

At room temperature, 40% of the initial **[HPt]**$^+$ was consumed after 100 min (Figure 2.7a) and the observed rate constant was calculated to be 2.8×10^{-4} s^{-1}. To determine more information about the nature of the transition state, the activation parameters were determined by calculating the rates at variable temperatures (Figure 2.7a). The observed rate constants for the reactions at 5 and –13 ºC were calculated to be 6.5×10^{-5} s^{-1} and 1.2×10^{-5} s^{-1}, respectively. As expected, these are significantly slower than the reactions at 25 ºC. From the Eyring plot (Figure 2.7b) the activation parameters were determined to be: $\Delta H^{\ddagger}$ = 12 kcal/mol, $\Delta S^{\ddagger}$ = –34 cal/mol•K, and $\Delta G^{\ddagger}_{298K}$ = 22 kcal/mol. As anticipated, the large $\Delta G^{\ddagger}_{298K}$ term suggests sluggish kinetics at room temperature. The entropic term suggests a large degree of order in the transition state and is consistent with a bimolecular reaction between two species; furthermore, it is in agreement with what few examples have been reported in the literature for activation parameters for hydride transfer to CO_2.[13-14]

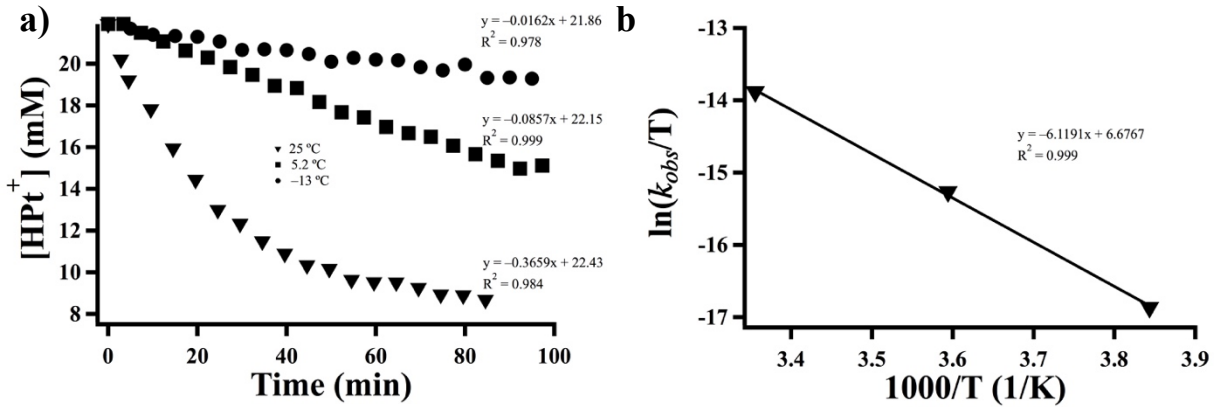

Figure 2.7. (a) Reaction of **[HPt]**$^+$ (21.9 mM) with CO_2 (1.0 atm) at various temperatures; linear fits from initial rates. (b) Eyring plot for hydride transfer to CO_2.

To date, intimate mechanistic details for the insertion of CO_2 into metal hydrides bonds are lacking and historically have been based primarily on computational studies.[21-28] Two of the most common mechanisms for CO_2 insertion can be seen in Scheme 2.1. In the so-called outer-

sphere mechanism, a hydride is delivered directly to CO_2 with concomitant cleavage of the M–H and C–H bond formation, resulting in a linear transition state. In the inner-sphere mechanism, M–H and CO_2 join in an end on fashion giving rising to a metallocyclic transition state. Recently, Mayer, Hazari, and colleagues have studied the kinetics of CO_2 insertion into, primarily d^9 and d^{10}, metal hydrides.[13-14,29] They have shown that the rate of CO_2 insertion can be accelerated, by up to a factor of $\times 10^3$, with the addition of Lewis acid (LA) cations.[13-14] The acceleration in rate has been attributed to stabilization of the negative charge that is built up on the carboxylate moiety in the transition state for the outer-sphere mechanism.

Scheme 2.1 Common Mechanisms for CO_2 Insertion into Metal Hydrides

(a) *Outer-sphere mechanism rate-determining step*

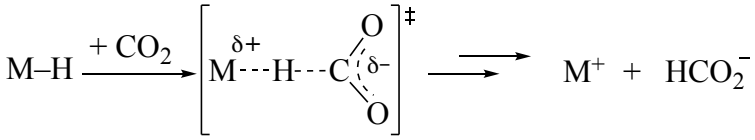

(b) *Inner-sphere mechanism rate-determining step*

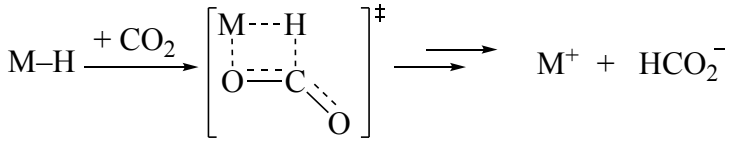

In an attempt to accelerate the rate of CO_2 insertion into **[HPt]**$^+$, lithium *bis*(trifluoromethane)sulfonimide, or $LiNTf_2$, was chosen as a LA due to its relatively high solubility in acetonitrile and it has previously been shown to result in the high rate acceleration.[13] For quantifying the rate in the presence of $LiNTf_2$, UV–Visible spectroscopy (UV–Vis) was utilized instead of ^{1}H NMR; this was due to precipitation of lithium formate at concentrations required for NMR (i.e. mM). The data for the reaction of **[HPt]**$^+$ and CO_2 with and without $LiNTf_2$ can be seen in Figure 2.8. From this data, as described previously, the observed rate constant for hydride transfer was calculated using the method of initial rates, as described prior, using the data points for $t < 20$ min. They were determined to be 6.5×10^{-5} s^{-1} without $LiNTf_2$

and 7.2×10^{-5} s^{-1} with $LiNTf_2$. It can be concluded that addition of $LiNTf_2$ does not seem to drastically increase the rate of CO_2 insertion into **[HPt]**$^+$.

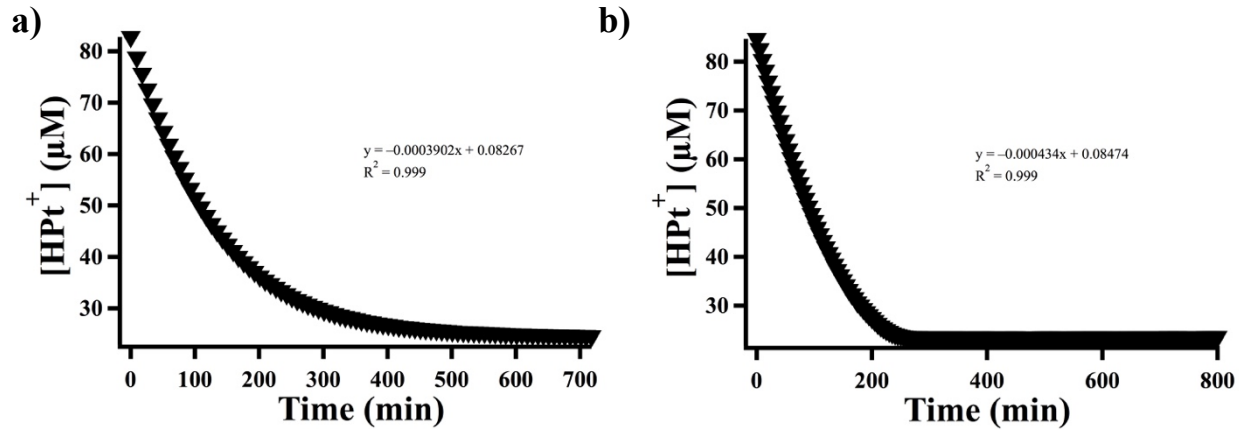

Figure 2.8. Reaction of **[HPt]**$^+$ (0.100 mM) with CO_2 (1.0 atm) without (a) and with $LiNTf_2$ (10 mM) (b). The inset shows the line for the initial rates calculated at t < 20min.

Considering alternative pathways. To provide more evidence in support of catalysis proceeding via a metal hydride intermediate, we sought to seek out alternative pathways for CO_2 reduction to HCO_2^-. Throughout our studies, we had observed that the reduced platinum species, **[Pt]**^{0}, can directly react with CO_2 (eq 2.7). The exact structure of the CO_2-bound species is uncertain, thus it is denoted ambiguously as "Pt–CO_2." Figure 2.9 shows the CVs for **[Pt]**$^{2+}$ with CO_2; once CO_2 is added, the return, anodic scan is completely diminished and the resulting wave is irreversible. This is attributed to reaction of CO_2 with **[Pt]**^{0}.

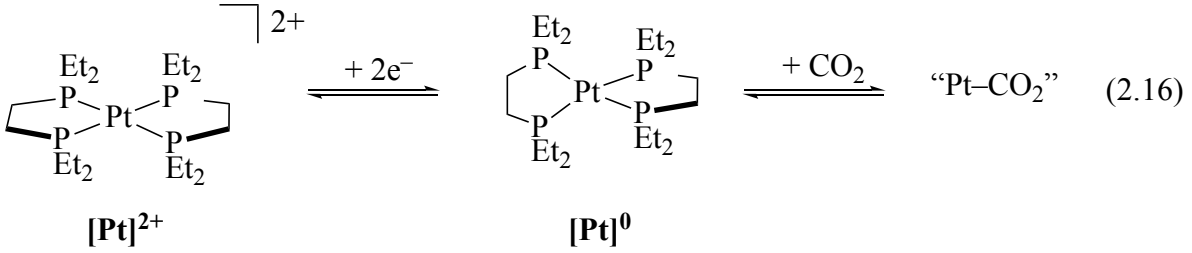

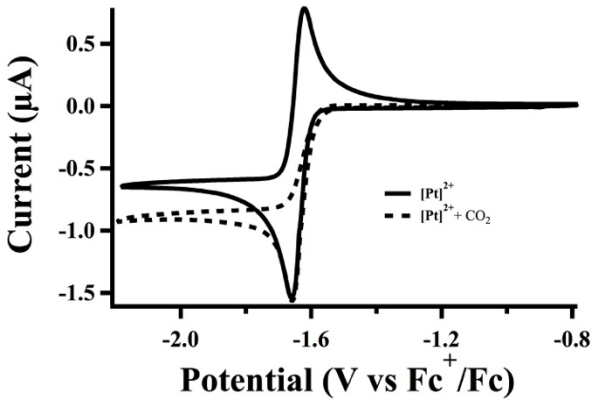

Figure 2.9. CVs of $\mathbf{[Pt]^{2+}}$ (1.0 mM) with and without CO_2 at a scan rate of 0.1 V/s.

The rate of CO_2 binding to $\mathbf{[Pt]^0}$ was then investigated to see how this rate compared to the rate of CO_2 insertion to $\mathbf{[HPt]^+}$. This was done by increasing the scan rate until the wave begins to have reversible character. In this method, described by DuBois, the peak ratio is proportional to the concentration of $\mathbf{[Pt]^0}$, and is plotted versus the time of the CV experiment to obtain an observed rate constant. [30] The plot of peak currents as a function of the scanning time can be seen in Figure 2.10. This plot is fit to a 3rd-order polynomial and from this the half-life was calculated to be 26 s, which corresponds to an observed rate constant, k_{obs}, of 0.023 s^{-1}.

To ensure more certainty in this number, the rate was also calculated another method described by Savéant.[15] In this method, the peak current ratio is plotted against the natural logarithm of the scan rate. The plot should exhibit a sigmoidal curve and is fitted with a polynomial to determine the half-life. Using this method, k_{obs} was calculated to be 0.027 s^{-1}. These numbers are in good agreement with one another, and the observed rate constant for CO_2 binding was calculated as an average of the two to be 0.025 s^{-1}. The rate for CO_2 binding by $\mathbf{[Pt]^0}$ is much less than the rate for protonation of $\mathbf{[Pt]^0}$ (>750 s^{-1} under catalytic conditions), thus this kinetic bifurcation point would favor protonation of $\mathbf{[Pt]^0}$ over CO_2 binding.

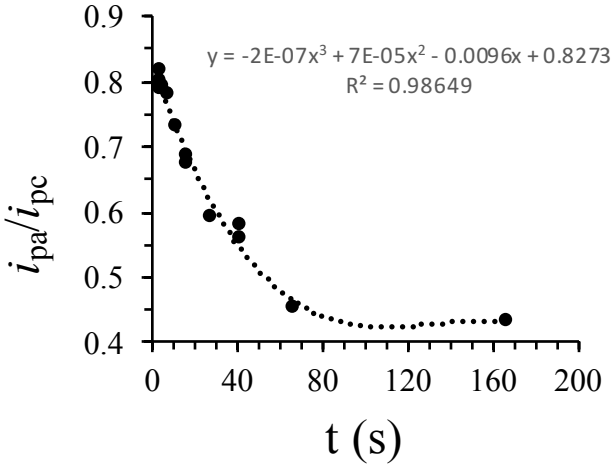

Figure 2.10. Determination of k_{obs} for CO_2 binding using the DuBois method. Peak ratios plotted at different scan rates for the reaction of $\mathbf{[Pt]^{2+}}$ (1.0 mM) and CO_2 (1.0 atm).

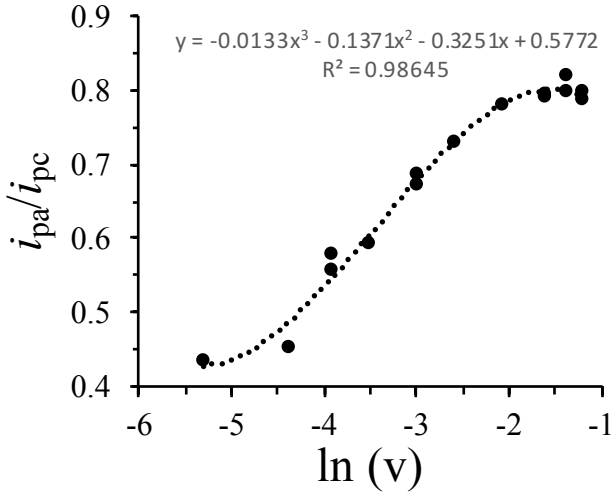

Figure 2.11. Determination of k_{obs} for CO_2 binding using Savéant method. Peak ratios plotted at different scan rates for the reaction of $\mathbf{[Pt]^{2+}}$ (1.0 mM) and CO_2 (1.0 atm).

Conclusion

Through a series of electrochemical, NMR, and UV–Vis experiments we have quantified the rates for each elementary step in the proposed catalytic cycle for CO_2 reduction to HCO_2^- by $\mathbf{[HPt]^+}$. It was demonstrated that electron transfer to $\mathbf{[Pt]^{2+}}$ and well as protonation of $\mathbf{[Pt]^0}$

(Steps 1 and 2 in Figure 2.12) were facile and likely not the rate-determining step in the proposed catalytic cycle. Furthermore, we have looked into potential side reactions and showed that the unproductive binding of CO_2 by **[Pt]^0** (Step 2' in Figure 2.12) is much slower ($\times 10^{-5}$) than protonation of **[Pt]^0**, thus formation of **[HPt]$^+$** is formed selectively under kinetic control. The overall rate of catalysis is hindered by slow hydride transfer step between **[HPt]$^+$** and CO_2, that might be going through an inner-sphere mechanism. Currently we are working on investigating methods of facilitating the hydride transfer as a means to develop fast catalysts for the reduction of CO_2 to HCO_2^-.

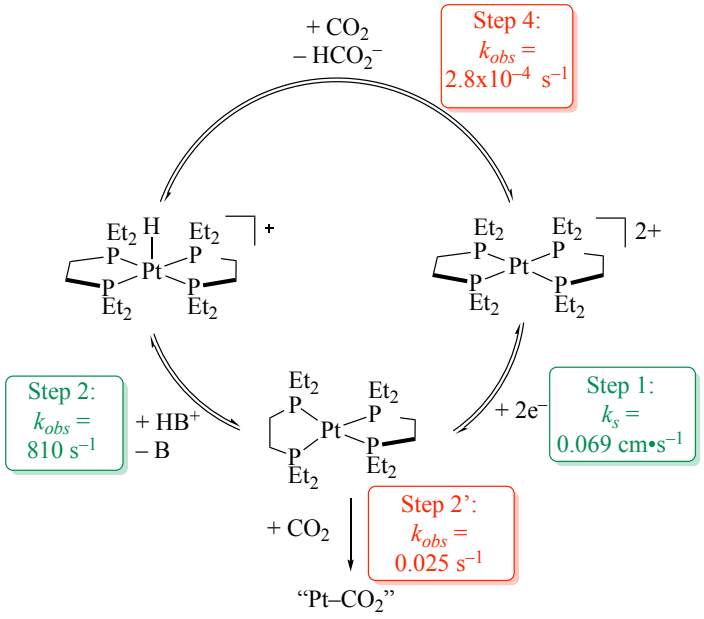

Figure 2.12. Proposed catalytic cycle and corresponding rates of reactions for CO_2 reduction to HCO_2^- by **[HPt]$^+$**

Experimental

All manipulations were carried out under a dinitrogen atmosphere in dried glassware unless otherwise noted. All chemicals were used as received from commercial sources unless otherwise noted. All non-deuterated solvents were degassed by sparging with argon and then dried by passage through an alumina column under argon pressure on a Solvent Drying System (JC Meyer Solvent Systems) and stored over activated molecular sieves. Deuterated solvents were degassed by freeze-pump-thaw methods then dried over activated molecular sieves. $[Pt(depe)_2][PF_6]_2$,[31] $[HPt(depe)_2][PF_6]$,[31] and $CH_2(TBD)_2$[32] were synthesized according to previously reported procedures.

Cyclic voltammetry. CVs were performed on a Pine Wavedriver 10 potentiostat with AfterMath software, using a 1 mm diameter glassy carbon disc working electrode and glassy carbon rod counter electrode. A Ag/Ag^+ pseudo-reference electrode containing a silver wire submerged in 0.2 M [*n*-Bu_4N][PF_6] separated from the bulk solution by a Vycor tip was used in addition to an internal ferrocene reference. It is important to note, that for kinetics experiments (especially at high scan rates) that the IR drop was compensated for and that ferrocene was added as an internal reference for experiments that required precise determination of peak potentials (for rate determination) and each CV was carefully referenced individually.

$CH_2(TBD)_2$•HPF_6. This synthesis was based on the modified literature report which synthesized the analogous compounds with Cl^- and BPh_4^- counter anions.[33] A solution of $CH_2(TBD)_2$ (123 mg, 0.425 mmol) in CH_3CN (5 mL) was added to $[NH_4][PF_6]$ and stirred for 2 h. The solution was then reduced in vacuo to yield a colorless, tacky solid. The tacky solid was dissolved in a minimal amount of toluene and placed in a freezer at –35 ºC; this yielded colorless crystals of $CH_2(TBD)_2$•HPF_6 (181 mg, 0.415 mmol, 98% yield) that were washed thrice with

ether and dried in vacuo. The ^{1}H NMR spectrum obtained was in agreement with previously reported data with the different counter anions.[33] ^{1}H NMR (d_6-dmso, 600 MHz): δ (ppm) = 13.40 (s br, 1H, N*H*), 4.77 (s, 2H, CH_2-bridging), 3.40 (t, 4H), 3.24 (t, 4H), 3.18 (m, 8H), 1.90 (quartet, 4H), 1.78 (quartet, 4H); ^{31}P{^{1}H} NMR (d_6-dmso, 243 MHz): δ (ppm) = –144 (m, PF_6).

Solution preparation for proton transfer rate constant. A stock solution of $[Pt(depe)_2][PF_6]_2$ was prepared by recording the mass of $[Pt(depe)_2][PF_6]_2$ (23.7 mg, 0.0264 mmol) directly in a 25.00 mL volumetric flask and dissolving with $CH_3CN/TBAPF_6$ (0.2 M). The working solution for CV measurements was then prepared by weighing $CH_2(TBD)_2{\bullet}H^+$ (21.0 mg, 0.481 mmol) directly into a 5.00 mL volumetric flask and dissolving with the $[Pt(depe)_2][PF_6]_2$ stock solution that was previously prepared. The resulting solution was 1.06 mM in **[Pt]**$^{2+}$ and 9.62 mM in $CH_2(TBD)_2{\bullet}H^+$. This was repeated for different concentrations of $CH_2(TBD)_2{\bullet}H^+$ by weighing out differing amounts and dissolving in the same **[Pt]**$^{2+}$ stock solution. CVs were then recorded with an aliquot of this solution. The data points in Figures 2.4 and 2.5 are an average of 3 data points for each scan rate and errors are reported to one standard deviation.

Solution preparation for electron transfer rate constant. A 153 mM of $[Pt(depe)_2][PF_6]$ stock solution in CH_3CN (16.4 μL) was added to a 5.00 mL volumetric flask along with a 103 mM ferrocene stock solution in CH_3CN (21.3 μL) and diluted with $CH_3CN/TBAPF_6$ (0.2 M). The resulting solution was 0.501 mM in **[HPt]**$^{+}$ and 0.499 mM in ferrocene. CVs were then recorded with an aliquot of this solution. The data points in Figures 2.1 and 2.2 are an average of 3 data points for each scan rate and errors are reported to one standard deviation.

CO_2 insertion rates by NMR. $[HPt(depe)_2][PF_6]$ (82.5 mg, 0.109 mmol) was weighed directly into a 5.00 mL volumetric flask. A small amount of CD_3CN (ca. 2 mL) was added to dissolve the platinum. C_6H_6 (9.00 μL) was added as an internal standard and the remaining CD_3CN was added. The resulting solution was 21.9 mM in **$[HPt]^+$** and 26.4 mM in C_6H_6 and stored in the glovebox freezer at –35 ºC in between experiments. A 0.60 mL aliquot was put into a J-Young tube and an NMR spectra were acquired before the addition of CO_2. CO_2 was added by first pseudo-freeze-pump-thawing the J-Young tube on a custom-made gas-addition manifold composed of Swagelok pieces. To do this, a J-Young tube is attached to the manifold and the manifold is evacuated under dynamic vacuum and then shut off to vacuum once the pressure is < 50 mTorr. The J-Young tube is then briefly turned to open the valve to the static vacuum above it and then immediately closed. Dynamic vacuum is then once again applied to the manifold and the pressure increase on the gauge is noted. This procedure is then repeated until the solution is fully degassed, as indicated by a lack of pressure increase when applying dynamic vacuum after a cycle (usually three times would suffice). Once degassed, and after evacuating the manifold, it is then charged with CO_2 (1.0 atm). Immediately after charging with CO_2, a timer is started and this corresponds to $t = 0$. The J-Young tube is then quickly brought to and inserted into the pre-equilibrated spectrometer probe. For low temperature experiments, the procedure is the same except that the J-Young is first equilibrated in a cooling bath (water/ice for 5 ºC measurements and 9:1 ethanol/ethylene glycol –13 ºC measurements) for several hours until the temperature comes to a constant reading. The NMR probe is set to the temperature of the cooling bath and allowed to equilibrate for at least 15 minutes. NMR spectra are acquired before gas addition. Gas is then added as described above and NMR spectra are acquired over time. After acquiring the necessary spectra, a CH_3OH standard is used to calibrate the actual probe temperature.[34]

CO_2 insertion rates by UV–Vis. These experiments were conducted in an identical fashion to the rates for NMR described above, except they were in a 1.0 cm path length quartz cuvette that had been adapted for connecting to the gas-addition manifold and at lowered concentrations achieved by serial dilution with volumetric glassware.

References

1. Gray, H. B. *Nature Chemistry* **2009**, *1*, 7-7.

2. Lewis, N. S. *Science* **2007**, *315*, 798-801.

3. Lewis, N. S.; Nocera, D. G. *Proc. Natl. Acad. Sci.* **2006**, *103*, 15729-15735.

4. Ceballos, B. M.; Yang, J. Y. *Proc. Natl. Acad. Sci.* **2018**, *115*, 12686-12691.

5. Taheri, A.; Berben, L. A. *Inorg. Chem.* **2016**, *55*, 378-385.

6. Barlow, J. M.; Yang, J. Y. *ACS Cent. Sci.* **2019**, *5*, 580-588.

7. Taheri, A.; Carr, C. R.; Berben, L. A. *ACS Catal.* **2018**, *8*, 5787-5793.

8. Taheri, A.; Thompson, E. J.; Fettinger, J. C.; Berben, L. A. *ACS Catal.* **2015**, *5*, 7140-7151.

9. Kang, P.; Cheng, C.; Chen, Z.; Schauer, C. K.; Meyer, T. J.; Brookhart, M. *J. Am. Chem. Soc.* **2012**, *134*, 5500-5503.

10. Kang, P.; Meyer, T. J.; Brookhart, M. *Chem. Sci.* **2013**, *4*, 3497-3502.

11. Ahn, S. T.; Bielinski, E. A.; Lane, E. M.; Chen, Y.; Bernskoetter, W. H.; Hazari, N.; Palmore, G. T. R. *Chem. Commun.* **2015**, *51*, 5947-5950.

12. Roy, S.; Sharma, B.; Pécaut, J.; Simon, P.; Fontecave, M.; Tran, P. D.; Derat, E.; Artero, V. *J. Am. Chem. Soc.* **2017**, *139*, 3685-3696.

13. Heimann, J. E.; Bernskoetter, W. H.; Hazari, N. *J. Am. Chem. Soc.* **2019**, *141*, 10520-10529.

14. Heimann, J. E.; Bernskoetter, W. H.; Hazari, N.; Mayer, James M. *Chem. Sci.* **2018**, *9*, 6629-6638.

15. Savéant, J. M. In *Investigation of Rates and Mechanisms of Reactions* Wiley, Ed. 1986.

16. Bard, A. J. *Electrochemical methods : fundamentals and applications / Allen J. Bard, Larry R. Faulkner*; Wiley: New York, 1980.

17. Mashkina, E.; Bond, A. M. *Anal. Chem.* **2011**, *83*, 1791-1799.

18. Wiedner, E. S.; Bullock, R. M. *J. Am. Chem. Soc.* **2016**, *138*, 8309-8318.

19. Saveánt, J. M. *Elements of Molecular and Biomolecular Electrochemistry: An Electrochemical Approach to Electron Transfer Chemistry*; Wiley: Hoboken, NJ, 2006.

20. Fujita, E.; Szalda, D. J.; Creutz, C.; Sutin, N. *J. Am. Chem. Soc.* **1988**, *110*, 4870-4871.

21. Bernskoetter, W. H.; Hazari, N. *Eur. J. Inorg. Chem.* **2013**, *2013*, 4032-4041.

22. Huang, F.; Zhang, C.; Jiang, J.; Wang, Z.-X.; Guan, H. *Inorg. Chem.* **2011**, *50*, 3816-3825.

23. Ma, Q.-Q.; Liu, T.; Adhikary, A.; Zhang, J.; Krause, J. A.; Guan, H. *Organometallics* **2016**, *35*, 4077-4082.

24. Osadchuk, I.; Tamm, T.; Ahlquist, M. S. G. *Organometallics* **2015**, *34*, 4932-4940.

25. Ríos, P.; Rodríguez, A.; López-Serrano, J. *ACS Catal.* **2016**, *6*, 5715-5723.

26. Schmeier, T. J.; Dobereiner, G. E.; Crabtree, R. H.; Hazari, N. *J. Am. Chem. Soc.* **2011**, *133*, 9274-9277.

27. Schmeier, T. J.; Hazari, N.; Incarvito, C. D.; Raskatov, J. A. *Chem. Commun.* **2011**, *47*, 1824-1826.

28. Suh, H.-W.; Schmeier, T. J.; Hazari, N.; Kemp, R. A.; Takase, M. K. *Organometallics* **2012**, *31*, 8225-8236.

29. Hazari, N.; Heimann, J. E. *Inorg. Chem.* **2017**, *56*, 13655-13678.

30. Yang, J. Y.; Bullock, R. M.; Shaw, W. J.; Twamley, B.; Fraze, K.; DuBois, M. R.; DuBois, D. L. *J. Am. Chem. Soc.* **2009**, *131*, 5935-5945.

31. Miedaner, A.; DuBois, D. L.; Curtis, C. J.; Haltiwanger, R. C. *Organometallics* **1993**, *12*, 299-303.

32. Oakley, S. H.; Coles, M. P.; Hitchcock, P. B. *Inorg. Chem.* **2003**, *42*, 3154-3156.

33. Coles, M. P.; Aragón-Sáez, P. J.; Oakley, S. H.; Hitchcock, P. B.; Davidson, M. G.; Maksić, Z. B.; Vianello, R.; Leito, I.; Kaljurand, I.; Apperley, D. C. *J. Am. Chem. Soc.* **2009**, *131*, 16858-16868.

34. UCI NMR Manual; https://www.chem.uci.edu/~dennison/UCINMRmanual.pdf.

CHAPTER 3:

Role of LiCl in Generating Soluble Organozinc Reagents

Introduction*

Organometallic reagents have revolutionized organic synthesis by enabling diverse carbon–carbon bond forming reactions. The generation of soluble organomagnesium reagents (Grignard reagents) by oxidative addition of organohalides to magnesium turnings was an enabling early advance.[1,2] The analogous direct insertion of organohalides into commercially available powders of other metals would provide the simplest route for the synthesis of valuable reagents with higher functional group tolerance, complimentary reactivity, or catalytic activity (e.g., organo-zinc, -copper, -calcium, -manganese, -indium, -aluminum, and -palladium complexes). Yet generalization of this direct insertion process has long been hampered by the resistance of commercial powders of metals other than magnesium toward direct insertion of organohalides. The primary failure methods are believed to be recalcitrant oxidative addition to these metal surfaces due to passivation from surface impurities[3] or inherent inactivity,[4] and/or low solubility of the products once formed, which are then sluggish to dissociate from the metallic surface.[5]

Given the challenges with in operando characterization of small quantities of intermediates in mixtures of metal powders with organohalides, progress in extending direct insertion to other metals has been largely empirical to date. For example, in 2006 Knochel established that addition of lithium chloride enabled the synthesis of highly functionalized, soluble organozinc reagents via oxidative addition to metallic zinc (Scheme 3.1).[6] The reagents

* This chapter has been published: Feng, C.; Cunningham, D.W.; Easter, Q.T.; Blum, S.A. *J. Am. Chem. Soc.* **2016**, *138*, 11156–11159

produced through this pathway (denoted as RZnI•LiCl) are synthetically useful.[7–9] In a subsequent series of discoveries by Knochel, addition of lithium chloride enabled the direct insertion of organohalides into manganese,[10] aluminum,[11] and indium[12] powders, often in conjunction with other additives such as TMSCl[6,11] or metal halide catalysts[10].

Scheme 3.1. Prior work and experiment schematic

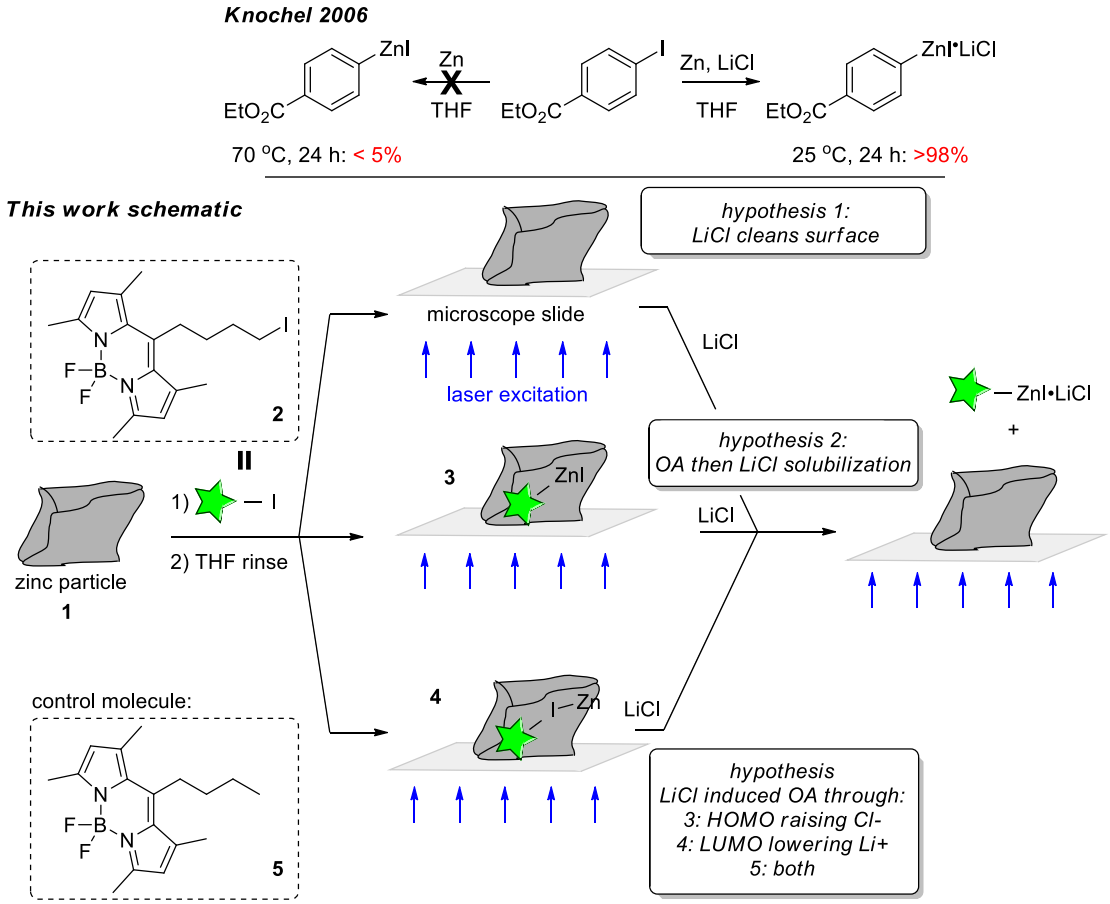

Despite its widespread use, the mechanistic role of lithium chloride in generating these reagents remains speculative and has not been experimentally established. We herein describe fluorescence microcopy experiments with single molecule[13–27] sensitivity that rule out some mechanistic possibilities and rationalize why the synthetic system optimized to LiCl rather than a different salt. It is anticipated that this improved understanding of the mechanistic basis for the

effect will facilitate the future development of currently unknown organometallic reagents by direct insertion into presently recalcitrant metals.

Five mechanistic possibilities were considered herein for the role of lithium chloride in the formation of soluble organozinc reagents from alkyl iodides and zinc powder: 1) lithium chloride cleans impurities from the surface of the zinc powder before coordination or reaction of the alkyl iodide, 2) lithium chloride solubilizes surface organozinc reagents after oxidative addition; 3) lithium chloride accelerates oxidative addition, through binding of lithium cation to iodide (LUMO lowering); 4) or through binding of chloride to zinc surface (HOMO raising); 5) simultaneous LUMO lowering/HOMO with both lithium and chloride (Scheme 1).

Results and Discussion

We designed an alkyl iodide probe (**2**) to differentiate between these mechanistic roles through fluorescence microscopy imaging (Scheme 3.1). The green BODIPY fluorophore in **2** serves as a bright "beacon" that enables determination of the location of the alkyl group throughout the multiple physical phase changes and chemical changes of the overall reaction. The fluorophore is a spectator in the reaction and is not directly attached to the iodide in order to reduce the chance of quenching or other undesired/interfering reactivity of the fluorophore upon reaction with the zinc surface.

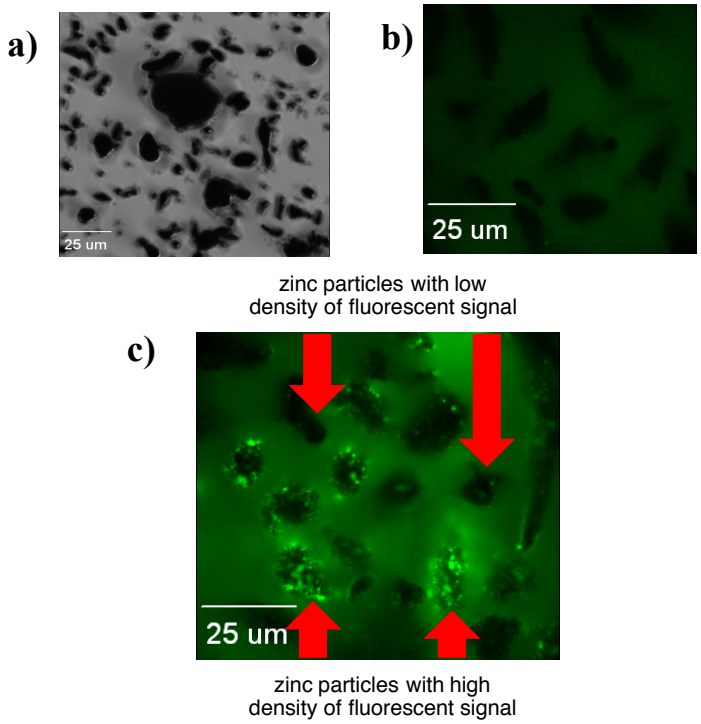

Figure 3.1. a) Zinc powder under ambient light illumination. b) Zinc powder after soaking in a solution of control compound **5**. Individual particles are dark against the light green background produced by the solution, showing the absence of attachment of **5** to the surface of the zinc. c) Zinc powder after soaking in a solution of **2**. Particles show bright green spots corresponding to coating with the fluorophore probe; degree of coating is heterogeneous between particles. The image in a) was acquired by Chao Feng.

Commercial zinc metal powder (**1**, Figure 3.1a) from the same supplier and of the same mesh as previously employed by Knochel was treated with TMSCl per the reported protocol[6] and then soaked in a solution of probe alkyl iodide **2** in THF for 24 h. The mother liquor containing residual **2** was then decanted, and the remaining zinc particles were rinsed three times with THF. The zinc particles were suspended in clean THF and transferred to a reaction vial with a thin glass bottom suitable for fluorescence microscopy imaging of the sample under air-free conditions.

Organic molecules or groups of many molecules containing the fluorophore are clearly visible as bright green spots on the surface of the dark irregular zinc particles (Figure 3.1b). These coat the 3D surfaces of the particles as can be observed by changing the microscope focus up and down the *z* axis to trace the 3D contours of the particles. The background appears light green rather than black because of illumination from fluorescent spots on out-of-focus nearby zinc particles and residual fluorescent material in solution, in combination with the extremely high sensitivity of the camera to detect low levels of fluorescence. On the basis of the fluorescence intensity and photophysical behavior of these spots on the zinc particles, it is possible to clearly assign the brightest spots as many molecules of probe (e.g., >~1000) and not single molecules.[29]

Control probe **5** is similar to **2** but lacks the carbon–iodide bond. Zinc particles prepared identically except with control probe **5** instead of **2** are dark in comparison and do not show similar high quantities of organic molecules on their surface (Figure 3.1c). This experiment indicated the chemoselectivity of the surface attachment process and is consistent with the assignment of the chemical structure of the fluorescent molecules on the surface as **3** or **4**, rather than nonspecifically physisorbed material. The presence of these organic groups on the surface of the zinc *prior* to addition of lithium chloride is inconsistent with hypothesis 1.

The next question was if this observable material constituted reaction intermediates in the synthesis of organozinc reagents. In order to examine this question and remaining hypotheses 2–5, four different solid salts were then added to four separate samples of zinc particles previously treated with alkyl iodide probe **2**: LiCl, LiOTf, NaCl (only sparingly soluble, control experiment), and Bu_4NCl (Figure 3).

At t = 600 s after salt addition, the imaging region was moved to a new area that had not been exposed to the laser, in order to prevent any laser-induced effects from convoluting the data analysis. The sample with lithium chloride showed a dramatic decrease in the quantity of probe on the surface of the zinc, as seen by the lack of bright spots at t = 600 s, consistent with assignment of this material as reaction intermediates that could be transformed by lithium chloride.

In contrast, at t = 600 s, organic probe remained on the surface of the zinc in all other samples after addition of the LiOTf (lithium cation but no chloride), NaCl (insoluble control), and Bu_4NCl (chloride anion but no lithium cation), as seen by the presence of similar numbers and intensities of bright spots at t = –10 and t = 600 s. Representative data from one run is shown in Figure 3.2; data from triplicate runs are included in the SI. These results established that that both lithium and chloride are required concomitantly for transformation of the organic surface material. These results provide a mechanistic rationale for why the synthetic reaction optimized to LiCl: other salts are less effective at transforming surface-bound intermediates. These results eliminate hypotheses 3 and 4 from Scheme 3.1.

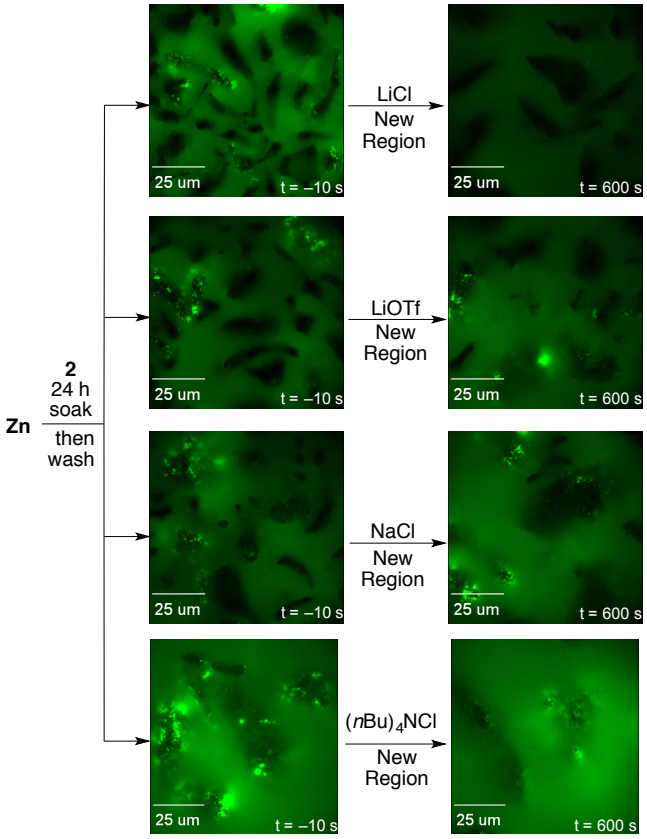

Figure 3.2. The addition of solid salts to different aliquots of a Zn sample in THF, LiCl, LiOTf, NaCl, n-Bu_4NCl (top to bottom). Negative times indicate the time before addition of the salt.

Quenching Control Experiments. An alternative explanation for the decrease in the fluorescence of the sample is that the added lithium chloride or liberated byproducts zinc iodide or zinc chloride could quench the fluorescence of the fluorophore, leading to a decrease in fluorescence signal even though the fluorescently tagged alkyl or alkyl iodide were still present on the surface of the zinc. Three control experiments therefore quantified the bulk fluorescence of a sample of BODIPY fluorophore **2** in THF in the absence of lithium chloride and in a saturated solution of lithium chloride, and separately at several concentrations of zinc iodide and zinc chloride. The three samples displayed identical fluorescence at multiple concentrations (Figure 3.3). Thus, the disappearance of the fluorescence signal is attributed to removal of the

organic probe from the surface and not to quenching from the lithium chloride or from potential byproducts.

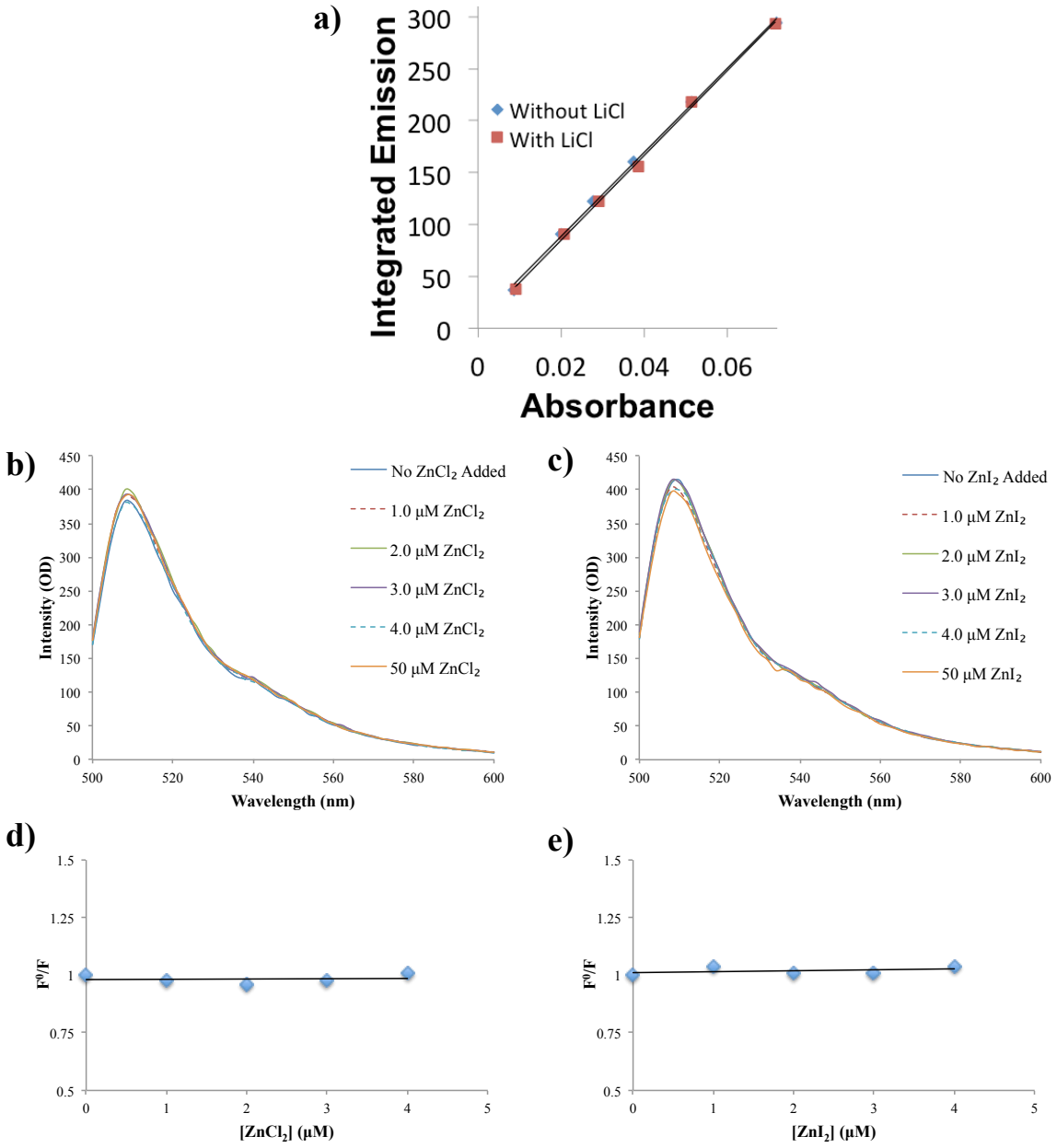

Figure 3.3. Fluorescence of a sample of **2** is not affected by reagents or byproduct quenching. a) In presence and absence of saturated lithium chloride, at varying concentrations of **2**. b–e) At fixed concentrations of **2** and varying concentrations of ZnI_2 or $ZnCl_2$ as would be expected in a microscopy sample; $\lambda_{ex} = 488$ nm and fluorescence was monitored at 510 nm. The data and graph in a) was collected and produced by Chao Feng.

Characterization of the Surface through Downstream Reactivity. We considered ways to differentiate between surface intermediates **3** and **4**. In contrast to the high signal that makes fluorescence imaging of small number of molecules possible, in our hands, surface Raman spectroscopy was insufficiently sensitive to differentiate between these two options by characterizing the type of bonds present on the surface. We therefore turned to chemical methods to characterize the nature of the surface. Specifically, to a sample of the zinc particles treated with **2** was added three drops of water during microscopy imaging. This addition resulted in complete and immediate removal of the plausible intermediates on the surface (Figure 3.4).

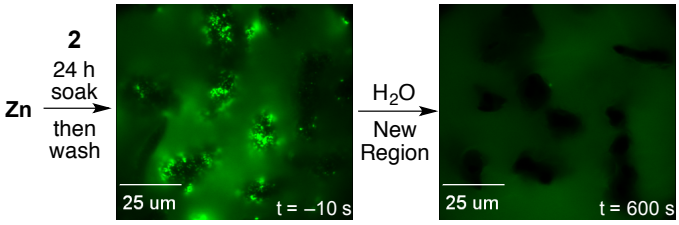

Figure 3.4. The addition of water to a zinc sample in THF, showing water-induced removal of the probe from the surface.

Zinc metal is reported to be unreactive with water at neutral pH and ambient temperature; thus, this effect is most consistent with protonation of a zinc–carbon bond by water to release **6** from the surface of the zinc (hypothesis 2). Nevertheless, it cannot be ruled out that a few layers of surface zinc react with the water even at this ambient temperature, resulting in chemical exfoliation of the top zinc layers, which would concurrently remove the probe. Thus, hypothesis 5 remains viable.

Characterization of Ultimate Organic Product. Treatment of probe **2** with the same zinc powder and lithium chloride in a standard bench experiment with wet d_8-THF led to the expected protodemetallated product **6**, as confirmed by ^{1}H NMR spectroscopic comparison with an authentic sample of **6** that was independently prepared and fully characterized (eq 3.1).

Protodemetallation is also the protocol employed by Knochel to characterize the organozinc compounds synthesized through this method. This result established that probe **2** does indeed form the corresponding organozinc reagent **7** upon treatment with zinc metal and lithium chloride in THF in our studied system.

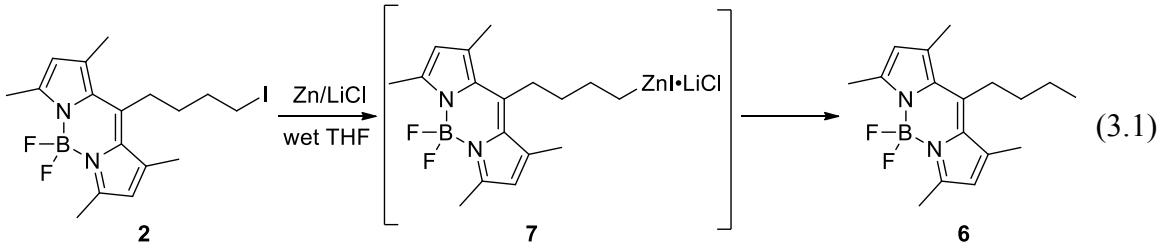

(3.1)

Conclusion

In conclusion, we demonstrated a sensitive new tool for investigating the roles of additives in the synthesis of organo- metallic reagents through direct metal insertion. This disclosure is the first example of fluorescence microscopy already well established in biology as a tool to determine the mechanistic role of a reagent in organic/organometallic synthesis. This sensitivity permitted detection of surface intermediates for the first time in reactions of commercial zinc powder with organohalides.

An initial reaction between the zinc surface and an alkyl iodide occurred in the absence of LiCl, inconsistent with hypothesis 1 (data in Figure 1b). An aryl iodide did not generate surface intermediates, inconsistent with hypotheses 3−5 (data in Scheme 3.1). Both lithium and chloride were required to transform the surface species, further ruling out hypotheses 3 and 4 (data in Figure 2). Not all locations on the surface of zinc were equally reactive, and addition of LiCl removed the organic material from these most reactive locations on the zinc surface, thus plausibly re-exposing the more reactive zinc locations to further substrate direct insertion during

the synthetic procedure, consistent with hypothesis 2. The mechanistic role for the lithium chloride additive is thus indicated as the solubilization of otherwise persistent organometallic intermediates from the surface of the zinc. These studies bring mechanistic understanding to an area of chemistry that is currently progressing empirically.

Experimental

All manipulations were carried out under a nitrogen atmosphere in dried glassware unless otherwise noted. All chemicals were used as received from commercial sources unless otherwise noted. THF was dried by passage through an alumina column under argon pressure on a Seca Solvent System (Glass Contour). Zinc powder (99.9%) was purchased from Strem and dried in vacuo while applying heat from a heat gun for ca. 30 min. Trimethylsilyl chloride was purified by stirring over CaH_2 for 24 h and was then vacuum transferred. Tetra-*n*-butylammonium chloride was purified by recrystallization from acetone/ether and dried in vacuo. 3,4-Dichlorobenzaldehyde was purified by recrystallization from ethanol. Zinc(II) iodide (>98%) was purchased from Sigma Aldrich and used directly from the bottle. Zinc(II) chloride was purchased from Fischer and purified by refluxing in dioxane over zinc dust, the solution was filtered hot and resulted in precipitation the zinc(II) chloride, which was then recrystallized from dioxane. Chlorodiphenylphosphine was purchased from Sigma Aldrich and distilled under reduced pressure. Trimethyltin chloride was purchased from Acros and used directly from the bottle. Flash chromatography was conducted using a Teledyne Isco Combiflash Rf 200 Automated Flash Chromatography System.

Fluorescent probe 2 was synthesized from the corresponding alkyl bromide[13] via a Finkelstein reaction. In the atmosphere, a round-bottom flask was charged with sodium iodide (0.245 g, 1.63 mmol, 3.0 equiv), acetone (3.0 mL), followed by **SI-1** (0.209 g, 0.546 mmol, 1.00

equiv). After heating at reflux for 8 h, the reaction mixture was evaporated to dryness. The residue that remained was dissolved in DCM (ca. 10 mL), extracted with brine then water (ca. 5 mL each), and dried over sodium sulfate. The mixture was filtered to removed sodium sulfate and then concentrated in vacuo to yield a crude product which was then chromatographed with 25% DCM in hexanes as the eluent. Removal of volatiles at ca. 10 mTorr for 6 h afforded **2** as an orange solid (0.20 g, 84% yield). ^{1}H NMR ($CDCl_3$, 600 MHz) δ 6.06 (s, 2H), 3.22 (t, J = 6.8 Hz, 2H), 2.98 (t, J = 8.5 Hz, 2H), 2.51 (s, 6H), 2.43 (s, 6H), 2.03 (quin, J = 7.2 Hz, 3H). ^{13}C NMR ($CDCl_3$, 125 MHz) δ 154.1, 145.3, 140.3, 131.4, 121.8, 34.0, 32.6, 27.5, 16.6, 14.5, 5.4. HRMS (ESI): m/z calculated for $C_{17}H_{22}BF_2IN_2Na$ ($[M+Na]^+$), 453.0786; found, 453.0792.

Control Probe 5 was prepared according to a literature procedure.[13] ^{1}H NMR ($CDCl_3$, 600 MHz) δ 6.05 (s, 2H), 2.94 (t, J = 8.6 Hz, 2H), 2.51 (s, 6H), 2.43 (s, 6H), 1.63 (m, 2H), 1.53 (m, 2H), 0.99 (m, 3H). This spectrum is in agreement with previously reported spectral data.

Microscopy and Image Acquisition. Imaging was performed with an IX71 inverted microscope (Olympus Corporation) and an oil-immersion objective with a 1.49 numerical aperture. Samples were illuminated with the 488 nm line of an Ar/Kr ion laser (Coherent Inc.) set to 25 mW. Illumination was done under conditions of EPI. Samples were imaged with a C9100-13 electron multiplier CCD camera (Hamamatsu Photonics). The CCD chip was a back-thinned electron multiplication type with an effective 512 × 512 array of pixels.

Coverslip Preparation. Glass coverslips (25 × 25 mm, No. 1.5, VWR Scientific) with a thickness of 0.17 mm were used for imaging. Cleaning of the coverslips was done by soaking them in a polypropylene Coplin staining jar (VWR Scientific) with a 0.5% (v:v) solution of Hellmanex Detergent (Fisher Scientific) in MilliQ water for 24 h, then sonicating them in the

same solution for 30 min. The coverslips were then rinsed three times, first with MilliQ water, then spectroscopic grade ethanol; finally, they were dried with a heat gun.

Construction of Reaction Cells. Reaction cells were constructed from a 1 dram vial by cutting of the bottom of the vials and adhering it to the prepared glass coverslip with Devcon 5 Minute Epoxy. After allowing the epoxy to cure for 1 h, the reaction cells were then dried under dynamic vacuum for 12 h before being brought into the glovebox.

Construction of Salt Pocket. The salt pocket allowed for the addition of solids to the imaging cell without compromising the atmosphere. The pocket was made by heating the tapered section of a Pasteur pipette with a blowtorch. Once the glass was molten (and had the consistency of cooked spaghetti) the delivering end of the pipette was then slowly pulled away from the base of the pipette while gently twisted. To fit inside the reaction cell, the open end of the pipette was scored and removed by holding firmly and applying pressure with your thumbs. NOTE: It is important that the pocket is as long as possible, yet still able to fit inside the 1 dram imaging cell. Otherwise it has been noticed to lead to contamination of the sample as a result of the surface adhesion of THF, which allows for THF to travel up the side of the glass and into the pocket.

Addition of Solid LiCl, LiOTf, and NaCl Experiments. In order to directly compare all three salt additions to each other, one batch of zinc particles was prepared and partitioned into three aliquots (one for each salt). The addition of the three salts to the zinc particles were reproduced in triplicate and to limit variation between batches they were all done on the same day.

In a glovebox filled with nitrogen, a 1 dram vial was charged with zinc (75 mg, 1.1 mmol), THF (1.0 mL), and trimethylsilyl chloride (1 drop). The mixture was then capped and

agitated gently to mix the solution. After soaking at room temperature for 2 h, the supernatant was removed from the mixture and the resulting zinc particles were washed with THF (2 × 2 mL). After the second rinse a solution of **2** (2.0 mM of **2** dissolved in THF, 20 drops) was added to the zinc particles, the solution was capped, and the vial was swirled gently to mix the solution, and set aside for soaking. After soaking at room temperature for 24 h, the supernatant was removed from the mixture and the resulting zinc particles were washed with THF (3 × 2 mL). After the third rinse THF (3.0 mL) was added to the vial, the vial was swirled vigorously to suspend the zinc particles in solution, and the resulting slurry was partitioned into three aliquots containing THF and zinc, and then put into separate reaction cells. To each cell was added one of the homemade salt containing pockets. The amounts of each salt were: lithium chloride (8.5 mg, 0.20 mmol), lithium triflate (31 mg, 0.20 mmol), and sodium chloride (12 mg, 0.20 mmol). The cells were then capped and carefully removed from the glovebox for imaging.

The cells were imaged for 11 min each. Zinc particles with fluorescent signals were found and kept in focus. After imaging the reaction cell for 40 s and observing the surface bound intermediate, the salt was added by inverting the cell and gently shaking the cell, this was repeated three times. After putting the cell back onto the microscope, zinc particles were found and brought into focus at 100 s after the salt addition and these particles were kept in focus until 540 s after the addition, after which the stage was moved to find new zinc particles that had not yet been exposed to laser illumination. Data from the triplicate runs can be seen in Figure 3.5.

Addition of Solid (*n*-Bu)$_4$NCl and LiCl Experiments. After the addition of the three salts, we sought out tetra-*n*-butylammonium chloride (TBAC) as a more soluble chloride source than the previously used sodium chloride. It was only necessary to compare the measurements from the TBAC to those of lithium chloride, so we partitioned the prepared zinc particles into

only two aliquots. To limit variations between batches this procedure was ran in triplicate on the same day. This procedure is analogous to that above, but with different amounts of zinc particles.

In a glovebox filled with nitrogen, a 1 dram vial was charged with zinc (50 mg, 0.76 mmol), THF (1.0 mL), and trimethylsilyl chloride (1 drop). The mixture was then capped and agitated gently to mix the solution. After soaking at room temperature for 2 h, the supernatant was removed from the mixture and the resulting zinc particles were washed with THF (2 × 2 mL). After the second rinse a solution of **2** (2.0 mM **2** dissolved in THF, 20 drops) was added to the zinc particles, the solution was capped, and the vial was swirled gently to mix the solution, and set aside for soaking. After soaking at room temperature for 24 h, the supernatant was removed from the mixture and the resulting zinc particles were washed with THF (3 × 2 mL). After the third rinse THF (2.0 mL) was added to the vial, the vial was swirled vigorously to suspend the zinc particles in solution, and the resulting slurry was partitioned into three aliquots containing THF and zinc, and then put into separate reaction cells. To each cell was added one of the homemade salt-containing pockets. The amounts of each salt in each pocket were: lithium chloride (8.5 mg, 0.20 mmol), TBAC (56 mg, 0.20 mmol) The cells were then capped and carefully removed from the glovebox for imaging.

The cells were imaged for 11 min each. Zinc particles with fluorescent signals were found and kept in focus. After imaging the reaction cell for 40 s and observing the surface bound intermediate, the salt was added by inverting the cell and gently shaking the cell, this was repeated three times. After putting the cell back onto the microscope, zinc particles were found and brought into focus at 100 s after the salt addition and these particles were kept in focus until 540 s after the addition, after which the stage was moved to find new zinc particles that had not yet been exposed to laser illumination. Data from the triplicate runs can be seen in Figure 3.5.

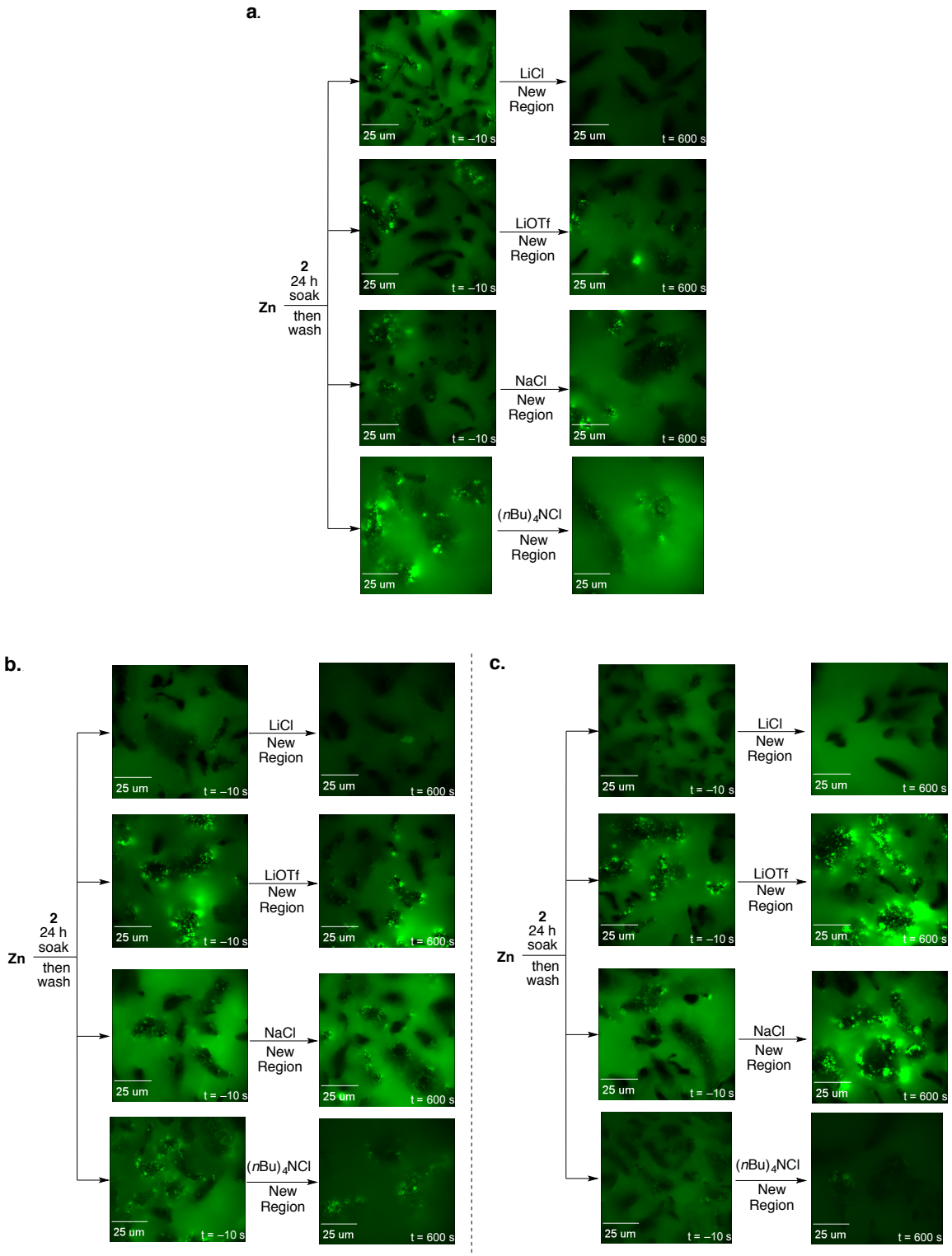

Figure 3.5. Results from triplicate salt addition experiments. *a* is the same data set shown in the Results and Discussion section.

Addition of Water Experiments. In a glovebox filled with nitrogen, a 1 dram vial was charged with zinc (50. mg, 0.76 mmol), THF (1.0 mL), and trimethylsilyl chloride (1 drop). The mixture was then capped and agitated gently to mix the solution. After soaking at room temperature for 2 h, the supernatant was removed from the mixture and the resulting zinc particles were washed with THF (2 × 2 mL). After the second rinse a solution of **2** (2.0 mM of **2** dissolved in THF, 20 drops) was added to the zinc particles, the solution was capped, and the vial was swirled gently to mix the solution, and set aside for soaking. After soaking at room temperature for 24 h, the supernatant was removed from the mixture and the resulting zinc particles were washed with THF (3 × 2 mL). After the third rinse THF (2.0 mL) was added to the vial, the vial was swirled vigorously to suspend the zinc particles in solution, and the resulting slurry was partitioned into three aliquots containing THF and zinc, and then put into separate reaction cells. The cells were then capped (with a cap that included a septum) then carefully removed from the glovebox for imaging.

The cells were imaged for 11 min each. Zinc particles with fluorescent signals were found and kept in focus. After imaging the reaction cell for 40 s and observing the surface bound intermediate, water (50.0 μL, 0.200 mmol) was then syringed through the septum. After putting the cell back onto the microscope, zinc particles were found and brought into focus at 100 s after the water addition and these particles were kept in focus until 540 s after the addition, after which the stage was moved to find new zinc particles that had not yet been exposed to laser illumination. Data for the triplicate runs can be seen in Figure 3.6.

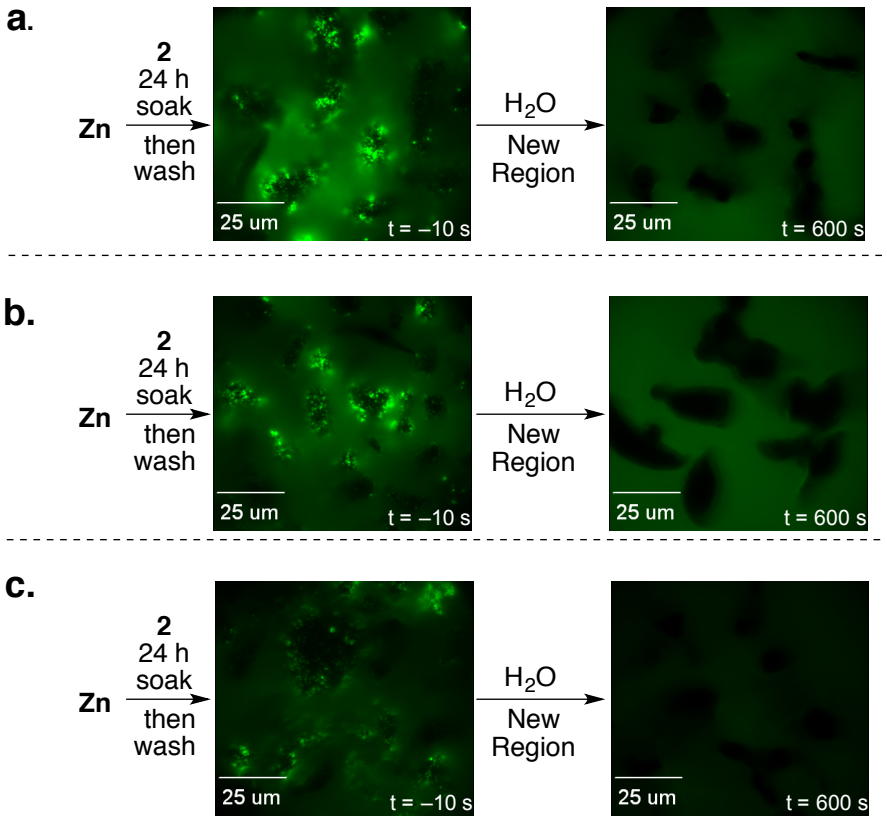

Figure 3.6. Results from triplicate water addition experiments. *a* is the same data set shown in the Results and Discussion section.

Control Experiments for Probes 2 and 5. In a glovebox filled with nitrogen, a 1 dram vial was charged with zinc (50 mg, 0.76 mmol), THF (1.0 mL), and trimethylsilyl chloride (1 drop). The mixture was then capped and agitated gently to mix the solution. After soaking at room temperature for 2 h, the supernatant was removed from the mixture and the resulting zinc particles were washed with THF (2 × 2 mL). After the second rinse a solution of either **2** or **5** (2.0 mM **2** or **5** dissolved in THF, 20 drops) was added to the zinc particles, the solution was capped, and the vial was swirled gently to mix the solution, and set aside for soaking. After soaking at room temperature for 24 h, the supernatant was removed from the mixture and the resulting zinc particles were washed with THF (3 × 2 mL). After the third rinse THF (1.0 mL) was added to the vial, the vial was swirled vigorously to suspend the zinc particles in solution,

and the resulting slurry was put into a reaction cell. The cell were then capped and carefully removed from the glovebox for imaging. This was done at total of three times for the alkyl iodide probe **2** and three times for the control probe **5**. Figure 3.7 shows these results.

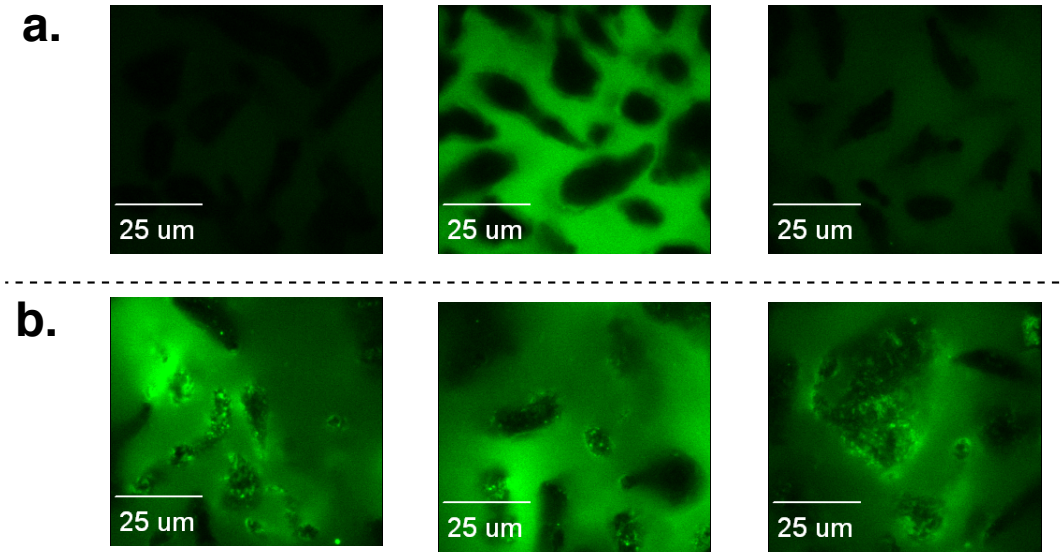

Figure 3.7. Results from control experiments. (a) From soaking zinc in control probe, **5**. (b) From soaking zinc in alkyl iodide probe, **2**.

Solution Preparation for Quenching Experiments. Five working standards containing **2** and ZnX_2 (X = Cl or I) were prepared at various concentrations (Table 3.1). First, a stock solution containing 2.0 mM of **2** dissolved in THF was made by weighing **2** (4.3 mg, 10. μmol) directly into a 5.0 mL volumetric flask and diluting to calibration line with THF. From this 2.0 mM stock solution a 2.0 μM solution of **2** dissolved in THF was made by syringing 50.0 μL of the 2.0 mM stock solution into a 50.0 mL volumetric flask and diluting to the calibration line with THF. This 2.0 μM solution of **2** dissolved in THF was used for all subsequent dilutions of ZnX_2.

Working Standard	[ZnX_2] (μM)	[2] (μM)
1	1.0	2.0
2	2.0	2.0
3	3.0	2.0
4	4.0	2.0
5	50.0	2.0

Table 3.1. Concentration of zinc salt and 2 in the working

For the zinc salts, a 50.0 mM solution of ZnX_2 dissolved in the 2.0 μM solution of **2** was prepared by weighing the zinc salt directly into a 10.0 mL volumetric flask (159.6 mg ZnI_2, 0.5000 mmol ZnI_2 or 68.2 mg $ZnCl_2$, 0.500 mmol $ZnCl_2$) and diluting to the calibration line with the 2.0 μM solution of **2** dissolved in THF. From this solution was then made a 50.0 μM solution of ZnX_2 dissolved in the 2.0 μM solution of **2** by syringing 10.0 μL of the 50.0 mM solution directly into a 10.0 mL volumetric flask and diluting to calibration line with 2.0 μM solution of **2** in THF.

Working solution were then prepared by syringing an appropriate amount (100, 200, 300, or 400 μL) of the 50.0 μM ZnX_2 solution into a 5.0 mL volumetric flask and diluting to calibration line with the 2.0 μM solution of **2** in THF. This afforded the working standards with concentrations seen in Table 3.1.

$ZnCl_2$ and ZnI_2 Quenching Experiments. The absorption spectrum of **2** (2.0 μM solution of **2** dissolved in THF) was measured on a Cary 50 absorption spectrometer (Figure 3.8).

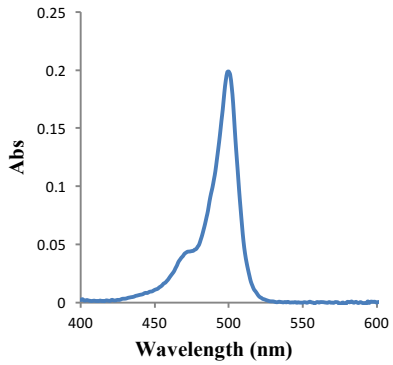

Figure 3.8. Absorbance spectrum of **2** (2.0 μM) in THF; λ_{max} = 500 nm. The data and graph in this figure were collected and produced by Chao Feng.

Emission spectra of the five stock solutions and the 2.0 μM solution of **2** dissolved in THF were taken for each zinc salt. The spectra were acquired on a Cary Eclipse fluorescence spectrometer with an excitation wavelength of 488 nm, fast scan rate, 2.5 nm excitation and emission slit width at a PMT voltage of 800 V.

References

1. Grignard, V. Compt. Rend. 1900, 130, 1322–1325.

2. Huryn, onds, Part 1. pp. 49–75, 1991.

3. Porter, Frank C. (1994). Corrosion Resistance of Zinc and Zinc Alloys. CRC Press. p. 121

4. Rieke, R. D.; Li, P. T.; Burns, T. P.; Uhm, S. T. J. Org. Chem. 1981, 46, 4323–4324.

5. Wu, T.-C.; Xiong, H.; Rieke, R. D. J. Org. Chem. 1990, 55, 5045–5051.

6. Krasovskiy, A.; Malakohov, V.; Gavryushin, A.; Knochel, P. Angew. Chem. Int. Ed. 2006, 45, 6040–6044.

7. Ochiai, H.; Jang, M.; Hirano, K.; Yorimitsu, H.; Oshima, K. Org. Lett. 2008, 2681–2683.

8. Metzger, A.; Schade, M. A.; Knochel, P. Org. Lett. 2008, 10, 1107–1110.

9. Gong, H.; Gagne, M. R. J. Am. Chem. Soc. 2008, 130, 12177–12183.

10. Peng, Z.; Knochel, P. Org. Lett. 2011, 13, 3198–3201.

11. Bluemke, T.; Chen, Y.-H.; Peng, Z.; Knochel, P. Nat. Chem. 2010, 2, 313–318.

12. Shen, Z.-L.; Knochel, P. Chem. Eur. J. 2015, 21, 7061–7065.

13. Esfandiari, N. M.; Wang, Y.; Bass, J. Y.; Cornell, T. P.; Otte, D. A. L.; Cheng, M. H.; Hemminger, J. C.; McIntire, T. M.; Mandelshtam, V. A.; Blum, S. A. J. Am. Chem. Soc. 2010, 132, 15167–15169.

APPENDIX A:

Progress Towards the Synthesis of

Water-Soluble Metal Hydrides

Introduction

There is interest in developing electrocatalysts for the reduction of CO_2 utilizing water as the solvent. Water is generally considered to be environmentally and economically less concerning relative to organic solvents. Water can also be used as a renewable source of protons for generating M–H. The proton activity can easily be tuned by adjusting the pH. One of the most notable reasons for using water as the solvent for CO_2 reduction is because it has been demonstrated that transition metal hydrides become stronger hydride donors in water relative to HCO_2^-.[1-2] In acetonitrile, the free energy for hydride transfer from $[HNi(dhmpe)_2]^+$ (R = CH_2OH in schem A.1; ΔG^o_{H-} = 57.4 kcal/mol) to CO_2 (ΔG^o_{H-} = 44 kcal/mol) is endergonic by over 13 kcal/mol; however, when the solvent is water the free energy for hydride transfer is endergonic by only 6 kcal/mol.[2] It has been proposed that this non-linear free energy change for hydride transfer to CO_2 when switching from acetonitrile to water is due to the stabilization of the negatively charged HCO_2^- anion by hydrogen bonding.[3] First-row transition metals are generally not hydridic enough to reduce CO_2 in acetonitrile. This phenomenon was utilized to synthesize first-row transition metal hydrides, which generally are not hydridic enough in acetonitrile to reduce CO_2. Yang and Ceballos showed that in acetonitrile hydride transfer from $[HNi(tmepe)_2]^+$ (R = $CH_2CH_2OCH_3$ in Scheme A.1) to CO_2 is endergonic by near 7 kcal/mol, but in water is exergonic by 1.3 kcal/mol; however in this case hydride transfer was noted to be kinetically

slow.[4] Another notable example comes from Berben and colleagues where CO_2 reduction by $[HFeN(CO)_{12}]^-$ is unfavorable in acetonitrile, but is nearly 9 kcal/mol favorable in water; this compound remains the fastest electrocatalyst that selectively reduces CO_2 to HCO_2^- since its initial discovery in 2011.[5-6] Water poses a unique method for tailoring metal hydride electrocatalysts to be sufficiently hydridic for CO_2 reduction.

Scheme A.1. Nickel *bis*(diphosphine)

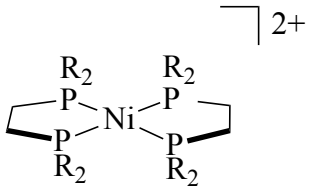

There are, however, current limitations for using water as solvent for CO_2 reduction. Currently there are very few number of measured hydricity values in water, thus there is a need to expand this to observe more trends and ultimately rationally develop future catalyst. In addition, transition metal complexes are not always inherently soluble in water and even if they are, the compounds often decompose in water. To achieve water solubility of diphosphine compounds of interest for CO_2 reduction, water-solubilizing sulfonate groups are appended to the ligand backbone of a *bis*(diphosphine). The two ligands of interest, dppbzts ((1,2-*bis*(diphenylphosphino)benzene tetrasulfonate) and dppets (1,2-*bis*(diphenylphosphino)ethane tetrasulfonate) can be seen in Scheme A.2. The dppbzts ligand was chosen because it is commercially available, the synthesis of dppets has been reported, and there are already various *bis(*dppe) metal hydrides that have reported hydricities in acetonitrile, which permits correlations to be made between the two solvents.

Scheme A.2. The Water-Solubilizing Ligands Used in this Study

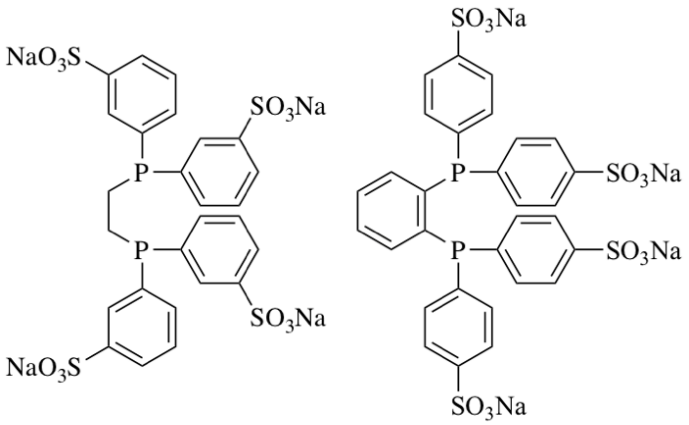

$[Na]_4[dppets]$ **$[Na]_4[dppbzts]$**

The corresponding earth-abundant nickel(II) complexes coordinated with two of these ligands were investigated. Nickel was chosen because various *bis*(diphosphine) nickel hydrides have been reported and are generally diamagnetic. Specifically, the hydricity of $[HNi(dppe)_2]^+$, which is clostest in structure to the sulfonated ligands, has been measured to be 62 kcal/mol in acetonitrile. For this compound, the reaction with CO_2 is energonic. Based on the changes in hydricitity expected when switching to water, it is anticipated hydride transfer to CO_2 may be exergonic. Herein, the synthesis of $[Na]_6[Ni(dppbzts)_2]$ and $[Na]_6[Ni(dppets)_2]$ are reported, in addition to their stability in water and various buffer systems.

Results and Discussion

The nickel compounds, $[Na]_6[Ni(dppbzts)_2]$ and $[Na]_6[Ni(dppets)_2]$, were synthesized by addition of a water solution containing the corresponding ligand (2.0 equiv) to a solution of $[Ni(H_2O)_6][BF_4]_2$ dissolved in water.

For $[Na]_6[Ni(dppbzts)_2]$, the addition of ligand to the Ni^{2+} precursor resulted in a color change from green to light orange/yellow and is accompanied by a 72 ppm down-field shift of the resonance in the $^{31}P\{^1H\}$ NMR from –14.4 ppm for the free ligand to 57.2 ppm for the

reaction mixture (Figure A.1). Salt contamination is often a problem, either from sodium on the ligands with counter anions of the metal precursor, or the commercially available dppbzts which is suspected to have sodium chloride impurities. Because salt contamination poses an issue, the crude solid was triturated with copious amounts of methanol, which $NaBF_4$ is soluble, and the desired product was anticipated to be sparingly soluble at best in. After triturating with methanol and decanting 6 times, the resonance attributed to $NaBF_4$ around 0 ppm in the ^{11}B NMR spectrum is no longer present (Figure A.2).

The single resonance that is observed in the $^{31}P\{^1H\}$ NMR spectrum of the product, reaction stoichiometry, and the lack of byproduct formation in the crude reaction mixture in the $^{31}P\{^1H\}$ NMR together indicate that the nickel is coordinated by two identical diphosphine ligands. In conjunction with the lack of $NaBF_4$, this gives rise to the proposed formula of $[Na]_6[Ni(dppbzts)_2]$, which contains sodium counter ions, based off of the mass balance.

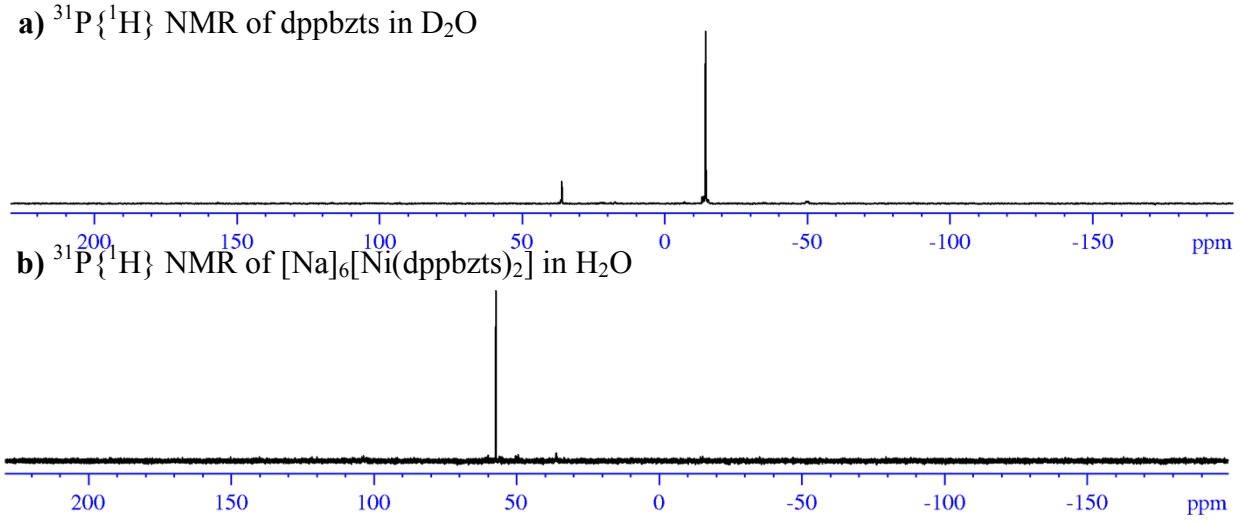

Figure A.1. $^{31}P\{^1H\}$ NMR spectra of a) dppbzts in D_2O and b) the reaction mixture of dppbzts (2.0 equiv) with $[Ni(H_2O)_6][BF_4]_2$ in H_2O.

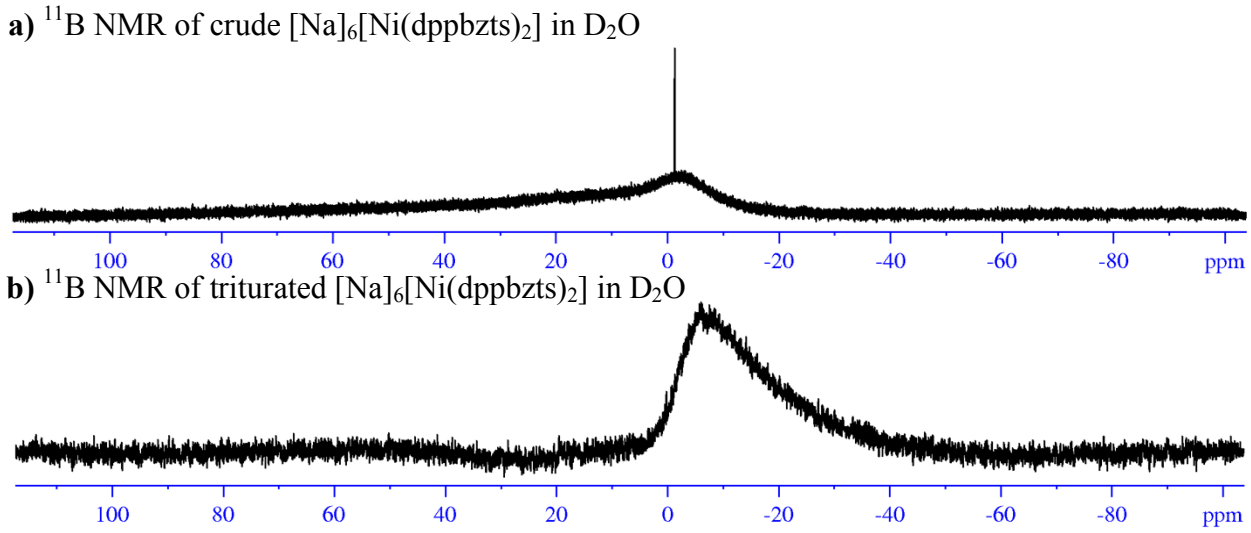

Figure A.2. ^{11}B NMR spectra of a) crude $[Na]_6[Ni(dppbzts)_2]$ b) the same sample after triturating with CH_3OH. Both samples are in D_2O. Note that the broad peak present in both spectra are attributed to borosilicate present in the glass of the NMR tube.

$[Na]_6[Ni(dppets)_2]$ was isolated in a similar manner. Addition of 2 equiv of dppets to the $[Ni(H_2O)_6][BF_4]_2$, precursor resulted in a color change from green to dark orange and is accompanied by a 74 ppm down-field shift of the resonance in the $^{31}P\{^1H\}$ NMR from –13.3 ppm for the free ligand to 59.2 ppm for the reaction mixture (Figure A.2). Unexpectedly, this compound has a higher solubility in methanol than does the dppbzts analogue. As a result, the excess $NaBF_4$ cannot be removed using the same procedure for the dppbzts analogue.

The single resonance that is observed in the $^{31}P\{^1H\}$ NMR spectrum of the product and the fact that 2 equiv of phosphine were added (with no apparent formation of by products in the crude reaction mixture) together indicate that the nickel is coordinated by magnetically equivalent diphosphine ligands. Based solely on this notion, this gives rise to the proposed formula of $[Na]_6[Ni(dppbzts)_2]$ strictly based off of the mass balance and with the product containing a signification amount of $NaBF_4$.

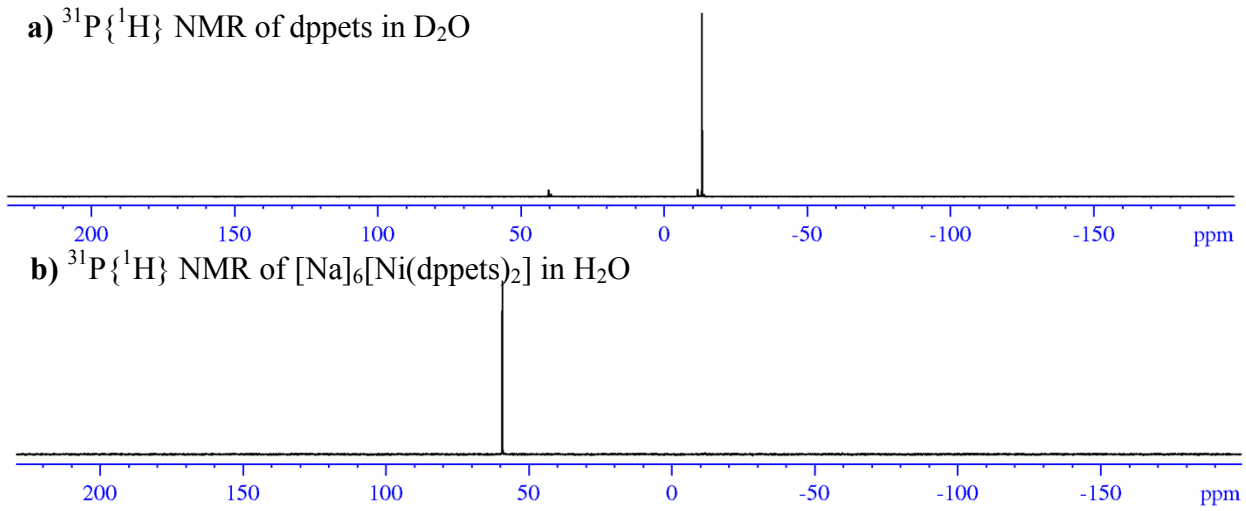

Figure A.3. $^{31}P\{^{1}H\}$ NMR spectra of a) dppets in D_2O and b) the reaction mixture of dppets (2.0 equiv) with $[Ni(H_2O)_6][BF_4]_2$ in H_2O.

The stability of these compounds in water was assessed by observing the ^{1}H NMR spectra over time. The ^{1}H NMR of $[Na]_6[Ni(dppbzts)_2]$ in D_2O was taken and the aromatic resonances corresponding to the ligand were integrated relative to dimethyl sulfoxide (DMSO), which is present as an impurity in the commercially available ligand. The integration of $[Na]_6[Ni(dppbzts)_2]$/standard (dmso) was 5.87/10.0). After sitting under dinitrogen (J-Young tube) for 1 d, the integrations were determined to be 5.48/10.0. The amount of $[Na]_6[Ni(dppbzts)_2]$ appears to go down by a factor of 0.93 relative to the dmso standard. This is likely within error, especially considering the how convoluted the aromatic region appears to be. If within error, provides evidence that $[Na]_6[Ni(dppbzts)_2]$ is stable in water over the course of a day. In either case, even if $[Na]_6[Ni(dppbzts)_2]$ is decomposing it is at a slow enough rate such that water is a suitable solvent over the timescales of a typical electrochemical experiments.

For the stability of $[Na]_6[Ni(dppets)_2]$ in water, the ^{1}H NMR integrations of a freshly-prepared solution in D_2O were determined to be 11.25/1.00 ($[Na]_6[Ni(dppets)_2]$/acetone

standard). After sitting for 1 d, the integrations were 11.51/1.00 (Figure A.5), or within error of the experiment. Thus, $[Na]_6[Ni(dppets)_2]$ is stable over the course of a day in water.

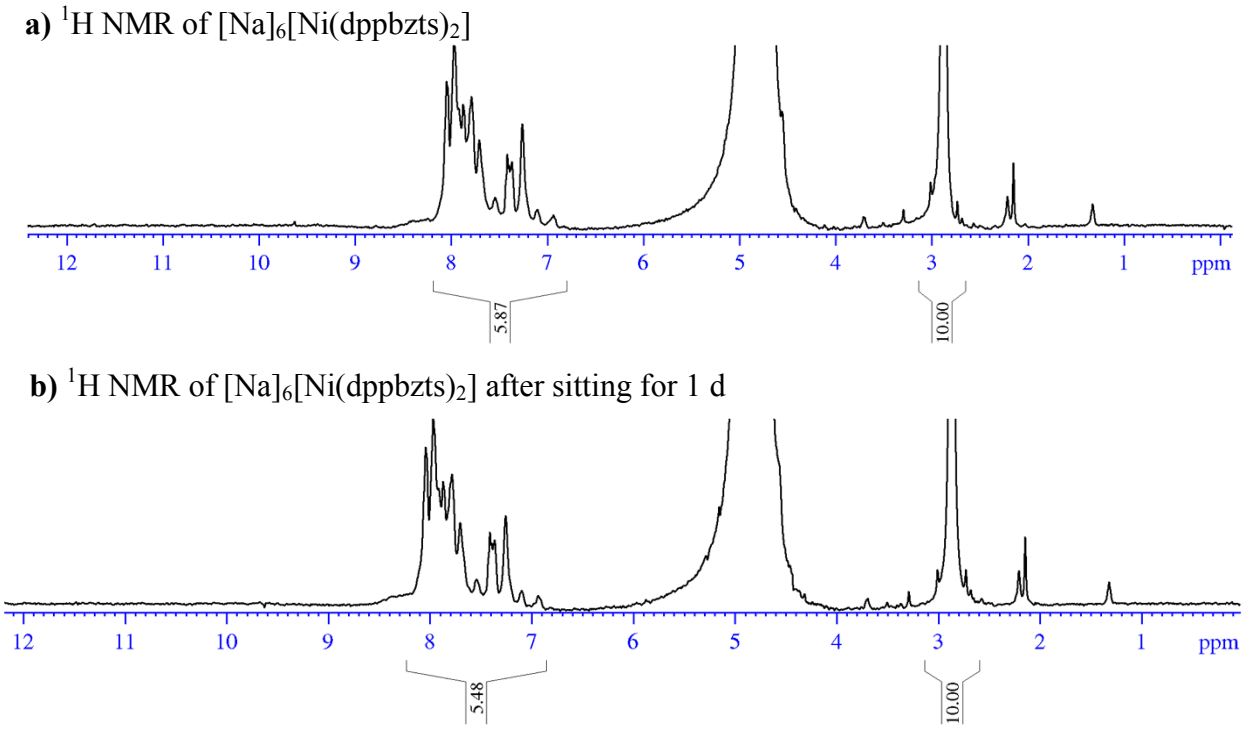

Figure A.4. ^{1}H NMR spectra of $[Na]_6[Ni(dppbzts)_2]$ (10 mM) in D_2O: a) freshly prepared NMR sample and b) the same NMR sample after 24 h.

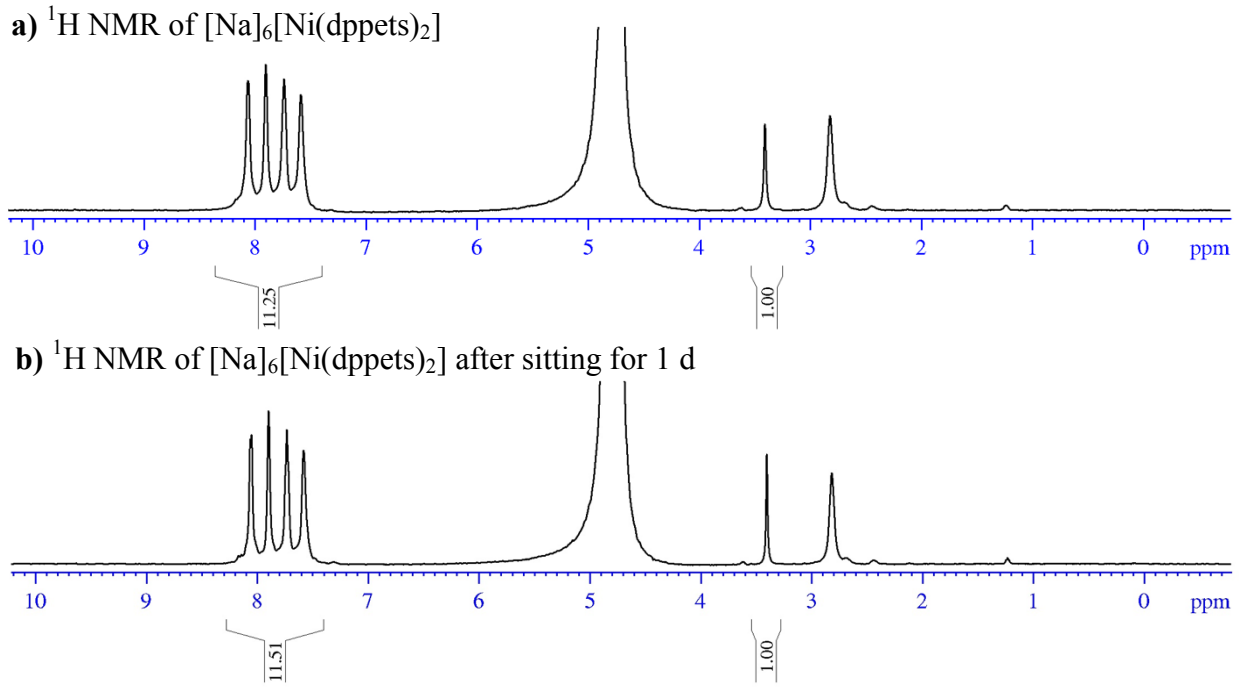

Figure A.5. ^{1}H NMR spectra of [Na]$_6$[Ni(dppets)$_2$] (10 mM) in D_2O: a) freshly prepared NMR sample and b) the same NMR sample after 24 h.

With evidence in hand that these compounds are stable in water, the stability of the compounds under catalytic relevant conditions was investigated. This includes the presence of protons, which are required to generate the metal hydride. In water, the proton activity is adjusted by changing the pH. Assuming these compounds are sufficiently hydridic in water to reduce CO_2, then they must have $\Delta G^{o}_{H^-} \leq 24$ (i.e. the hydricity of HCO_2^- in water).[3,7-8] If that is the case, then in order to circumvent unproductive HER, the pH of the solution must ≥ 7.5.

Sodium bicarbonate was initially chosen as a buffer due to its cost, availability, and is commonly employed as a buffer in aqueous hydrogenation of CO_2. The ^{31}P{^{1}H} NMRs for [Na]$_6$[Ni(dppbzts)$_2$] and [Na]$_6$[Ni(dppets)$_2$] with can be seen in Figure A.6 and Figure A.7, respectively, and they both exhibit identical behavior. After the addition of 1.0 equiv of sodium bicarbonate the peak corresponding to [Na]$_6$[Ni(dppbzts)$_2$] completely disappears and the

intensity of the peak corresponding to the doubly-oxidized ligand appears to grow in relative to the free ligand. After sitting for 24 h a new peak, ca. 15 ppm up field of $[Na]_6[Ni(dppbzts)_2]$, is observed; the intensity of the new resonances in both appears to be much less than the original (based on comparison to the baseline impurities around 55 ppm).

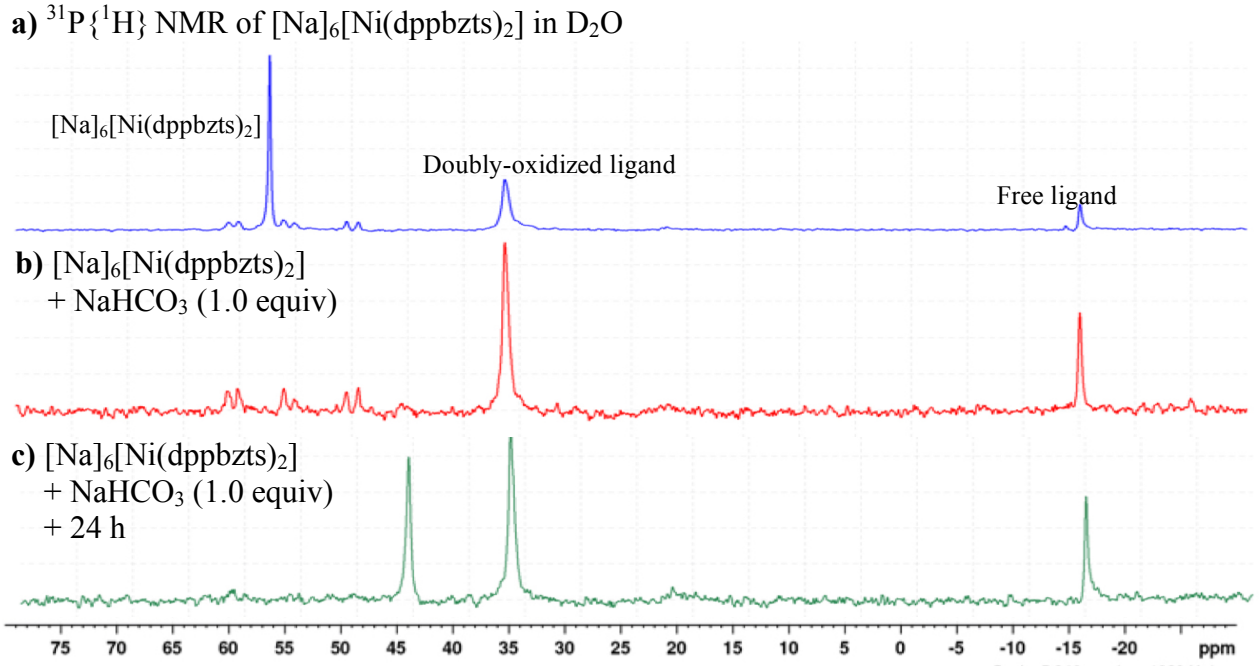

Figure A.6. $^{31}P\{^1H\}$ NMR spectra of $[Na]_6[Ni(dppbzts)_2]$ (19.6 mM) in D_2O a) freshly prepared solution, b) after the addition of $NaHCO_3$ (1.0 equiv), and c) after sitting for 24 h.

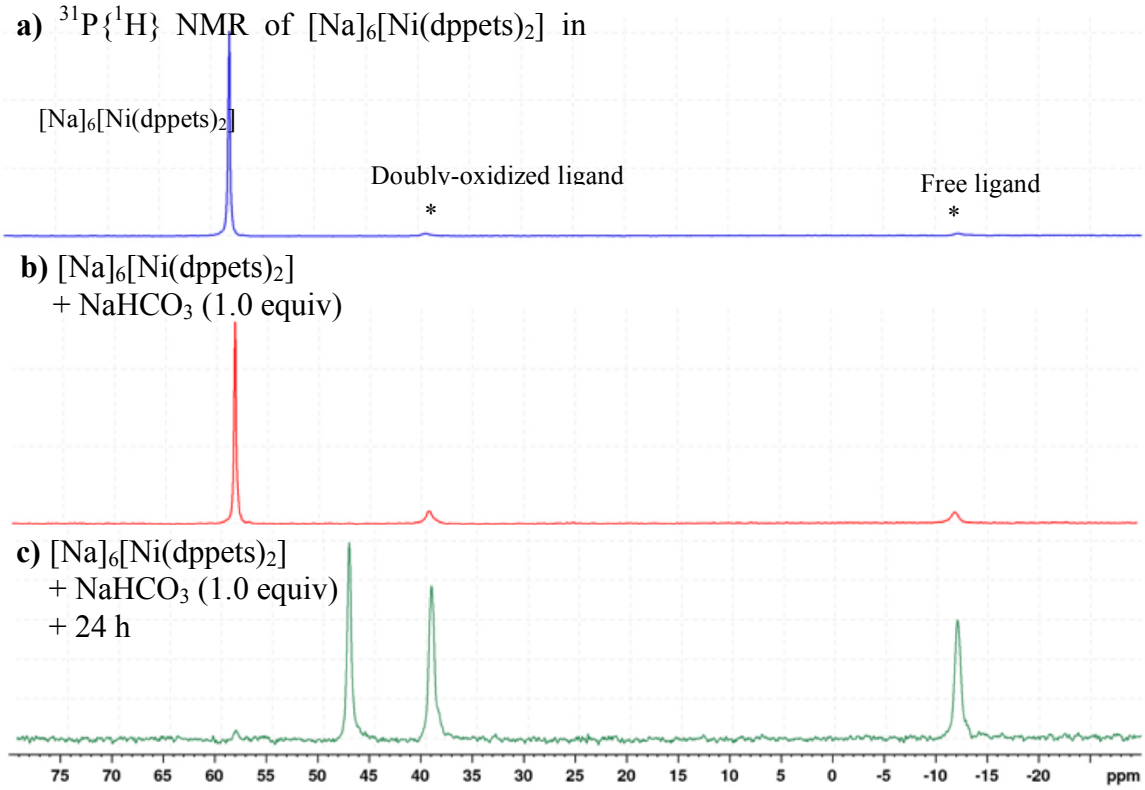

Figure A.7. $^{31}P\{^{1}H\}$ NMR spectra of $[Na]_6[Ni(dppets)_2]$ (20.1 mM) in D_2O a) freshly prepared solution, b) after the addition of $NaHCO_3$ (1.0 equiv), and c) after sitting for 24 h.

In the freshly prepared NMR sample of both $[Na]_6[Ni(dppbzts)_2]$ and $[Na]_6[Ni(dppets)_2]$, a resonance around 37 ppm corresponding to doubly-oxidized phosphine cis sometimes present (this resonance can also be seen in the $^{31}P\{^{1}H\}$ of the free ligand in Figure A.1a) as well as a resonance around –15 ppm corresponding to free ligand; these resonances are present in a roughly 4.3/1.0 ratio for $[Na]_6[Ni(dppbzts)_2]$ and 0.8/1.0 ratio for $[Na]_6[Ni(dppets)_2]$. After 1.0 equiv of sodium bicarbonate is added and the resonances corresponding to both nickel *bis*(diphosphine) compounds disappear, the free ligand appears to grow in relative to the doubly-oxidized ligand (3.0/1.0 for $[Na]_6[Ni(dppbzts)_2]$ and 1.1/1.0 for $[Na]_6[Ni(dppets)_2]$). It is evident by inspecting the intensity of the oxidized and free ligand, that the total nickel species are likely not conserved, as small amounts of both species the ligand species are being generated while the

resonance for the complexes are completely gone. Thus, it is believed the pathway for which both compounds are decomposing results in a soluble product (no precipitate was observed) that is NMR-silent. A possible explanation for this is formation of a 6-coordiante nickel(II) species (via potential binding of HCO_3^-, CO_3^{2-}, or HO^-), which would be expected to be paramagnetic. More interesting is the appearance of the new resonance at 44 ppm after sitting for 24 h. A possible explanation for this new resonance is slow dissociation of one of the diphosphine ligands after formation of a potential 6-coordinate nickel(II) species and subsequent double oxidation of the free phosphine (doubly-oxidized ligand grows in relative to free ligand after 24 h). This plausible pathway can be seen in eq A.1. Of course, this pathway is speculative and more experimentation would be needed to confirm this possibility. Ultimately, this experiment demonstrates that these nickel compounds are not stable in bicarbonate-buffered water. In a desperate attempt to find a suitable buffer system, the following other buffers were screened and exhibited similar behavior (data not shown): TAPS (pH 10.5), MES/HEPS (0.1 M each, pH 8.0), and even NaOH (titration).

$$[Ni^{II}(P_2)_2] \xrightarrow{+\,2\,X^-} \underset{\text{NMR Silent}}{[Ni^{II}(P_2)_2X_2]^{2-}} \xrightarrow[-\,1\,P_2]{} [Ni^{II}(P_2)X_2]^{2-} \qquad \text{(A.1)}$$

Conclusions and Future Directions

These experiments indicate that Ni(II) coordinated with the dppets or dppbzts seem to react with buffered aqueous solutions and hence are not suitable for our target reaction. Insight into the decomposition pathway could provide to be fruitful in preventing such decomposition pathways from happening. It is speculated that these compounds are forming 6-coordinate nicked(II) species upon addition to the aqueous buffers discussed. It is interesting to note that there are

several Ni(II) *bis*(diphosphines) that are stable in water and even have reported hydricities in water. Among these are $[Ni(dhmpe)_2]^{2+}$ (R=CH_2OH; Scheme A.1),[2,9-10], $[Ni(tmepe)_2]^{2+}$ (R=$CH_2CH_2OCH_3$),[4] and an example from Appel et al. where R= $CH_2CH_2CH_2OCH_3$.[11] A noticeable difference is that these reported (and stable) examples have alkyl or ether groups on the phosphine ligands while dppbzts and dppets contain phenyl groups, over which the lone pair of the phosphorus can be delocalized. It is speculated that perhaps the less donating phenyl groups provide a relatively electron-deficient nickel(II) center that is susceptible to the binding of exogenous anions.[12-15]

The dearth of these tetra-sulfonated and highly water-soluble ligands and corresponding metal complexes in the literature is perhaps due to the difficulties in purification and thus characterization. Difficulties associated with purifying and characterizing sulfonated compounds are well documented in the literature with several papers publishing a crystal structure of a sulfonated phosphine using chelating agents and even guanidinium salts that make ordered hydrogen-bonding networks and crystalline products.[12-15] Various attempts to incorporate chelating agents or guanidinium salts have proven to be futile. Future efforts toward purification and isolation may look towards biology and biochemistry and how water-soluble compounds are purified and crystallized. Several attempts to purify the transition metal compounds by ion exchange chromatography were not successful; however, with careful optimization this method seems promising. Lyophilizing water solutions is an attractive method for water removal, which often requires significant time periods even at elevated temperatures; ChemGlass even manufactures a glass lyophilizer for use on a Schlenk line.

Experimental

Synthesis of dppets. This was prepared according to a literature procedure[16] in 46% yield. ^{1}H NMR (D_2O, 600 MHz) δ = 7.88 (br, 4H), 7.81 (br/m, 4H), 7.51 (br, 4H), 7.49 (br, 4H), 2.25 (t, $^{2}J_{P-H}$ = 4.80 Hz, 4H). $^{31}P\{^{1}H\}$ NMR (D_2O, 243 MHz): δ = –13.3 (s). These spectra are in agreement of previously reported spectral data.

To aid in future synthesis, the chemical shifts of the protonated dppets and protonated starting material, dppe, are reported for monitoring the slow reaction progress (doubly protonated at each phosphine under reaction conditions; Figure B.9). dppets•2H^{+}: $^{31}P\{^{1}H\}$ NMR (H_2SO_4, 600 MHz): δ = 11.2 (s). dppe•2H^{+}: $^{31}P\{^{1}H\}$ NMR (H_2SO_4, 600 MHz): δ = 10.4 (s) (see Figure 8 for $^{31}P\{^{1}H\}$ NMR spectrum of the reaction mixture).

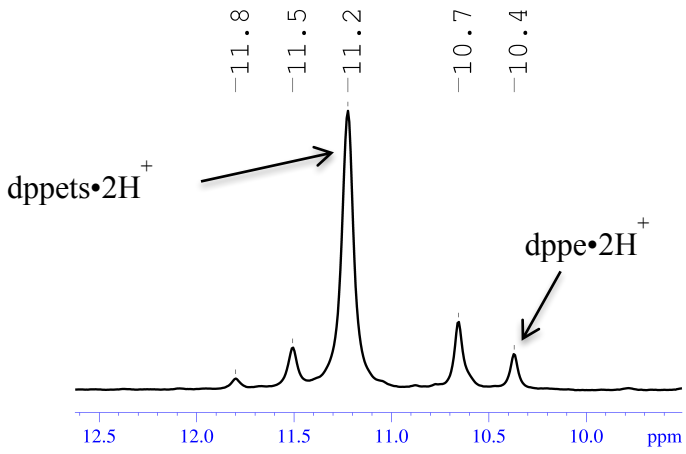

Figure A.8. An aliquot of the crude reaction mixture for this synthesis of dppets highlighting protonated dppets (dppets•2H^{+}) and protonated dppe (dppets•2H^{+}).

Synthesis of $[Na]_6[Ni(dppbzts)_2]$. Under a dinitrogen atmosphere, a CH_3CN/H_2O solution (1/1, 10 mL) containing $[Ni(H_2O)_6][BF_4]_2$ (186 mg, 0. 547 mmol) was added to solid dppbzts (934 mg, 1.09 mmol; purchased from Strem and contains significant dmso impurities!). This resulted in an immediate color change to dark orange. After stirring for 12 h, the solution

was reduced in vacuo at 50 ºC and triturated with methanol (4 × 10 mL) and then washed with ether (3 × 5 mL). Upon drying in vacuo, a pale orange solid was yielded (400 mg, 42%). ^{1}H NMR (D_2O, 600 MHz) δ/ppm = 6.73–8.00 (m). $^{31}P\{^{1}H\}$ NMR (D_2O, 243 MHz): δ = 57.2 (s).

Synthesis of $[Na]_6[Ni(dppbzts)_2]$. Under a dinitrogen atmosphere, a CH_3CN/H_2O solution (1/1, 5 mL) containing $[Ni(H_2O)_6][BF_4]_2$ (82.4 mg, 0.242 mmol) was added to solid dppets (390 mg, 0.484 mmol). This resulted in an immediate color change to dark orange. After stirring for 12 h, the solution was reduced in vacuo at 50 ºC and triturated with methanol (11 × 3 mL) and then washed with ether (3 × 5 mL). Upon drying in vacuo, a pale orange solid was yielded, which was contaminated with $NaBF_4$. ^{1}H NMR (D_2O, 600 MHz) δ/ppm = 2.76 (t, 8H), 7.54 (s, 8H), 7.69 (t, 8H), 7.85 (s, 8H), 8.01 (d, 8H). $^{31}P\{^{1}H\}$ NMR (D_2O, 243 MHz): δ = 59.2 (s).

References

1. Creutz, C.; Chou, M. H. *J. Am. Chem. Soc.* **2007**, *129*, 10108-10109.

2. Tsay, C.; Livesay, B. N.; Ruelas, S.; Yang, J. Y. *J. Am. Chem. Soc.* **2015**, *137*, 14114-14121.

3. Connelly Robinson, S. J.; Zall, C. M.; Miller, D. L.; Linehan, J. C.; Appel, A. M. *Dalton Trans.* **2016**, *45*, 10017-10023.

4. Ceballos, B. M.; Yang, J. Y. *Proc. Natl. Acad. Sci.* **2018**, *115*, 12686-12691.

5. Taheri, A.; Thompson, E. J.; Fettinger, J. C.; Berben, L. A. *ACS Catal.* **2015**, *5*, 7140-7151.

6. Rail, M. D.; Berben, L. A. *J. Am. Chem. Soc.* **2011**, *133*, 18577-18579.

7. Curtis, C. J.; Miedaner, A.; Ellis, W. W.; DuBois, D. L. *J. Am. Chem. Soc.* **2002**, *124*, 1918-1925.

8. Pitman, C. L.; Brereton, K. R.; Miller, A. J. M. *J. Am. Chem. Soc.* **2016**, *138*, 2252-2260.

9. Tsay, C.; Ceballos, B. M.; Yang, J. Y. *Organometallics* **2019**, *38*, 1286-1291.

10. Tsay, C.; Yang, J. Y. *J. Am. Chem. Soc.* **2016**, *138*, 14174-14177.

11. Burgess, S. A.; Kendall, A. J.; Tyler, D. R.; Linehan, J. C.; Appel, A. M. *ACS Catal.* **2017**, *7*, 3089-3096.

12. Russell, V. A.; Etter, M. C.; Ward, M. D. *J. Am. Chem. Soc.* **1994**, *116*, 1941-1952.

13. Burrows, Andrew D.; Harrington, Ross W.; Mahon, Mary F.; Teat, Simon J. *Eur. J. Inorg. Chem.* **2003**, *2003*, 1433-1439.

14. Kathó, Á.; Bényei, A. C.; Joó, F.; Sági, M. *Adv. Synth. Catal.* **2002**, *344*, 278-282.

15. Bényei, A. C.; Gulyás, H.; Ozawa, Y.; Kimura, K.; Toriumi, K.; Kégl, T.; Bakos, J. *J. Organomet. Chem.* **2007**, *692*, 1845-1851.

16. Lucey, D. W.; Atwood, J. D. *Organometallics* **2002**, *21*, 2481-2490.

APPENDIX B:

Adaptable Ligand Donor Strength: Tracking Transannular Bond Interactions in *Tris*(2- pyridylmethyl)-azaphosphatrane (TPAP)

Introduction*

Ligands that can adapt their donor strength provide a versatile method for adjusting electronic structure in order to access reactive transition metal intermediates. For example, Peters et al. have extensively explored first row metal complexes with tripodal phosphine ligands containing a B, C, or Si hetero- atom, where the interaction between the metal and heteroatom adjusts depending on the metal oxidation state and identity of ligands trans to the interaction. [1-7] Parkin et al. have demon- strated that the flexible interactions of an apical carbon in atrane-type ligands contribute to unique reactivity, and that the interaction can be modified through ligand design.[8-9] Lu et al. designed tripodal ligands that encapsulate a Lewis acidic cation that can tune the electronic structure and reactivity at the metal.[10-13] In addition, the Agapie[14-28] and Meyer[29-31] labs have utilized phenyl or mesitylene linkers strategically positioned near a metal to serve as electron reservoirs to support multi-electron reactivity. In all of the above cases, the adaptable interaction is incorporated into flexible chelating ligands, and the degree of interaction can be evaluated by the metal-donor distance. Under some conditions the weak interaction is absent, formally changing the coordination environment around the metal and thus the electronic structure.

---

* Portions of this chapter have been published: Thammavongsy, Z.; Cunningham, D. W.; Sutthirat, N.; Eisenhart, R. J.; Ziller, J. W.; Yang, J. Y. *Dalton Trans.* **2018**, *47*, 14101–14110.

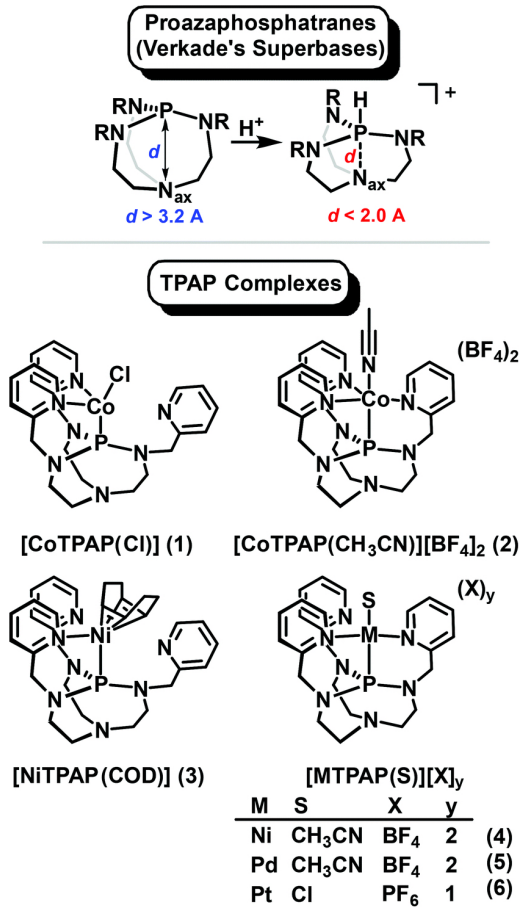

Figure B.1. TPAP complexes of interest in this study.

In a study led by Zachary Thammavongsy, a previous graduate student, an alternative type of adaptable interaction was described. The metal and donor maintain a fixed distance, but the latter can harness electron density through a transannular interaction when coordinated to more electron deficient metals. The ligand is based on proazaphosphatranes, a structurally unique class of neutral organic superbases more commonly known as Verkade's Superbases (Figure B.1, top).[32] These superbases are often used as a stoichiometric or catalytic Lewis base in a variety of organic transformations.[33-35] The pK_a of the protonated form, or azaphosphatrane, ranges from 32.8 to 34.5 in acetonitrile depending on the substituents attached to the equatorial nitrogen atoms (R).[32,36] The extreme basicity of proazaphosphatranes stems from the formation of a stable

three-centered four-electron transannular bond10 between P and N_{ax} atoms in complexes **1**, **2**, **4**, **5**, and **6** (Figure B.1, bottom) and an analogue of complex **3**.

To provide additional support for Zachary Thammavongsy's experimental study, I performed density functional theory (DFT) calculations on some of his compounds. The study examined whether there were any bonding interactions between P and N_{ax} in several of his reported compounds.

Results and Discussion

DFT calculations were performed using the Gaussian09 program suite with the incorporated NBO 3.1 package at the M06 level of theory with 6–311G++(3df,3pd) basis set for 3rd row main groups, 6-311G**++ basis set for 2nd row main groups, and LANL2DZ basis set for all metals. Geometry optimizations of the complexes from the X-ray coordinates, followed by harmonic frequency calculations indicated that all of the calculated compounds are minima on the potential energy surface. A comparison of selected calculated and experimental geometrical parameters is tabulated in Table B.1.

Figure B.2. Depiction of the angle, θ, as the degree of puckering of the axial nitrogen out of the C–C–C plane

We propose the shortening of the P···N_{ax} distance with concomitant puckering of the axial nitrogen above the plane of the three adjacent carbon atoms (θ in Figure B.2) was due to electron donation between the axial nitrogen (N_{ax}) and the phosphorus atom of the azaphosphatrane unit. To probe the nature of the P···N_{ax} interaction and observe electron density in a chemically

intuitive manner, an analysis utilizing natural bond orbital (NBO) perturbation theory was carried out with a focus on the NBOs of the M–P–N_{ax} fragment. All calculated values for each

Table B.1. Bond lengths and Angles of Complexes 1–6

	1	2	3	4	5	6
P_1–N_1 ($P\cdots N_{ax}$) (Å)	3.2647(14)	2.877(2)	3.3915(17)	2.948(2)	2.6747(18)	2.927(4)
Calc. ($P\cdots N_{ax}$) (Å)	3.088	2.737	3.306	2.701	2.646	2.815
P_1–N_2 (Å)	1.7089(13)	2.035(2)	1.7101(16)	1.6500(19)	1.6722(17)	1.666(4)
P_1–N_3 (Å)	1.6892(13)	1.997(2)	1.6965(16)	1.6511(19)	1.6528(17)	1.649(4)
P_1–N_4 (Å)	1.6879(13)	2.094(2)	1.7007(16)	1.649(2)	1.6583(16)	1.642(4)
P_1–M (Å)	2.1675(5)	2.1693(7)	2.1642(5)	2.1670(7)	2.2294(5)	2.2245(11)
Calc. P–M (Å)	2.190	2.263	2.323	2.254	2.357	2.354
C_1–C_3–C_5 θ (°)	−9.1349	9.9140	−10.9882	13.0123	17.7932	8.8644
Calc. C_1–C_3–C_5 θ (°)	3.41	16.62	—	17.32	18.62	13.79

Metrics 5 and 6 were taken from one of two molecules in the asymmetric unit. Metal ion is denoted as M. Note that "Calc." represents a DFT-calculated value.

metal ion coordinated to TPAP utilized the complexes in Figure B.1 except [NiTPAP(COD)] (**3**). The latter could not be modeled computationally because the structure failed to converge to a minimum on the potential energy surface. The previously reported structure [Ni(κ^1-TPAP)$(CO)_2$] (**3b**)[37] was used as an alternative model for the transannular interaction of a Ni(0) bound to TPAP. Table B.2 summarizes the calculated stabilization energies for each compound.

When the oxidation state of the metal is greater than +1, there is significant donation from the lone pair (LP) of N_{ax} into unfilled antibonding NBOs. The LP(N_{ax}) → σ*(M–P) stabilization is ca. 2 kcal mol^{-1} for the case of Ni(II) and Co(II). For Co(I) and Ni(0), where minimal or no transannular interaction is observed experimentally, the stabilization energy is negligible (<0.5 kcal mol^{-1}). For second- and third-row metals the LP(Nax) → σ*(M–P)

interaction provides 7.2 kcal mol^{-1} and 3.1 kcal mol^{-1} of stabilization energy for Pd(II) and Pt(II), respectively. In addition to the $LP(N_{ax}) \rightarrow \sigma^*(M–P)$ donation, there is a significant interaction of the axial nitrogen with the three $\sigma^*(P–N_{eq})$ NBOs (Table B.2). These calculations suggest the interaction of the axial nitrogen with the phosphorus atom is the dominating factor that influences the puckering angle, θ, and $P\cdots N_{ax}$ distance.

Table B.2. Results of NBO Analysis of Donor–Acceptor Interactions in Compound Adducts, Estimated by Second-Order Perturbation theory, $E^{(2)}_{i\rightarrow j}$ (kcal mol^{-1})

Parameter	**1**	**2**	**3b**	**4**	**5**	**6**
$LP(N_{ax}) \rightarrow \sigma^*(M–P)$	<0.5	1.09	<0.5	2.09	7.23	3.11
$LP(N_{ax}) \rightarrow \sigma^*(P–N_{eq})$	<1.5	2.86	<1.5	6.74	8.05	4.22

The proposed interaction between the phosphorus atom and axial nitrogen can be seen by visualizing the highest occupied molecular orbitals (HOMO) for Ni(0) and Ni(II) (Figure B.3). In the case of Ni(0), which lacks any significant $P\cdots N_{ax}$ interactions, the axial nitrogen contributes only 7% to the HOMO and does not interact with any orbitals of phosphorus; however, for Ni(II) the axial nitrogen contributes 51% to the HOMO and results in a shortening on the $P\cdots N_{ax}$ as well as a positive value of θ.

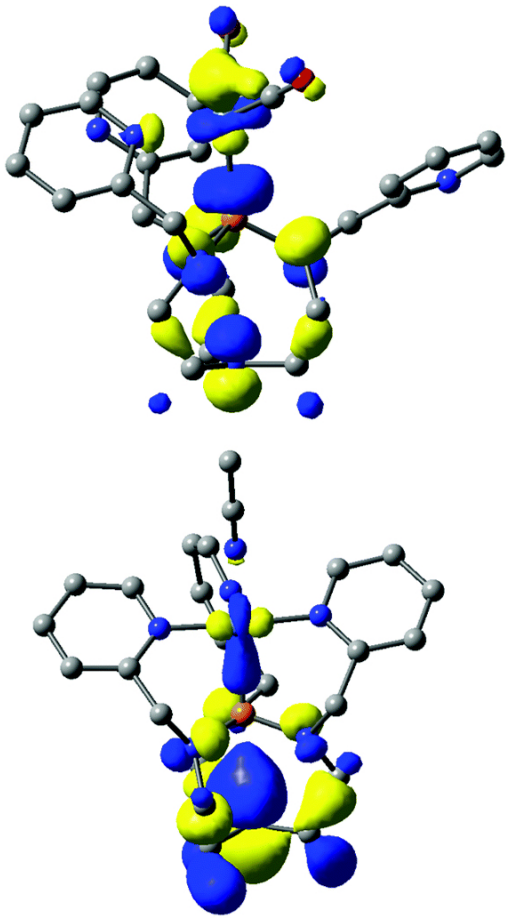

Figure B.3. HOMOs of Ni(0) (top) and Ni(II) (bottom). All surfaces are at an isovalue of 0.035.

Conclusions

The use of flexible ligands with adjustable coordinative inter- actions has shown great utility in accessing reactive metal sites. The experimental and computational results demonstrate that an azaphosphatrane incorporated into a chelating ligand provides a new type of variable ligand interaction. The metal–ligand distance remains constant while the non-coordinating nitrogen in the azapho- sphatrane can donate additional electron density into the phosphorus ligand. A prior study previously measured the Tolman parameter of azaphosphtranes and found that even in the absence of a transannular interaction, they are among the most strongly donating phosphine

ligands. Thus, the TPAP ligand represents an inherently strong ligand that can increase its donor strength in contrast to prior systems that utilize weaker interactions. The higher donor strength available with TPAP may also be valuable for stabilizing more electron deficient metal ions.

Experimental

DFT calculations were performed using the Gaussian09 program suite with the incorporated NBO 3.1 package at the M06 level of theory with 6–311G++(3df,3pd) basis set for 3rd row main groups, 6-311G**++ basis set for 2nd row main groups, and LANL2DZ basis set for all metals. Geometry optimizations of the complexes from the X-ray coordinates, followed by harmonic frequency calculations indicated that all of the calculated compounds are minima on the potential energy surface.

Optimized Coordinates for 1:

Co	4.371075687008	11.960855530715	3.048982070568
Cl	4.634713442546	9.695386084716	3.587945203238
P	3.738984775026	14.022572200466	3.177398006133
N	6.273616426953	12.361825325558	3.495916561202
N	4.952065534771	15.095450696038	3.723405033398
N	3.290682630871	14.592556736451	1.603298717068
N	3.003339093560	17.174173732985	3.062922060984
N	2.437895432826	14.422833797314	4.232200144291
C	1.486728536005	13.034470522625	8.364083788467
H	0.955263198367	13.551050552162	9.162566464228
N	2.800274799624	11.570224399275	1.873753200258
C	6.801790419335	13.463652844559	4.092847751244
C	5.843265644102	14.468171889881	4.699351441080
H	5.234715324823	13.966337309665	5.464159130147
H	6.411449474160	15.250799387243	5.213352249917
C	2.149834874698	15.493617109708	1.400955032421
H	1.284887452616	15.183863901210	2.004815578377
H	1.843242424522	15.432874559297	0.349425202851
C	2.497078236601	16.956247500414	1.727259332162
H	3.254160130979	17.308590926891	1.016782381624
H	1.588843279163	17.561211633978	1.554153699903
C	2.131870960059	16.936649802999	4.195644039218
H	1.103123328453	16.893653403632	3.817515135583
H	2.173634354997	17.791590840110	4.893515840063

C	2.423025481301	15.666445870365	5.016811421084
H	3.377016840274	15.799187493067	5.542640473493
H	1.653991506101	15.560042429694	5.788748622340
C	1.533052715584	13.358168029460	4.705984343495
H	1.573952837974	12.535555234651	3.990171483705
H	0.507318499323	13.746111339029	4.717269719694
C	1.850613698756	12.837964955671	6.100995022459
C	2.764754596444	11.793199862328	6.298633161718
H	3.255326733253	11.318719225908	5.451147405105
C	3.029554630684	11.371641370684	7.600797590524
H	3.727276858030	10.557302442681	7.777319482489
C	2.380020175406	12.005136732564	8.661018116039
H	2.553134558732	11.708152616618	9.691446726738
N	1.216647763369	13.447418214625	7.119087710089
C	4.402076947816	17.476793200098	3.270439668702
H	4.519042889421	17.805876093755	4.310466754472
H	4.711828821696	18.322631423499	2.632163872152
C	5.363660623560	16.295223773277	3.005821531419
H	5.409216578672	16.102345927616	1.926111004805
H	6.377950927859	16.568154541549	3.324432375759
C	3.477271698282	13.545425161549	0.580618093821
H	4.521088315234	13.215424510258	0.604998511665
H	3.291926678090	13.989517979107	-0.403315530927
C	2.583031424049	12.332810950276	0.768220129943
C	1.993750185417	10.505206608229	2.077769523040
H	2.229877286551	9.911161925270	2.951625135808
C	0.961571659498	10.157474208989	1.210987648680
H	0.349675129463	9.289469014964	1.434372165995
C	0.745565041635	10.928445896135	0.072069776587
H	-0.045533668704	10.682373902507	-0.630661162498
C	1.573919185569	12.028978435577	-0.144859193610
H	1.445957632252	12.658028326720	-1.020808997719
C	8.177499453162	13.695335059296	4.134934388166
H	8.545718841048	14.587729854096	4.632892110005
C	9.060169660021	12.790735512434	3.549631175000
H	10.132715899438	12.961328673895	3.576068818384
C	8.522009564285	11.661984637730	2.937110946612
H	9.152146555760	10.913028961072	2.468224369897
C	7.143073832921	11.482540241864	2.939135013291
H	6.691796479408	10.598568674903	2.508942527354

Optimized Coordinates for 2:

Co	7.188603486027	6.552243987197	10.731733250787
P	7.131874270102	8.072006821056	12.407513779643
N	7.167607304849	9.969609977505	14.457987791084
N	8.652670931652	7.996116901656	13.171923804625
N	8.097988922452	5.237507276670	12.033056914030
N	6.863755534259	9.598840576035	11.755314057291
N	7.336060810928	8.047962685134	9.249766716643
N	5.849981286239	7.700613914186	13.455167841377
N	5.031041776946	6.212754268297	10.945346682264
N	7.295061915420	5.092319837347	9.308079573808
C	7.106065869020	11.166165254834	13.632992591230
H	7.721636348697	11.982890871593	14.036354567093
H	6.071513260794	11.523340323033	13.608060530078
C	7.560304124288	10.812786995971	12.205544409076
H	7.337828533743	11.623015549087	11.504770855600
H	8.644640034089	10.654490033788	12.183776832051
C	6.007516380443	9.632350352832	10.566725355300
H	5.577207444283	10.632556087095	10.470636285354
H	5.167957852170	8.939276166014	10.696906972606
C	6.772962814937	9.278780860342	9.307651966047
C	6.935083980843	10.210073723761	8.281967739859
H	6.450168894150	11.178010588255	8.359674316559
C	7.724270466053	9.897313976994	7.176455018642
H	7.863124499469	10.615098876054	6.373831855945
C	8.341178975880	8.648960919078	7.137182768404
H	8.984655252855	8.358146149582	6.313811129147
C	8.115845082846	7.761526963200	8.183334773845
H	8.572041298011	6.780083419442	8.172711026929
C	8.448114089342	9.598882841099	15.038167343516
H	8.455142574052	9.689900145401	16.134357074646
H	9.215596959476	10.276064187203	14.651193651550
C	8.798226306737	8.161624506335	14.634935599449
H	9.836646535017	7.939337277056	14.899507974021
H	8.163096616438	7.448405703232	15.177428671118
C	9.614463727916	7.092029998796	12.516318673844
H	10.602909608420	7.266629474605	12.948655461484
H	9.692248694809	7.361632638348	11.454946698951
C	9.242011081053	5.623425869326	12.646208847905
C	10.007074000510	4.722359191039	13.386464010194
H	10.925146248054	5.058398181398	13.857805925393
C	9.582739942390	3.399623269124	13.514051506305
H	10.165794226324	2.687125757948	14.089521432616
C	8.393861506158	3.013081341235	12.894633212914
H	8.017751529012	1.998692457761	12.973591187552
C	7.686969173628	3.959430046164	12.161166181659

H	6.761714134578	3.703891633088	11.655861165745
C	5.950857014670	9.527711574116	15.120331762342
H	5.382675685480	10.364599152337	15.553087553843
H	6.222335342084	8.860019071939	15.943993088478
C	5.069611142837	8.764250480258	14.121194774677
H	4.226152101255	8.296449030451	14.637133470897
H	4.649324186956	9.459769073259	13.383768774004
C	5.251308199915	6.358407682072	13.379290477203
H	4.642021405439	6.208337335300	14.273893749233
H	6.044284121014	5.608096556974	13.416991075664
C	4.401221142910	6.135442370900	12.140410573989
C	3.032213708559	5.878430910430	12.230910928852
H	2.560103963156	5.813304495009	13.206273820150
C	2.283193926921	5.709701882677	11.066231130831
H	1.217064696925	5.511209107370	11.119710084931
C	2.930450195558	5.809854797764	9.835595542542
H	2.391579120222	5.697709140788	8.900743177721
C	4.299544109767	6.060026495110	9.824615506834
H	4.841180917187	6.143283232290	8.888084704234
C	7.361222745830	4.213593254398	8.555507202851
C	7.446115596997	3.110513297339	7.605397510488
H	6.656064477041	2.380026268114	7.807977029260
H	8.419262073778	2.616322812076	7.692763309295
H	7.328099820143	3.486024103832	6.583710727502

Optimized Coordinates for 3b

Ni	3.092092727440	8.976607300487	1.823344947458
P	2.773411852696	10.896272011393	0.554976223733
O	2.934407829855	9.391796238451	4.725641108455
N	2.739165341336	13.677703711092	-1.231178480607
C	2.340267053286	12.900372100782	-2.370073379133
H	3.226758247895	12.732001598835	-2.997417123283
H	1.620984761522	13.459729637931	-2.995610702955
O	1.615321904791	6.535960684506	1.120535984834
N	1.532953872957	12.052767560957	0.940123374738
C	1.717090138635	11.558245082109	-2.000922078467
H	0.766503835853	11.744390692123	-1.481314613428
H	1.458694649723	11.006885044473	-2.916187227633
N	2.565210457143	10.715348892731	-1.184800443904
C	1.748033272697	14.188687668603	-0.323226621358
H	0.763917373876	14.085483534235	-0.799760915199
H	1.895422479606	15.270244535225	-0.149234397727
N	4.263058001145	11.885908673561	0.697375773062
C	1.740140422965	13.482493695685	1.028604441889
H	2.692349659476	13.678869038929	1.540580943330
H	0.951172391793	13.904546876758	1.666477717133
N	-1.512554274930	11.441523459181	2.880272929338
C	4.130505354226	13.804128950551	-0.906530045891
H	4.224400284071	14.537670125641	-0.095350298259
H	4.692412891471	14.216501429202	-1.765004110068
N	3.333851995881	7.308672418325	-2.337863110128
C	4.833354680451	12.517956083374	-0.488071712779
H	4.872812638300	11.829437289085	-1.348691036958
H	5.876784896232	12.772449436016	-0.257058105679
N	5.103053994040	8.903419035708	1.097351642186
C	0.218672019317	11.532385902526	1.220254593301
H	0.176408362243	10.476905329065	0.907687707425
H	-0.553623940097	12.044200768430	0.623430231071
C	-0.204649215734	11.588899189525	2.667973172438
C	0.715613881562	11.737343652210	3.698365746468
H	1.769874867320	11.854591487579	3.463530389263
C	0.258266056943	11.710267526713	5.005169897346
H	0.955751510509	11.803980952268	5.832010720495
C	-1.098514925887	11.549056157521	5.236268909094
H	-1.501823469031	11.520568682314	6.242886147347
C	-1.937871249732	11.422146443697	4.138632290853
H	-3.010793608176	11.298060592768	4.281990363261
C	3.298726650645	9.650228700086	-1.821142260874
H	4.217905509535	9.423243637348	-1.263739763323
H	3.651565240874	9.983431265432	-2.811441617560
C	2.561656160905	8.344409702929	-2.002304135416

C	1.184927720291	8.234931557693	-1.843878053741
H	0.603862176433	9.101224541807	-1.543964730412
C	0.588112518789	7.001968473450	-2.046746401081
H	-0.483761050682	6.883087746091	-1.921062339626
C	1.381914288332	5.921453049799	-2.393638716227
H	0.959465084590	4.935038891708	-2.550831713480
C	2.747110639817	6.130553711319	-2.521577650763
H	3.403695691583	5.301871151562	-2.785445101198
C	5.254619605183	11.275878968045	1.584209579189
H	4.774274527667	11.043709733674	2.541259666071
H	6.039887578506	12.015853869761	1.780053822268
C	5.864392209980	10.009842541012	1.039106705315
C	7.119035080906	9.999757648659	0.443186242974
H	7.707132418381	10.912694071313	0.420493136504
C	7.599040900196	8.827131735407	-0.117075276191
H	8.573048581791	8.802361945308	-0.595634746548
C	6.811845844835	7.689412323974	-0.054902883945
H	7.138227879458	6.748912074256	-0.483437023234
C	5.577206135029	7.774127771471	0.564593634200
H	4.926520298037	6.906870650178	0.632043361471
C	3.023314946651	9.275837216355	3.589396131157
C	2.202434338598	7.500287530795	1.307549283405

Optimized Coordinates for 4

Ni	3.125730684072	2.083130086723	2.981539824812
P	1.841404721093	3.078432592631	1.419727162616
N	0.176766262113	4.293538894561	-0.325453038752
N	2.617779474989	2.913867045240	-0.136814498496
N	1.748417572387	4.758839574322	1.839609365719
N	0.368357379571	2.213703124330	1.458417688801
N	3.606900933220	0.752830486431	1.657112178955
N	2.574327922453	3.361174521022	4.348481731340
N	0.985151960079	0.472596385156	3.888743999588
N	4.492985253087	1.354604180472	4.209765188062
C	1.006895590067	4.162008331871	-1.504988278082
H	0.892793573625	5.013390080072	-2.191695660130
H	0.700144353743	3.265371462907	-2.053772214675
C	2.458213353443	4.018182583185	-1.097584106031
H	3.063255947582	3.773401659827	-1.976151625472
H	2.847786048447	4.963066044332	-0.684979212566
C	0.088103561686	5.603435705079	0.285075056932
H	-0.916747176345	6.038619043695	0.191665358475
H	0.781137840335	6.278032734745	-0.228786087994
C	0.495169627054	5.503591737992	1.749011373983
H	0.658498118025	6.500685736990	2.172869982618
H	-0.306022351168	5.039044905358	2.345476845345
C	-0.961321125851	3.406230377341	-0.213990979195
H	-1.515788741863	3.307798530248	-1.158601655277
H	-1.659348849327	3.818643778926	0.524594500286
C	-0.446622651394	2.053366731314	0.261180697776
H	-1.257973310684	1.356291629218	0.495734355881
H	0.158518773254	1.579367345004	-0.519263203433
C	4.011137786514	2.459459389560	-0.015384388206
H	4.609315443413	3.086599625918	0.667036827219
H	4.471480329442	2.541404919235	-1.002648054869
C	4.039678271610	1.030846351214	0.415113108330
C	4.432100179190	0.024689565229	-0.452789809643
H	4.779627890776	0.287387595281	-1.445839129467
C	4.366048291733	-1.296889442038	-0.047496532279
H	4.669988306395	-2.094594523616	-0.716747004220
C	3.895569939143	-1.578522269319	1.225291990637
H	3.813881209557	-2.596097608768	1.587965533608
C	3.530051409113	-0.530664274840	2.043943636355
H	3.164361454118	-0.707149430754	3.047424881363
C	2.766898381403	5.196212035219	2.779436031529
H	3.751573170898	4.843254648207	2.446458092089
H	2.810014364524	6.289230913839	2.772091596881
C	2.490471938214	4.690035164009	4.165338358138
C	2.085811899324	5.536185777734	5.184288251016

H	2.035742634687	6.604273586627	4.998725135725
C	1.752984572733	5.007440478404	6.420865945854
H	1.432207537547	5.655130757262	7.229760465742
C	1.835747098175	3.635982007958	6.602430899601
H	1.581163689218	3.173416899805	7.548514907290
C	2.251926399591	2.848784502290	5.547775108248
H	2.316520687752	1.771115543088	5.641722238151
C	-0.316433577873	2.160676604448	2.751749093427
H	-1.369085241301	2.434992755357	2.606626138841
H	0.099996413212	2.913640872234	3.434159804675
C	-0.219122729400	0.814750553205	3.416171053590
C	-1.334240684675	0.000167403292	3.554501378546
H	-2.294151995103	0.317987355713	3.158442948928
C	-1.206709330774	-1.212182387566	4.216329843713
H	-2.063265165499	-1.866545613607	4.339026704261
C	0.031300267157	-1.562839017300	4.728116264141
H	0.177115934342	-2.490533652189	5.269397391558
C	1.088493887078	-0.687469844124	4.535529579365
H	2.074278165444	-0.928629990257	4.938979216872
C	5.389449422597	1.026161626852	4.849271062889
C	6.516254994649	0.619996486085	5.648555603380
H	7.367603367881	1.275445732760	5.448233994819
H	6.798554336364	-0.407729317933	5.408105334456
H	6.267184307140	0.680842912491	6.710651746362

Optimized Coordinates For 5

Pd	15.306692659287	10.600074854391	9.569444379304
P	13.793220133832	9.061853287116	8.620605271103
N	12.038983959002	7.303046465038	7.709805192916
N	14.342135687983	7.500152956934	9.122703129194
N	13.852694412908	9.242438439405	6.888243118087
N	12.280283460978	9.564791005500	9.228867435190
N	15.715226449677	9.265993235293	11.154892713548
N	14.775881208167	11.921196188966	8.023819984532
N	13.230697508324	11.760078896131	11.253864299040
N	16.822157227076	11.995579367985	10.317961934223
C	12.538614865647	6.091033115646	8.329061485722
C	12.281066952905	7.470775248921	6.289197791771
C	13.390041448626	6.470284530086	9.531202253531
C	10.818617044759	7.876389524596	8.241516841640
C	13.675227632478	8.022433424954	6.083003364832
C	15.717691887244	7.414515247803	9.588897774190
C	16.128911695005	7.112838021674	12.065615268984
C	11.065836563331	9.365681260887	8.449165868645
C	15.881121349937	7.945317575008	10.986858032763
C	16.197957805744	7.650895603723	13.341641524150
C	14.933496851672	10.118450119565	6.404458790822
C	12.143474479539	9.678988550937	10.685462815195
C	16.007621753657	9.013928588320	13.504594933030
C	14.662810570609	11.551088311656	6.737671755039
C	15.767008983927	9.790158820115	12.387163289214
C	12.068099457813	11.106613967404	11.157112322899
C	14.283240506725	12.463295074786	5.765738772062
C	10.853718887523	11.693327305413	11.486266811702
C	14.010544128283	13.773361550925	6.123376511148
C	14.500504399603	13.184742065151	8.375774812456
C	10.839802227850	13.008255473428	11.928138482237
C	13.205026305995	13.017128518785	11.690322049013
C	14.118104355381	14.139422918130	7.455300662378
C	17.734426334845	12.640440941396	10.588400152978
C	12.041916058706	13.687708664206	12.037349001391
C	18.881158335382	13.445064013251	10.925569760398
H	11.727506816829	5.410677877295	8.623220183667
H	13.163812041215	5.557112843316	7.606006867230
H	12.153848127591	6.532195451366	5.731403653522
H	13.956688381377	5.606284876718	9.893958927936
H	14.439860303661	7.267309122730	6.323296375753
H	9.952868608888	7.704910137783	7.586203445175
H	10.595067731834	7.398374404407	9.202968053038

H	11.553778323283	8.185632543476	5.890688394847
H	16.036231063469	6.368726006343	9.540966897208
H	12.757574938363	6.802477664030	10.369102205522
H	13.811854267250	8.298326687698	5.033478299506
H	16.268699777915	6.049627869420	11.897660420002
H	16.371382163817	7.975007127210	8.908524083945
H	11.170165320989	9.874188054670	7.484491688561
H	16.392281890059	7.013693421082	14.197811102876
H	10.240469792825	9.856684019321	8.974100229088
H	14.965971816461	10.014067593436	5.317563551713
H	11.247288895769	9.126592990308	10.996770529456
H	15.923972790556	9.821319925560	6.786278801909
H	12.992691375818	9.194698562269	11.182629215436
H	14.203865390948	12.138946850062	4.733867241628
H	16.041699708170	9.477495369196	14.483266147031
H	9.931984191524	11.123475316702	11.412075021433
H	15.596675797420	10.859080050299	12.462206897307
H	13.716259183275	14.498036145092	5.371849007036
H	14.597647225311	13.422713473961	9.429013017597
H	9.905239488882	13.490162339526	12.195484093572
H	14.173206107077	13.512938711070	11.781069123297
H	13.911660528181	15.151073098656	7.783580308269
H	19.683786453128	13.267450721816	10.205654470646
H	19.240533274170	13.187713225797	11.924681796743
H	12.081184488519	14.710247856943	12.395150565958
H	18.618030145007	14.505216528920	10.906310797768

Optimized Coordinates For 6

Pt	9.133310647764	10.003969537026	13.130973184868
Cl	11.447258675812	9.380148362969	12.706918712896
P	6.890398381546	10.591526690249	13.538034189185
N	4.183609347932	11.312274020319	13.820176070621
N	6.247617446589	9.634150426210	14.865005608878
N	6.020998677703	10.228980310792	12.069630149212
N	6.783850535656	12.238035584700	13.975545012614
N	9.383370125499	9.618693843756	15.156430696500
N	8.931939163303	10.516380904373	11.121057769728
N	10.028918009502	13.465513914241	12.970195595011
C	3.872485953722	10.298595301981	14.798314132842
H	2.851271465905	9.903703818698	14.676627528118
H	3.921076256457	10.750956060933	15.795387014948
C	4.864452418900	9.153376151321	14.732429538976
H	4.675537342902	8.466409516306	15.564114325332
H	4.733133149271	8.579140707188	13.800195551326
C	3.782299964565	11.102760006975	12.450693453432
H	3.039342138862	11.843766030190	12.117630129743
H	3.312831107401	10.115577489393	12.369163828531
C	5.006226310501	11.138425711324	11.549345529826
H	4.744990104013	10.811271019168	10.536533523085
H	5.384739799947	12.169631775143	11.455809296737
C	4.391589888435	12.663326351564	14.281080926906
H	3.624551489184	12.987470218857	15.002440080330
H	4.331766645948	13.341209348913	13.420575947130
C	5.781030366929	12.752148655608	14.893386799125
H	6.047636740301	13.784639162695	15.143150846428
H	5.814720316335	12.179118440045	15.829887922891
C	7.174578411605	8.554539206155	15.245161740669
H	7.449884595632	7.913212649280	14.391135838169
H	6.644982260569	7.921454280209	15.961831809737
C	8.418694545515	9.056762844457	15.913466289406
C	8.581978610916	8.926771540606	17.281993662254
H	7.790273838944	8.470382011921	17.865847621975
C	9.748663913451	9.366458790746	17.885909319732
H	9.886440374894	9.261857049480	18.956788628296
C	10.735138125819	9.926994097190	17.095610633837
H	11.673087837718	10.272930517882	17.513661575692
C	10.519361653284	10.040596375760	15.736445139513
H	11.266802817955	10.457116269058	15.070627666546
C	6.756135945492	9.417262654441	11.106035635200
H	6.042762277457	9.025543014958	10.374004172711
H	7.193892948360	8.550094770971	11.614567619480

C	7.842770877249	10.179189081753	10.400418571274
C	7.718308138907	10.567360505997	9.079342244932
H	6.835344311590	10.270284859477	8.522450237916
C	8.721349914279	11.318301981975	8.484558340758
H	8.636052567159	11.627055872145	7.448072579337
C	9.829089092012	11.663519915372	9.235658977806
H	10.639056010800	12.249583303286	8.819393163829
C	9.905162071236	11.244585844469	10.550502940463
H	10.756183709242	11.483115340098	11.175574636014
C	7.657628029013	13.147937739660	13.249133188367
H	7.164176662348	14.129185500717	13.211605803291
H	7.774993962550	12.843623505343	12.200115045673
C	9.038580380346	13.290253377262	13.843957204415
C	9.241877240764	13.264076085774	15.219876864764
H	8.408286746141	13.101117843084	15.897588440483
C	10.527199569725	13.446981867540	15.702542964494
H	10.718367513120	13.448909487206	16.771806942391
C	11.564763915466	13.626607874033	14.800182397218
H	12.587104663206	13.767948379998	15.132580953459
C	11.261867176166	13.622204859604	13.446725700255
H	12.052246819990	13.749191341252	12.708902084524

Representative Calculation Input for Geometry Optimization and Vibrational Frequency Analyses

```
%mem=50GB
%nproc=12
%Chk=pt2tpap_m06.chk
# M06/GenECP Opt Freq

pt2tpap/m06/opt and freq

1 1
Pt      9.0901005673    9.9232684074    13.2120358793
Cl      11.1864682092   8.9660080671    12.7817823928
P       6.9075304391    10.4626836050   13.5059769692
N       4.1769351761    11.3062161791   13.8794455613
N       6.2096242266    9.4229826191    14.7085820071
N       5.9240368543    10.3526394893   12.0886117499
N       6.9619925669    12.1017586994   14.0896875417
N       9.3054973047    9.5634060628    15.1342491953
N       8.9538821289    10.3445607035   11.2040724837
N       9.9014253526    13.6702235122   12.8855776391
C       3.8727947899    10.1870594364   14.7455465338
H       2.8434250131    9.8640511238    14.5518826557
H       3.9278766605    10.5029489649   15.7965615825
C       4.8298384694    9.0356367706    14.4986249776
H       4.5688760258    8.2537701518    15.2161837558
H       4.6983838539    8.6395809085    13.4931704776
C       3.8188473369    11.2560092542   12.4760418117
H       3.1068338790    12.0441797286   12.2463623479
H       3.3508809522    10.2850361256   12.2492547467
C       5.0597157973    11.4130515581   11.6536294987
H       4.8186348715    11.2705294237   10.5902435744
H       5.4974117778    12.4100251959   11.7587360776
C       4.5214525147    12.5773162162   14.4674860461
H       3.7677655683    12.8110730635   15.2368196868
H       4.4721994042    13.3657673511   13.7109392480
C       5.9206631242    12.5171110539   15.0577524505
H       6.1639943075    13.5071481140   15.4644656518
H       5.9085863381    11.8362442725   15.9297822925
C       7.0942597925    8.4428560026    15.2644566860
H       7.4269129476    7.7633437185    14.4781043812
H       6.5426483152    7.8762411909    16.0152186644
C       8.2668128616    9.0560745197    15.9310194465
C       8.4322890055    8.9765361971    17.2551539559
H       7.7132588108    8.5497209957    17.9122672312
C       9.6621738501    9.4670679345    17.8798826973
```

H	9.8308259842	9.4159339060	18.9506384903
C	10.6726153974	10.0345023643	16.9953020775
H	11.5450548897	10.4430889778	17.4363153383
C	10.4870039237	10.0471808557	15.6923701635
H	11.1799009590	10.5297830179	15.0525317297
C	6.5975459975	9.5173524334	11.0715194320
H	5.8686736221	9.2520024043	10.3114552420
H	6.9495376892	8.5771297042	11.5284645064
C	7.7819497192	10.1342652105	10.4312862820
C	7.7594249548	10.4797565189	9.1251312143
H	6.9193478447	10.3227876328	8.4837976515
C	8.9059176012	11.1521808162	8.5055071509
H	8.9041072770	11.5015559364	7.4728513253
C	10.0508711760	11.4063642325	9.3679738198
H	10.8846260810	11.9159127625	8.9476254853
C	10.0506591388	11.0092269667	10.6307680636
H	10.8848335248	11.2023938818	11.2416457731
C	7.6199380666	13.0744363312	13.3005961014
H	7.0417354316	13.9944116651	13.3029899277
H	7.6935920784	12.7085679728	12.2779504587
C	8.9743183608	13.3380886587	13.8017127976
C	9.3147098824	13.3176123373	15.1637085636
H	8.6097043106	13.0528228944	15.9191732618
C	10.6024060402	13.6540145499	15.5433948087
H	10.8899344116	13.6551296470	16.5779730282
C	11.5256056699	13.9941584406	14.5782994960
H	12.5226240776	14.2581000463	14.8529615092
C	11.1564587914	13.9873004815	13.2473801893
H	11.8660880051	14.2360227362	12.5038782148

C H N 0
6-311G**++
****

P Cl 0
6-311G++(3df,3pd)
****

Pt 0
LANL2DZ
****

Representative Gaussian input for NBO Analyses

```
%mem=50GB
%nproc=12
%Chk=pt2tpap_m06.chk
# M06/GenECP Geom=Checkpoint Guess=Read Pop=(nbo,savenbo,regular)

pt2tpap/m06/NBO and pop

1 1

C H N 0
6-311G**++
****
P Cl 0
6-311G++(3df,3pd)
****
Pt 0
LANL2DZ
****
```

Influence of Complex Charges on Calculated Distances. Compounds $[Ni(TPAP)(CH_3CN)]^{2+}$ (**4**) and $[Pd(TPAP)(CH_3CN)]^{2+}$ (**5**) were isolated with axial CH_3CN ligands, while $[Pt(TPAP)Cl]^{+}$ (**6**) was isolated with an anionic chloride ligand in the axial position. As a result, **6** is mono-cationic while **4** and **5** are di-cationic. To probe whether the overall complex charge significantly impacts the M–P and P---N_{ax} distances, the compounds $[Pd(TPAP)Cl]^{+}$ and $[Pt(TPAP)(CH_3CN)]^{2+}$ were investigated computationally and compared to their di-cationic and mono-cationic analogues, respectively.

Table B.3. shows that the M–P distances are not particularly sensitive to changes in the overall complex charges, as increasing the charge changes the M–P distances at most by ca. 0.01 Å. For both Pt and Pd compounds, the angles θ and P---Nax distances increase by 5.1 Å and 0.15 Å, respectively, when going from mono-cationic to di-cationic. Because the differences in changes of θ and P---N_{ax} are identical for each compound, the complex charge does not account for any non-monotonic trends observed.

Table B.3. DFT-Calculated Geometrical Parameters for Selected Mono-Cationic and Di-Cationic Complexes

Parameter	$[Pt(TPAP)(CH_3CN)]^{2+}$	$[Pt(TPAP)Cl]^{+}$	$[Pd(TPAP)(CH_3CN)]^{2+}$	$[Pd(TPAP)Cl]^{+}$
M–P (Å)	2.35025	2.35406	2.35733	2.37091
P---N_{ax} (Å)	2.65028	2.81528	2.64581	2.81892
θ (º)	18.8896	13.78628	18.61757	13.4973

References

1. Anderson, J. S.; Rittle, J.; Peters, J. C. *Nature* **2013**, *501*, 84.

2. Rittle, J.; Peters, J. C. *Proc. Natl. Acad. Sci.* **2013**, *110*, 15898-15903.

3. Creutz, S. E.; Peters, J. C. *J. Am. Chem. Soc.* **2014**, *136*, 1105-1115.

4. Anderson, J. S.; Moret, M.-E.; Peters, J. C. *J. Am. Chem. Soc.* **2013**, *135*, 534-537.

5. Moret, M.-E.; Zhang, L.; Peters, J. C. *J. Am. Chem. Soc.* **2013**, *135*, 3792-3795.

6. Moret, M.-E.; Peters, J. C. *J. Am. Chem. Soc.* **2011**, *133*, 18118-18121.

7. Del Castillo, T. J.; Thompson, N. B.; Suess, D. L. M.; Ung, G.; Peters, J. C. *Inorg. Chem.* **2015**, *54*, 9256-9262.

8. Rauch, M.; Parkin, G. *J. Am. Chem. Soc.* **2017**, *139*, 18162-18165.

9. Rauch, M.; Ruccolo, S.; Parkin, G. *J. Am. Chem. Soc.* **2017**, *139*, 13264-13267.

10. Rudd, P. A.; Planas, N.; Bill, E.; Gagliardi, L.; Lu, C. C. *Eur. J. Inorg. Chem.* **2013**, *2013*, 3898-3906.

11. Vollmer, M. V.; Xie, J.; Lu, C. C. *J. Am. Chem. Soc.* **2017**, *139*, 6570-6573.

12. Cammarota, R. C.; Lu, C. C. *J. Am. Chem. Soc.* **2015**, *137*, 12486-12489.

13. Cammarota, R. C.; Vollmer, M. V.; Xie, J.; Ye, J.; Linehan, J. C.; Burgess, S. A.; Appel, A. M.; Gagliardi, L.; Lu, C. C. *J. Am. Chem. Soc.* **2017**, *139*, 14244-14250.

14. Buss, J. A.; Agapie, T. *Nature* **2015**, *529*, 72.

15. Buss, J. A.; Agapie, T. *J. Am. Chem. Soc.* **2016**, *138*, 16466-16477.

16. Horak, K. T.; VanderVelde, D. G.; Agapie, T. *Organometallics* **2015**, *34*, 4753-4765.

17. Horak, K. T.; Lin, S.; Rittle, J.; Agapie, T. *Organometallics* **2015**, *34*, 4429-4432.

18. Edouard, G. A.; Kelley, P.; Herbert, D. E.; Agapie, T. *Organometallics* **2015**, *34*, 5254-5277.

19. Horak, K. T.; Agapie, T. *J. Am. Chem. Soc.* **2016**, *138*, 3443-3452.

20. Buss, J. A.; Edouard, G. A.; Cheng, C.; Shi, J.; Agapie, T. *J. Am. Chem. Soc.* **2014**, *136*, 11272-11275.

21. Henthorn, J. T.; Agapie, T. *Inorg. Chem.* **2016**, *55*, 5337-5342.

22. Henthorn, J. T.; Lin, S.; Agapie, T. *J. Am. Chem. Soc.* **2015**, *137*, 1458-1464.

23. Tsui, E. Y.; Agapie, T. *Polyhedron* **2014**, *84*, 103-110.

24. Lin, S.; Herbert, D. E.; Velian, A.; Day, M. W.; Agapie, T. *J. Am. Chem. Soc.* **2013**, *135*, 15830-15840.

25. Suseno, S.; Horak, K. T.; Day, M. W.; Agapie, T. *Organometallics* **2013**, *32*, 6883-6886.

26. Horak, K. T.; Velian, A.; Day, M. W.; Agapie, T. *Chem. Commun.* **2014**, *50*, 4427-4429.

27. Lin, S.; Day, M. W.; Agapie, T. *J. Am. Chem. Soc.* **2011**, *133*, 3828-3831.

28. Chao, S. T.; Lara, N. C.; Lin, S.; Day, M. W.; Agapie, T. *Angew. Chem. Int. Ed.* **2011**, *50*, 7529-7532.

29. Halter, D. P.; Heinemann, F. W.; Bachmann, J.; Meyer, K. *Nature* **2016**, *530*, 317.

30. Bart, S. C.; Heinemann, F. W.; Anthon, C.; Hauser, C.; Meyer, K. *Inorg. Chem.* **2009**, *48*, 9419-9426.

31. Fieser, M. E.; Palumbo, C. T.; La Pierre, H. S.; Halter, D. P.; Voora, V. K.; Ziller, J. W.; Furche, F.; Meyer, K.; Evans, W. J. *Chem. Sci.* **2017**, *8*, 7424-7433.

32. Kisanga, P. B.; Verkade, J. G.; Schwesinger, R. *J. Org. Chem.* **2000**, *65*, 5431-5432.

33. Nyulászi, L.; Veszprémi, T.; D'S, B. A.; Verkade, J. *Inorg. Chem.* **1996**, *35*, 6102-6107.

34. Aneetha, H.; Wu, W.; Verkade, J. G. *Organometallics* **2005**, *24*, 2590-2596.

35. Liu, X.-D.; Verkade, J. G. *Inorg. Chem.* **1998**, *37*, 5189-5197.

36. Lensink, C.; Xi, S. K.; Daniels, L. M.; Verkade, J. G. *J. Am. Chem. Soc.* **1989**, *111*, 3478-3479.

37. Thammavongsy, Z.; Kha, I. M.; Ziller, J. W.; Yang, J. Y. *Dalton Trans.* **2016**, *45*, 9853-9859.